

**SYNTHESIS OF NANOSTRUCTURED WO₃ PARTICLES VIA AEROSOL
PROCESS AND THEIR PHOTOCATALYTIC APPLICATION**

(エアロゾルプロセスによるナノ構造化酸化タンゲステン微粒子の合成
と光触媒への応用)

By
OSI ARUTANTI

HIROSHIMA UNIVERSITY
SEPTEMBER 2015

**SYNTHESIS OF NANOSTRUCTURED WO₃ PARTICLES VIA AEROSOL
PROCESS AND THEIR PHOTOCATALYTIC APPLICATION**

(エアロゾルプロセスによるナノ構造化酸化タンゲステン微粒子の合成
と光触媒への応用)

A Thesis submitted to
The Department of Chemical Engineering
Graduate School of Engineering
Hiroshima University

By
OSI ARUTANTI

In Partial Fulfillment of the Requirements
For the Degree of
Doctor of Engineering

Hiroshima University
September 2015

Approved by

Professor Kikuo Okuyama
Advisor

Abstract

Photocatalytic method is one of the advanced oxidation process to eliminate harmful organic compounds in polluted water which cannot be effectively removed by conventional treatment process. Since the performance of photocatalytic activity is mainly influenced by material properties, tungsten trioxide (WO_3) which has a narrow band gap, harmless, good thermal stability, and good photostability is a prospective material for solar-related material application. Therefore, deep understanding regarding the influence of WO_3 properties on photocatalytic performance is desired.

In this dissertation, synthesis of nanostructured WO_3 particles via aerosol process for photocatalytic application is systematically investigated. Aerosol process was used in this study because it can produce particles in the nano- to submicron-sized ranges with a high production rate, continuous operation, and low cost process. The effect of several process parameters on the particles formation and morphology was studied. The prepared particles were used to decompose rhodamine B (RhB) and amaranth as the model of organic waste under visible light. The major contents of this dissertation are listed as follow.

Chapter 1 provides the background and motivation of current research. Basic theoretical explanation and review of previous researches on photocatalyst materials, especially WO_3 particles were also provided.

Chapter 2 describes the synthesis of WO_3 particles with controllable crystallite and particle sizes using spray-pyrolysis method. To prepare fine particles, ammonium tungstate pentahydrate (ATP) was used as a starting precursor. The crystallite and particle sizes were controlled by changing the synthesis temperatures from 120 to 1300°C and precursor concentrations from 2.5 to 15 mmol/L. Submicron particles were obtained when the synthesis temperature of below 900°C. Increases in temperature process above 900°C lead the production of nanoparticles (NPs) due to the evaporation and condensation of WO_3 material during the high synthesis temperature process. It was found that the synthesis temperature has a more significant effect on the change of particles morphology than precursor concentration. Photocatalytic analysis

showed that the ability of WO_3 catalyst to decompose RhB was influenced by crystallinity and particle size. The optimum condition to produce WO_3 particles with the highest photocatalytic performance was the synthesis temperature of 1200°C and the precursor concentration of 10 mmol/L . This condition resulted in the production of WO_3 particles with diameter of 105 nm and crystal size of 25 nm .

In **Chapter 3**, the direct synthesis of composite WO_3/TiO_2 NPs using flame-assisted spray-pyrolysis method is conducted. The mass ratio of ammonium metatungstate (AMT) as a WO_3 source and titanium isopropoxide (TTIP) as a TiO_2 source was varied: $0/100$; $10/90$; $25/75$; $55/45$; $70/30$; and $100/0$. Increases in the AMT amount lead to the production of smaller-sized particle down to 20 nm . Photocatalytic analysis showed that the performance of the prepared particles was proportional to that of AMT amount. Therefore, UV-Vis spectrophotometer was used to measure the change of light absorbance. It was found that an increase in AMT amount shifted the light wavelength from 371 (blue region) to 416 nm (red region), resulted in the reduction of band gap energy. It can be concluded that the improvement of photocatalytic performance was influenced by the changes of particle size and band gap energy.

A rapid synthesis of nanostructured macroporous WO_3 particles via spray-drying process with colloidal template is introduced in **Chapter 4**. ATP and 230 nm of polystyrene (PS) particles were used to produce spherical macroporous WO_3 particles. This research is one of strategies to develop efficient catalyst because the entire surface area of the particles can be activated by light illumination effectively. The mass ratio of PS/ATP was varied from 0.00 to 0.64 to generate particles with highly ordered-porous structure. Macroporous WO_3 particles prepared with mass ratio of 0.60 shows the highest photocatalytic performance. This work presents simple process for designing nanostructured macroporous material with controllable porous structure.

In **Chapter 5**, a facile route to deposit Pt NPs on the surface of nanostructured macroporous WO_3 particles via in-situ process is discussed. High photocatalytic performance of porous WO_3 particles containing Pt NPs as a co-catalyst material is investigated in this chapter. The nanostructured Pt/ WO_3 particles were prepared by spray-drying of a precursor solution containing WO_3 NPs (10 nm), Pt salt, and PS particles (250 nm) at 600°C . The results of morphology characterizations showed that Pt

NPs were distributed on the particle surface with the size around 2 nm. The best photocatalytic activity was achieved for catalyst particles prepared at a PS/WO₃ mass ratio of 0.32 and Pt NPs of 0.23 wt%, whereby the photodecomposition rate was more than 5 times higher than that WO₃ NPs.

A general conclusion of all topics and some suggestions for further investigation were listed in **Chapter 6**.

Contents

| | |
|--|------------|
| Abstract | i |
| Contents | iv |
| List of Figures | vii |
| List of Tables | xii |
| | |
| 1. Introduction | 1 |
| 1.1 Introduction..... | 1 |
| 1.2 Semiconductor Photocatalyst..... | 4 |
| 1.2.1 Tungsten trioxide (WO ₃)..... | 5 |
| 1.3 Synthesis of Nanostructured WO ₃ Particles..... | 5 |
| 1.3.1 Flame spray pyrolysis (FSP)..... | 7 |
| 1.3.2 Spray pyrolysis/drying..... | 8 |
| 1.4 Objectives and Outline of the Dissertation..... | 9 |
| 1.5 References..... | 12 |
| | |
| 2. Controllable Crystallite and Particle Sizes of WO₃ Particles Prepared by a Spray-Pyrolysis Method and Their Photocatalytic Activity | 17 |
| 2.1 Introduction..... | 17 |
| 2.2 Experimental..... | 18 |
| 2.2.1 Synthesis of WO ₃ particles..... | 18 |
| 2.2.2 Characterizations..... | 19 |
| 2.3 Result and Discussion..... | 20 |
| 2.3.1 Effect of synthesis temperature on physicochemical of WO ₃ Properties..... | 20 |
| 2.3.2 Effect of initial precursor concentration..... | 28 |
| 2.3.3 Investigation of effect of particle and crystallite sizes on photocatalytic performance..... | 33 |
| 2.3.4 Investigation of effect of crystallite size on photocatalytic Performance..... | 34 |
| 2.4 Conclusions..... | 37 |
| 2.5 References..... | 38 |
| | |
| 3. Synthesis of Composite WO₃/TiO₂ Nanoparticles by Flame-Assisted Spray Pyrolysis and Their Photocatalytic Activity | 40 |
| 3.1 Introduction..... | 40 |

| | |
|--|-----------|
| 3.2 Experimental..... | 42 |
| 3.2.1 Raw material..... | 42 |
| 3.2.2 Preparation of WO ₃ /TiO ₂ nanocomposite particles..... | 42 |
| 3.2.3 Characterization..... | 44 |
| 3.3 Result and Discussion..... | 44 |
| 3.3.1 Synthesis of composite WO ₃ /TiO ₂ nanoparticles..... | 44 |
| 3.3.2 Evaluation of the photocatalytic activity of the prepared composite particles..... | 50 |
| 3.4 Conclusions..... | 55 |
| 3.5 References..... | 55 |
| | |
| 4. Synthesis of Spherical Macroporous WO₃ Particles and Their High Photocatalytic Performance..... | 59 |
| 4.1 Introduction..... | 59 |
| 4.2 Experimental..... | 62 |
| 4.2.1 Raw material..... | 62 |
| 4.2.2 Preparation of macroporous WO ₃ particles..... | 62 |
| 4.2.3 Characterization..... | 63 |
| 4.3 Result and Discussion..... | 64 |
| 4.3.1 Investigation of physicochemical properties of raw materials and prepared particles..... | 64 |
| 4.3.2 Effect of PS/ATP mass ratio on porous structure inside WO ₃ | 65 |
| 4.3.3 Effect of precursor concentration on porous particle outer diameter..... | 71 |
| 4.3.4 Enhancement of material performance by porous structure Formation..... | 73 |
| 4.4 Conclusion..... | 78 |
| 4.5 References..... | 78 |
| | |
| 5. Influence of Porous Structurization and Pt Addition on the Improvement of Photocatalytic Performance..... | 82 |
| 5.1 Introduction..... | 82 |
| 5.2 Experimental..... | 83 |
| 5.2.1 Preparation of spherical macroporous Pt-modified WO ₃ particles..... | 83 |
| 5.2.2 Characterization..... | 84 |
| 5.3 Result and Discussion..... | 87 |
| 5.3.1 Physicochemical properties of raw material..... | 87 |
| 5.3.2 Preparation of spherical macroporous Pt-modified WO ₃ particles..... | 87 |
| 5.3.3 Photocatalytic performance of WO ₃ particles..... | 93 |
| 5.3.4 Correlation between particle morphology, added Pt, and photocatalytic activity..... | 95 |
| 5.3.4.1 Effect of particle morphology..... | 98 |
| 5.3.4.1.1. Spherical dense particles..... | 101 |

| | |
|--|------------|
| 5.3.4.1.2. Spherical particles prepared from aggregated nanoparticles..... | 101 |
| 5.3.4.1.3. Porous-structured particles..... | 103 |
| 5.3.4.2 Effect of added Pt..... | 104 |
| 5.4 Conclusion..... | 107 |
| 5.5 Nomenclature..... | 108 |
| 5.6 Reference..... | 108 |
| 6. Summary..... | 112 |
| 6.1 Conclusions..... | 112 |

List of Figures

| | | |
|-----------|---|----|
| Fig. 1.1. | Energy level of semiconductor material. | 5 |
| Fig. 1.2. | Experimental setup of flame-assisted spray-pyrolysis. | 8 |
| Fig. 1.3. | Experimental setup of spray-pyrolysis. | 9 |
| Fig. 1.4. | Organization and structure of chapters in the present dissertation | 10 |
| Fig. 2.1. | Schematic illustration of experimental setup. | 19 |
| Fig. 2.2. | XRD patterns of particles prepared with various synthesis temperatures at constant initial concentration of 10 mmol/L. | 21 |
| Fig. 2.3. | SEM images of particles prepared at various synthesis temperatures: (a) 600; (b) 700; (c) 800; (d) 900; (e) 1000; (f) 1050; (g) 1100; (h) 1200; and (e) 1300°C. Particles were produced using 10 mmol/L of ATP. | 22 |
| Fig. 2.4. | TEM images of particles prepared with precursor concentration of 10 mmol/L ATP under different synthesis temperatures: (a) 700; (b) 800; (c) 900; (d) 1200; and (e) 1300°C. | 23 |
| Fig. 2.5. | (a) Nitrogen adsorption and desorption of particles prepared under different synthesis temperatures, (b) pore size distribution analysis. | 24 |
| Fig. 2.6. | TG-DTA analysis and Photograph images in the course of thermal decomposition of ammonium tungstate pentahydrate process. | 26 |
| Fig. 2.7. | SEM images and XRD patterns in the course of thermal decomposition of ammonium tungstate pentahydrate. | 27 |
| Fig. 2.8. | Mechanism of the formation of particles in spray-pyrolysis method as the effect of various synthesis temperatures. | 29 |
| Fig. 2.9. | SEM images of particles prepared with various initial precursor concentrations: (a) 2.5; (b) 5; (c) 10; (d) 15 mmol/L at 900°C. Particles were produced using 10 mmol/L of ATP. | 30 |

| | | |
|------------|---|----|
| Fig.2.10. | SEM images of particles prepared with various initial precursor concentrations under synthesis temperature at 1200°C: (a) 2.5; (b) 5; and (c) 15 mmol/L. | 31 |
| Fig. 2.11. | XRD patterns of particles prepared with various precursor concentrations at constant synthesis temperature: (a) 900°C and (b) 1200°C. | 32 |
| Fig. 2.12. | Comparison of the particle diameter between experimental and theoretical calculation. | 33 |
| Fig. 2.13. | Photodegradation of RhB by WO ₃ particles with various particle sizes. | 34 |
| Fig. 2.14. | Photodecomposition of RhB by WO ₃ particles with various crystal sizes. | 35 |
| Fig. 2.15. | Effect of synthesis temperatures on particle sizes (d_p), surface area (S_{BET}), crystallite sizes (d_C), and photodecomposition rates (k). | 36 |
| Fig. 3.1. | Experimental set up of flame-assisted spray-pyrolysis. | 43 |
| Fig. 3.2. | XRD patterns of particles prepared with various compositions of AMT and TTIP. | 45 |
| Fig. 3.3. | SEM images of particle prepared with various compositions aof AMT and TTIP: (a) 0:100, (b) 10:90, (c) 25:75, (d) 55:45, (e) 70:30, and (f) 100:0 wt%. | 47 |
| Fig. 3.4. | Effect of AMT amount on particle size, and surface area of the prepared particles. | 48 |
| Fig. 3.5. | Particle size distribution of nanocomposite prepared with carious mass ratio of AMT and TTIP: (a) 0:100, (b) 10:90, (c) 25:75, (d) 55:45, (e) 70:30, and (f) 100:0 wt%. | 48 |
| Fig. 3.6. | TEM images ((a1),(b1),(c1),(d1)) and HRTEM images ((a2),(b2),(c2),(d2)) of nanocomposite particles prepared with | 49 |

| | | |
|------------|---|----|
| | various composition of AMT and TTIP. Sample (a1,a2), (b1,b2),(c1,c2), and (d1,d2) were prepared using AMT and TTIP (wt%): 10:90; 25:75; 70:30; and 100:0, respectively. | |
| Fig. 3.7. | UV-Vis absorbance spectra of the particles prepared with various compositions AMT and TTIP. | 51 |
| Fig. 3.8. | Photodegradation profiles of 10 ppm amaranth with various amounts of AMT. C and C ₀ are the concentration of amaranth at the initial and measured times, respectively. | 52 |
| Fig. 3.9. | The effect of AMT amount in the physical chemical properties of particles. | 53 |
| Fig. 3.10. | The proposal photocatalytic mechanism of particle containing WO ₃ and TiO ₂ . | 54 |
| Fig. 4.1. | TGA results for PS/ATP, PS only, and ATP only. | 65 |
| Fig. 4.2. | Nitrogen adsorption analysis of prepared particles (a) and pore size distribution analysis using the BJH method (b). | 66 |
| Fig. 4.3. | Schematic diagram of mechanism of porous WO ₃ particle formation during spray-pyrolysis. | 67 |
| Fig. 4.4. | XRD patterns of particles prepared using various PS/ATP mass ratios. | 68 |
| Fig. 4.5. | SEM images of particles prepared using different PS/ATP mass ratios: (a) 0.00; (b) 0.13; (c) 0.27; (d) 0.40; (e) 0.54; (f) 0.60; and (g) 0.64. | 69 |
| Fig. 4.6. | Three-dimensional tomography images of particles prepared using different PS/ATP mass ratios: (a) 0.27 and (b) 0.60. | 71 |
| Fig. 4.7. | Effect of PS/ATP mass ratio on proposed particle formation mechanism. | 72 |
| Fig. 4.8. | TEM images of particles prepared using various PS/ATP mass | 74 |

- ratios, (a) 0.00, (b) 0.40, and (c) 0.60, in a total precursor concentration of 10 g/L; (d) and (e) are low-magnification TEM images of samples (PS/ATP mass ratio 0.60) prepared using total precursor concentrations of 10 and 100 g/L, respectively.
- Fig. 4.9. Photodegradation of RhB over time by WO_3 particles with various PS/ATP mass ratios. Empirically determined rate constants for each particle type are also given as k values. Insets: (i) molecular structure of RhB and (ii) digital camera photographs of RhB before and after photocatalytic process using WO_3 prepared using a PS/ATP mass ratio of 0.60. 75
- Fig. 5.1. Schematic illustration of the spray-drying apparatus. 86
- Fig. 5.2. Typical electron microscopy images of the raw materials used in this study: (a, c) WO_3 nanoparticles and (b, d) PS spheres. SEM and TEM images are shown in (a, b) and (c, d), respectively. 88
- Fig. 5.3. TG–DTA analysis of “ WO_3 nanoparticles only”, “PS/ WO_3 ”, and “PS only” samples. 89
- Fig. 5.4. SEM images of the spray-dried particles: (a) prepared from ATP and (b–e) prepared using varying PS/ WO_3 mass ratios of 0.00, 0.24, 0.32, and 0.40, respectively. Figures (f–g) are the high-resolution TEM images of macroporous particles with the PS/ WO_3 mass ratio of about 0.32. 90
- Fig. 5.5. XRD patterns of the as-prepared particles using varying compositions of PS and Pt addition in the precursor. 91
- Fig. 5.6. STEM image of prepared particle and corresponding elemental mapping images showing the presence of W, O, and Pt elements in the sample. 92
- Fig. 5.7. Proposed formation mechanism of the spherical macroporous Pt-modified WO_3 particles. 94

| | | |
|------------|---|-----|
| Fig. 5.8. | Photodegradation profiles of RhB in the absence of catalyst (dotted line) and the presence of various WO ₃ -based catalysts. | 96 |
| Fig. 5.9. | Recyclability performance of aggregated particles with macroporous and Pt addition for photodegradation of RhB. | 96 |
| Fig. 5.10. | Nitrogen adsorption of the prepared particles. | 98 |
| Fig. 5.11. | Proposed interaction mechanism between water molecules and surface active sites on WO ₃ catalyst with different sizes and structures: (a) dense particles with a smooth surface; (b) aggregated particles (prepared from nanoparticles); and (c) aggregated particles with macropores. | 99 |
| Fig. 5.12. | Illustration of the effect particle morphology on the surface area. | 105 |
| Fig. 5.13. | Proposed photocatalysis mechanism operating in the presence of a Pt-modified WO ₃ particle system. | 106 |

List of Tables

| | | |
|------------|--|-----|
| Table 1.1. | Relative powers of chemical oxidant. | 2 |
| Table 1.2. | Summary of the use of WO ₃ semiconductor for photocatalyst in 5 years. | 6 |
| Table 3.1. | Crystallite size of the prepared particles with various concentrations of AMT and TTIP. | 46 |
| Table 3.2. | STEM and elemental mapping images of particles prepared with various amounts of AMT. Scale bars are 100 nm. | 50 |
| Table 4.1. | TEM Images of Particles Prepared Using Different Mass Ratios of PS/ATP and Predicted PS Arrangements in the Particles. | 70 |
| Table 4.2. | BET Surface Areas and Photocatalysis Rate Constants (Determined Empirically from Photodegradation of RhB) of Different Types of WO ₃ Particles. | 76 |
| Table 5.1. | Composition of raw materials used in the precursors. | 85 |
| Table 5.2. | Photodecomposition rate constants determined experimentally and surface area ratios calculated using a geometric model. | 97 |
| Table 5.3. | Prediction of surface area based on geometrical model. | 100 |

Chapter 1

Introduction

1.1 Introduction

The rapid growth of industry to meet the human needs has also brought a side effect of serious environment issues. For example, several toxic chemicals released from textile industry have polluted ground water. As the most precious natural resource in the world and directly linked to human health, it is become an urgent need to find the solution to recovery the polluted water. Therefore, the removal of those harmful matters from industry waste water is the key issue. So far, there are numerous water treatment methods that have been introduced and it can be classified into biological, chemical, and physical oxidation process [1]. Biological treatment is the cheapest method to recovery polluted water. However, the use of bacteria to decompose organic pollutant promotes deoxygenation process and produce toxic pollutant as a side reaction, while physical treatment is not feasible to decompose organic pollutant, because post treatment is required. Furthermore, a simple and low cost process to effectively decompose organic pollutant is highly desired [2].

Advanced oxidation process (AOPs) is one of chemical treatment to remove organic materials in water using oxidation process and involving hydroxyl radical ($\bullet\text{OH}$). OH radical with an oxidation potential of 2.8 V is an extraordinary reactive species. Therefore, this process can eliminate various potentially harmful compounds which cannot be effectively removed by neither biological nor physical processes. The list of common chemical oxidants is shown in **table 1.1**. In AOPs, OH radical can be produced from three different ways: ozonation (O_3), reaction with H_2O_2 , and photocatalytic process. Since the H_2O_2 and O_3 are expensive reactants, photocatalytic process by utilizing solar energy becomes the most promising method [3-5].

Photocatalytic process can be defined as an acceleration of chemical reaction in the presence of light and semiconductor metal oxide as catalyst [6]. The utilization of solar energy as an abundant source for photocatlytic is very interesting. The advantages of photocatalytic method are: 1) the use of a renewable and pollutant-free solar energy

as an energy source, 2) no harmful side reactions product, and 3) possibility to be applied in aqueous- and gas-phase treatment. Thus, photocatalytic has attracted a great attention from fundamental science, engineering, and industrial point of views.

Table 1.1 Relative powers of chemical oxidants.

| Compound | Oxidation Potential (Volts) | Relative Oxidizing Power (Cl ₂) = 1.0 |
|-------------------|--------------------------------|--|
| Hydroxyl radical | 2.80 | 2.10 |
| Sulfate radical | 2.60 | 1.90 |
| Ozone | 2.10 | 1.50 |
| Hydrogen peroxide | 1.80 | 1.30 |
| Permanganate | 1.70 | 1.20 |
| Chlorine dioxide | 1.50 | 1.10 |
| Chlorine | 1.40 | 1.00 |
| Oxygen | 1.20 | 0.90 |
| Bromine | 1.10 | 0.80 |
| Iodine | 0.76 | 0.54 |

The photocatalytic process begins with the absorption of the suitable radiation energy followed by the formation of electrons (e^-) and holes (h^+) in conduction band (CB) and valence band (VB), respectively [7].



where MO is semiconductor metal oxide. Photogenerated e^- will be used to reduce O_2 into superoxide radical ion (O_2^-), while photogenerated h^+ will oxidize water molecule (H_2O) and produce hydroxyl (OH) radical. Both generated O_2^- and OH radicals are then used to decompose organic pollutant [8]. The detail of chemical reactions are shown as follows:



Photodegradation of organic molecules in photocatalytic process under illuminated fitted the Langmuir-Hinshelwood (L-H) kinetics models [9].

$$r = \frac{a}{a} = \frac{k}{1+K} \quad (1.6)$$

where r is the oxidation rate of the reactant (mg/L min), C is the concentration of the reactant (mg/L), t is the illumination time (min), k is the reaction rate constant (mg/L min), and K is adsorption coefficient of the reactant (L/mg). The equation can be simplified to an apparent first-order equation:

$$\ln\left(\frac{C_0}{C}\right) = kKt = k_a t \quad (1.7)$$

The important phenomenon that should be considered during photocatalytic process is the high speed of recombination process of the e^- - h^+ pairs. It is because of the speed of reduction process (10^{-9} s) is lower than the oxidation process (10^{-8} - 10^{-3} s) [10-12]. Therefore, the question on how to avoid the rapid combination of separated photogenerated e^- and h^+ during photocatalytic is rising. To solve this problem, the prospective photocatalyst should have the major requirements: i) wide light spectrum absorption, ii) suitable band energy, iii) strong catalytic activity, iv) good stability, v) non-toxic, vi) sustainability, and vii) inexpensive [13].

Previous researchers have found that type and morphology of semiconductor material for photocatalyst greatly influences the photocatalytic performance. Titanium dioxide (TiO_2) is reported as a good photocatalyst material which has been applied in various environmental problems, especially for degradation of organic pollutant. However, TiO_2 which has a wide band gap ~ 3.2 eV only responds the UV light with a wavelength of 380 nm. Moreover, the composition UV light is less than 10% from the overall solar spectrum [14,15]. Intensive researches are carried out to modify TiO_2 to obtain a broader absorption spectrum [15]. Doping of non-metal anions can extend the absorption spectrum to visible light spectrum. However, the optical absorbance in this spectrum is still low. In addition, the recombination sites are produced, resulting in the decreasing of photocatalytic performance [15]. As an alternative of photocatalyst, tungsten trioxide (WO_3) has been proposed as a good candidate. Compare with TiO_2 , WO_3 has narrower band gap ~ 2.8 eV equal with a wavelength of 470 nm which means that it has a broader absorption spectrum and can be activated under visible light [16].

1.2 Semiconductor photocatalyst

Based on the electrical conductivity (the movement of e^- through the material), solid state material can be divided in three types: metal, semiconductor, and insulator. In metal case, CB and valence band VB are overlaps each other, resulting in the easy occupation of CB by e^- . In insulator case, e^- from the VB cannot be directly promoted to CB due to the large band gap [10]. While, in the case of semiconductor, band gap is not as wide as insulator making e^- in VB can be moved to CB. As a conclusion, semiconductor can be used as photocatalyst material.

Semiconductor photocatalyst has potential to eliminate hazardous chemical compounds. The main reasons for the use of semiconductor material are stable under aqueous conditions and resistant to photochemical degradation which makes it good as photocatalyst [11]. Furthermore, water insoluble, easy removal from the precursor solution, and can be coated on to various substrates are the other notable advantages from the semiconductor material [16]. A number of semiconductor materials are available, however, only a few of them are able for decomposition of organic molecule, namely TiO_2 , WO_3 , ZnO , CdS , ZnS , and Fe_2O_3 [17]. The energy level of a number of photocatalytic semiconductors are shown in **Figure 1.1**.

The ability of a semiconductor photocatalyst to photoinduced e^- transfer to reduce O_2 depends on the potential level of band energy. Potential level of CB band should be lower (more positive) than potential level of H_2/H_2O or O_2/O_2^- , while potential level of VB should be higher (more negative) than potential level of H_2/H_2O or O_2/O_2 . Therefore, the charge carrier recombination between photogenerated e^- and h^+ can be prevented.

1.2.1 Tungsten trioxide (WO_3)

Tungsten trioxide (WO_3) is a chemical compound which has O_2 and transition metal tungsten. WO_3 has been attracted great interest during the last few years due to its characteristics such as structural, optical and electrical properties and its potential for various applications such as catalyst material, electrochromic, or gas sensor [18,19]. It has also proven to be a promising photocatalyst for degradation organic pollutant due to its optical properties in the visible wavelength region (band gap ~ 2.8 eV). **Figure 1.1**

shows that WO_3 has a conduction band (CB) edge slightly lower than the O_2/O_2^- reduction potential, and a valence band (VB) edge much higher than the O_2/O_2^- oxidation potential, which makes WO_3 capable to efficiently photo-oxidizing of various organic compounds [17]. However, the low position of CB making this material has a low efficiency.

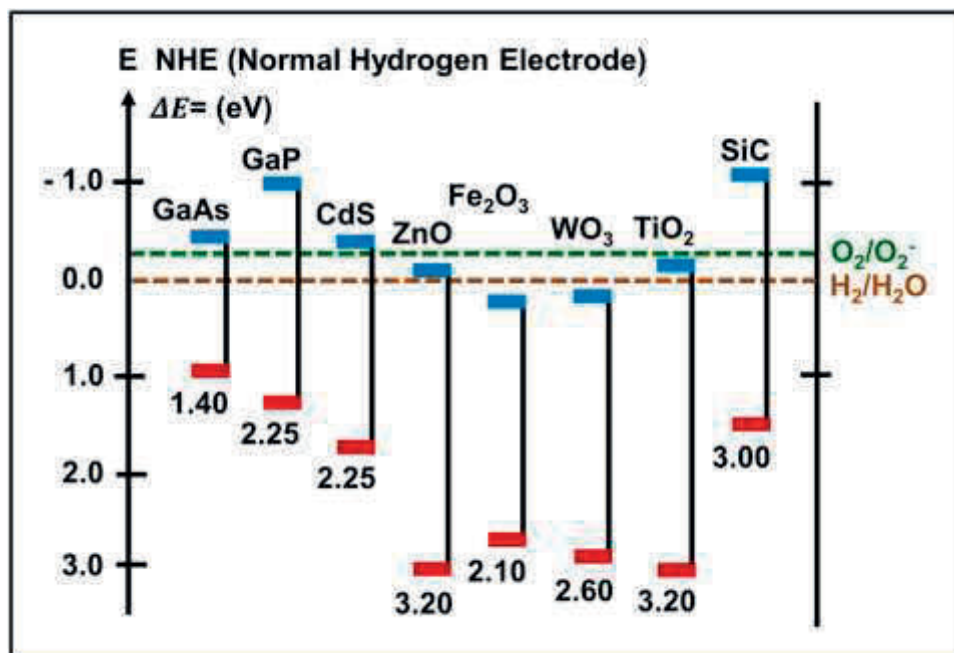


Fig. 1.1. Energy level of semiconductor material.

Furthermore, to enhance photocatalytic efficiency of WO_3 material, morphological design and additional of co-catalyst material as a trapping photogenerated e^- is necessary. The summary of the effect of particle morphology, size and composition of WO_3 prepared by various methods is shown in **Table 1.2**.

1.3 Synthesis of Nanostructured WO_3 Particles

Recently, significant effort has been devoted to synthesis WO_3 nanoparticles (NPs) using various methods, including sol-gel, hydrothermal, chemical vapor deposition, anodic oxidation method, etc. because WO_3 NPs distribute high surface area. Most reports described successful production of nanostructures WO_3 . However, their methods involve time-consuming, complicated, and multistep processes. In addition, the

morphology of the produced particle can not to be controlled using the above processes. Therefore, aerosol process was introduced to nanostructured WO₃ particles.

Table 1.2. Previous studies on synthesis of single or composite WO₃ particles for photocatalyst.

| Method | Morphology | Photocatalyst | Size (um) | Refs. |
|--------------------------|---------------------|--|-------------|-------|
| Calcination | Aggregates particle | WO ₃ | 0.05 – 0.10 | [20] |
| Flame spray pyrolysis | Nanoparticle | WO ₃ | ~ 0.01 | [21] |
| HWCVD | Nanoparticle | WO ₃ | ~ 0.07 | [22] |
| Mechanical mixing | Nanoparticle | Pd/WO ₃ | 0.05- 0.15 | [23] |
| Solvothermal | Core-shell | Fe ₃ O ₄ /WO ₃ | 1.00-5.00 | [24] |
| Simple mixing | Nanoparticle | Pt/WO ₃ | 0.13 | [26] |
| Liquid phase | Nanoparticle | Au/WO ₃ /TiO ₂ | 0.02 | [23] |
| Liquid phase | Hollow sphere | WO ₃ | 0.50 | [27] |
| Liquid phase | Mesoporous | Pt/WO ₃ | 0.15 | [28] |
| Liquid phase | Nanocomposite | WO ₃ /Bi ₃ O ₄ Cl | 1.00 | [29] |
| Liquid phase | Composite particle | InVO ₄ /WO ₃ | 0.05 – 1.00 | [30] |
| Liquid phase | Nanoparticle | WO ₃ | 0.20 | [31] |
| Liquid phase | Particle | PtPb/WO ₃ | 0.60 | [32] |
| Flame spray pyrolysis | Nanopowder | CuO/WO ₃ | 0.02 | [33] |
| Liquid phase | Nanorod | WO ₃ | 0.03 | [34] |
| Sonochemical | Composite particle | Au/SiO ₂ /WO ₃ | 0.03 | [35] |
| Microwave | Composite particle | Zn/WO ₃ | 0.05 | [36] |
| Precipitation | Composite particle | Pd/WO ₃ | ~ 0.1 | [37] |

Aerosol process has been proven as a good method to synthesis nanostructured metal oxide [38]. The produced particles can be readily used without any post processing because the obtained materials contain high purity. In addition, this process has high production rate, continuous operation, and produce particles in the nano- to

submicron-sized ranges [38]. In this dissertation, two types of heating method in aerosol process are reported to synthesis nanostructured WO_3 particles. They are flame assisted- and electric furnace-assisted spray pyrolysis method.

In general, both flame spray and spray pyrolysis apparatus contains three main of experimental parts: atomizer, heating zone, and particles collecting system [39]. Ultrasonic nebulizer (UN) has been used as an atomizer for generating droplet. The advantages of this droplet generator are produces small droplet with narrow size distribution, spherical of droplet, high liquid flow, and low pressure of fluids flow. The produced droplet size from UN is varied from 1 to 7 μm [40].

In flame-assisted spray-pyrolysis (FASP) apparatus, burner is used as a heating source, while in spray pyrolysis/drying using electric furnace. For particle collecting system, there are three types of particles collector that were used in this experiment, i.e. electrostatic precipitator, bag filter, and paper filter. The electrostatic precipitator was connected to the high voltage of DC electric to capture the particle with efficiency is around 20%. Different to electrostatic precipitator, bag filter is utilizing very small pore to collect the particles, have a higher efficiency which is around 60%. Paper filter shows the highest efficiency, around 80%.

1.3.1 Flame-assisted spray-pyrolysis (FSP)

Flame aerosol technology is widely employed for large-scale manufacture of nanomaterial. The advantages of FSP process are its capability to produce mixed metal oxide powder with high production rates, high crystallinity, dense and impurities-free due to heating in high temperature [41]. However, the drawback of this process is produce NPs agglomerated [42]. Detail apparatus system is shown in **Figure 1.2**.

In FSP process, the temperature on the flame zone can be controlled by adjusting the fuel gas and oxidant flow rate. Methane gas (CH_4) and O_2 gas have been used as a fuel gas and oxidant, respectively. The fuel gas was introduced via a burner, which consists of three concentric cylinders. The inner part was used to introduce precursor to the flame zone. CH_4 and O_2 gas were supplied to the burner through second and third annulus, respectively. In this zone, the physical and chemical process of

particles formation occurred and it was determined by fuel gas flow rate. After that, the as-prepared particles were then collected by bag filter with the aid of vacuum pump.

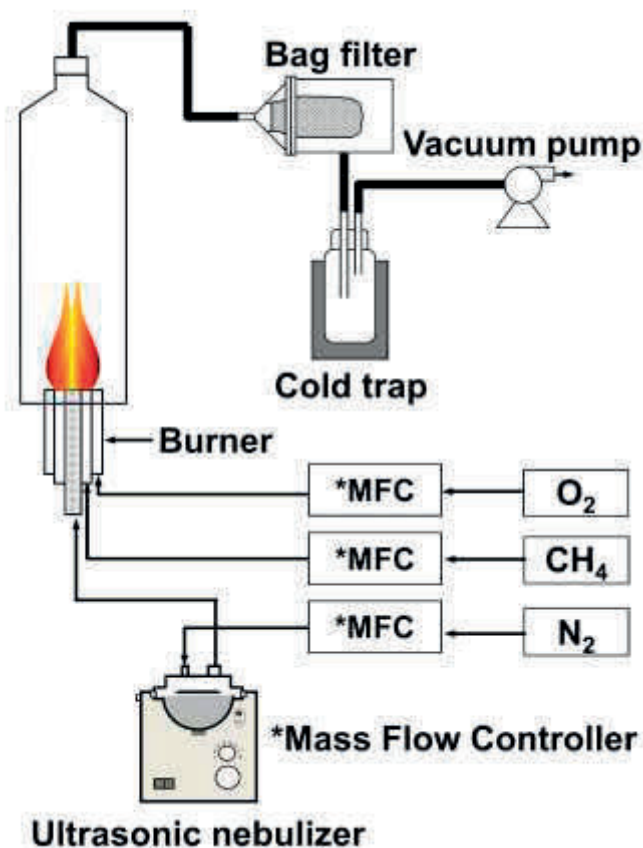


Fig. 1.2. Experimental setup of flame-assisted spray-pyrolysis.

1.3.2 Spray pyrolysis/drying

Similar with FASP, both spray pyrolysis and drying are the one-droplet-to-one-particle (ODOP) and one-droplet-to-many-particles (ODMP) methods [42]. Those methods have a similar basic principle, a particle is produced from a single droplet that undergoes solvent evaporation by heating. It causing the remaining components in droplet to precipitate after the mixture reaches a super-saturated state. Morphology of the produced particles is strongly depends on the characteristics of precursor, droplet size, and operating condition. Different with spray-drying method, a chemical decomposition at elevated temperatures occurs in spray pyrolysis method [43]. Correlation between precursor concentration and predicted final particle size can be written as

$$D_p = D_d \left[\sum \frac{C_i M_i}{\rho} \right]^{1/3} \quad (1.8)$$

Where D_p , D_d , C_d , M , ... denote the average particle diameter, the average droplet diameter, the precursor concentration, the molecular weight, and the particle mass density, respectively [41] Detail apparatus system is shown in **Figure 1.3**.

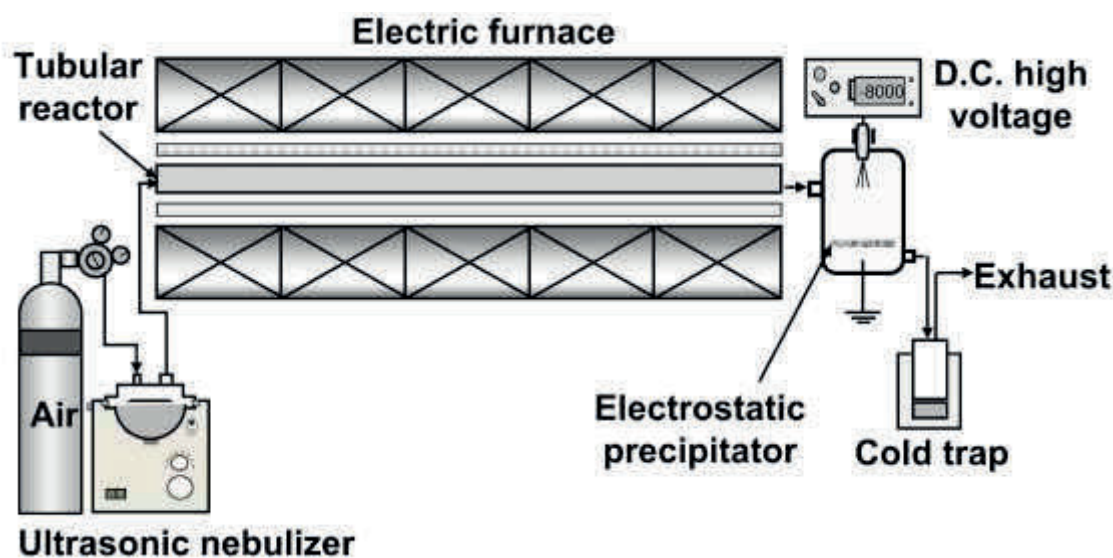


Fig. 1.3. Experimental setup of spray pyrolysis.

1.4 Objectives and Outline of the Dissertation

The main objectives of this dissertation are: (1) investigation of the effect of both particle and crystallite sizes of WO_3 material on photocatalytic performance, (2) Optimization of photocatalytic performance of WO_3 material by synthesis of composite WO_3/TiO_2 nanoparticles (NPs), synthesis of nanostructured macroporous WO_3 particles, and deposition of Pt Nps on nanostructured macroporous WO_3 particles. To investigate the photocatalytic activity, Rhodamine B (RhB) and amaranth have been used as the model of organic pollutants. This dissertation comprise of 6 chapters. The schematic diagram of dissertation organization is shown in **Figure 1.4**. The brief descriptions of each chapter are shown below.

Chapter 1 describes the background and motivation of current research. Basic theoretical explanation and review of previous researches on photocatalyst materials, especially WO_3 particles were also provided.

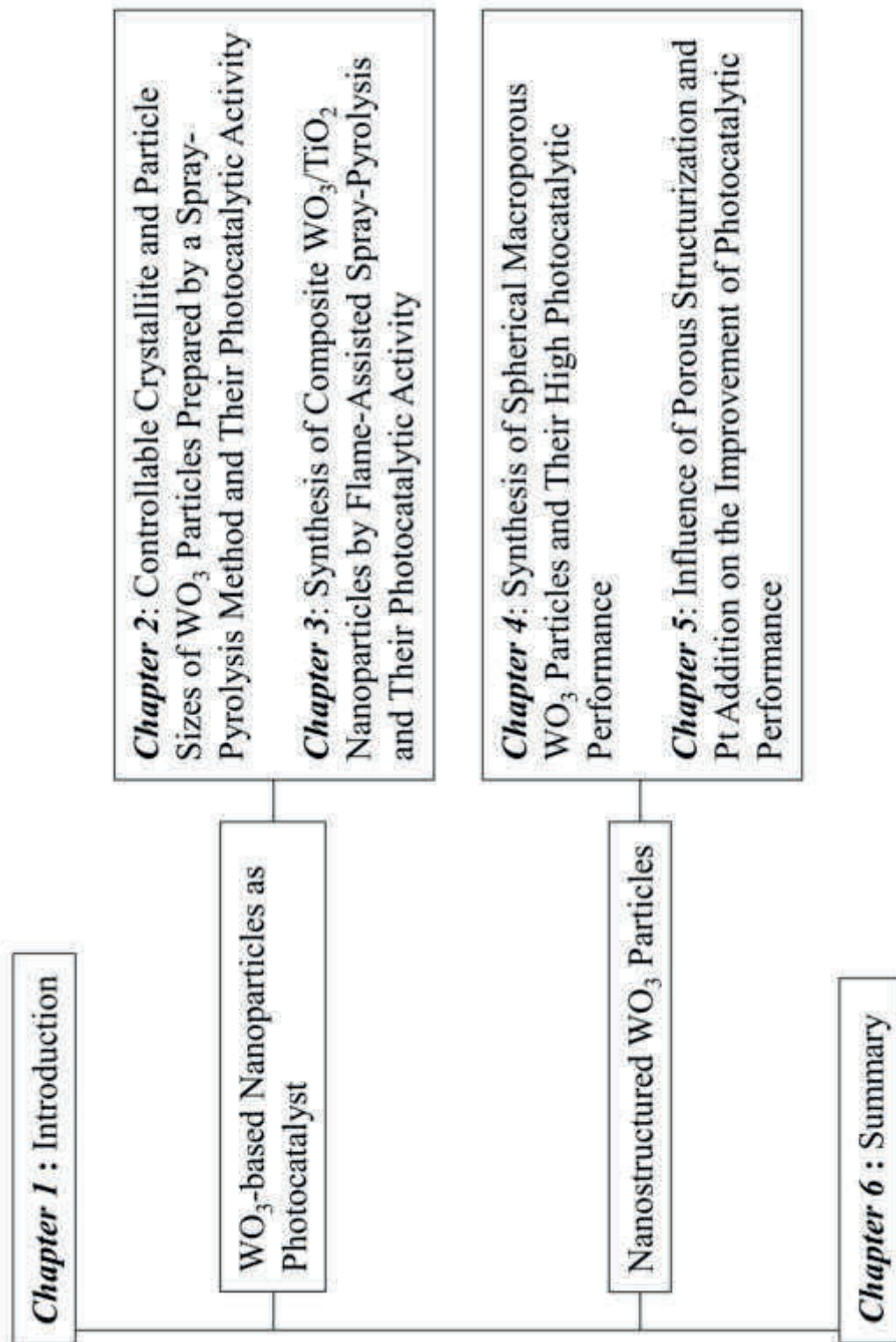


Fig. 1.4. Organization and structure of chapters in the present dissertation.

Synthesis and evaluation of WO_3 particles with controllable crystallite and particle sizes using spray-pyrolysis method is described in detail in **Chapter 2**. Ammonium tungstate pentahydrate (ATP) has been used as WO_3 source because conversion of this chemical into WO_3 is free of impurities. To control crystallite/particles size, synthesis temperatures and precursor concentrations were varied from 120 to 1300°C and from 2.5 to 15 mmol/L, respectively. The possible mechanism of WO_3 particle formation was proposed and divided in two processes based on the range of synthesis temperature: 1) pretreatment process (120-600°C), and 2) crystallization process (600-1300°C). The results showed that crystalline WO_3 particles was produced when the synthesis temperature was 600°C or higher. The production of WO_3 nanoparticles (NPs) was started when the synthesis temperature above 900°C due to the evaporation and condensation process. It was found that the synthesis temperature has more significant effect on the change of particles morphology and crystallinity than precursor concentration. The detail correlation between particle morphology and kinetic photodecomposition rate is examined. The results showed that both crystallite and particle sizes played an important role in photocatalytic activity to decompose RhB. Thus, the optimum condition to produce WO_3 particles with the highest photocatalytic performance was at the synthesis temperature of 1200°C (crystal size: 25 nm), and precursor concentration 10 mmol/L (particle size: 105 nm).

Detail investigation on the effect of WO_3/TiO_2 composite on photocatalytic performance is discussed in **Chapter 3**. Composite WO_3/TiO_2 NPs have been successfully synthesized by flame-assisted spray-pyrolysis method. The mass ratio of ammonium metatungstate (AMT) as a WO_3 source and titanium isopropoxide (TTIP) as a TiO_2 source was varied: 0/100; 10/90; 25/75; 55/45; 70/30; and 100/0. The elemental mapping analysis showed that the prepared particles contained O, W, and Ti. It was found that color intensities inside the prepared particles were well-distributed, confirming that the prepared particles contained WO_3 and TiO_2 . In addition, the effect of mass ratio on the change of energy band gap was also analyzed. The results showed that deviation ratio for (band gap)/(AMT) was (0.19 eV)/(25 wt%) higher than deviation ratio for higher concentration of AMT above 25 wt % ((0.18 eV)/(75 wt%)). The

improvement of photocatalytic performance was influenced by physicochemical properties of composite WO_3/TiO_2 NPs.

Chapter 4 introduces a rapid synthesis of nanostructured macroporous WO_3 particles via spray-drying process. Precursor contained ATP and 230 nm of polystyrene (PS) particles were spray dried at 700°C to produce spherical macroporous WO_3 particles. The mass ratio of PS/ATP was varied from 0.00 to 0.64 to control porous structure. It was found that photodecomposition rate was proportional to the mass ratio of PS/ATP. Particles with porous structure have better photooxidation (2.5 times) than those without porous structure due to better interaction between molecules and light in the deepest part of the active catalyst.

In order to produce macroporous WO_3 particles with a higher photocatalytic performance, Pt nanoparticles was deposited via in situ process. The detail description of this topic is explained in **Chapter 5**. The nanostructured Pt/ WO_3 particles were prepared by spray-drying of a precursor containing WO_3 NPs (10 nm), Pt salt, and PS particles (250 nm) at 600°C . Photocatalytic results showed that the changes in particle morphology and added Pt NPs effectively improved the photocatalytic performance 5 times higher than that of WO_3 NPs. The current strategy is a gateway toward designing materials with excellent performance but using relatively low amounts of raw materials.

Chapter 6 contains the summary of all chapters and direction for further investigation.

1.5. References

- [1] Chong, M. N.; Jin, B.; Chow, C. W.; Saint, C., Recent developments in photocatalytic water treatment technology: a review. *Water Research*, 44 (2010) 2997-3027.
- [2] Dapeng, L.; Jiuhui, Q., The progress of catalytic technologies in water purification: A review. *Journal of Environmental Sciences*, 21 (2009) 713-719.
- [3] Matilainen, A.; Sillanpää, M., Removal of natural organic matter from drinking water by advanced oxidation processes. *Chemosphere*, 80 (2010) 351-365.
- [4] Andreozzi, R.; Caprio, V.; Insola, A.; Marotta, R., Advanced oxidation processes (AOP) for water purification and recovery. *Catalysis Today*, 53 (1999) 51-59.

- [5] Oller, I.; Malato, S.; Sánchez-Pérez, J., Combination of advanced oxidation processes and biological treatments for wastewater decontamination-a review. *Science of the Total Environment*, 409 (2011) 4141-4166.
- [6] Yang, J.; Wang, D.; Han, H.; Li, C., Roles of cocatalysts in photocatalysis and photoelectrocatalysis. *Accounts of Chemical Research*, 46 (2013) 1900-1909.
- [7] Fan, W.; Zhang, Q.; Wang, Y., Semiconductor-based nanocomposites for photocatalytic H₂ production and CO₂ conversion. *Physical Chemistry Chemical Physics*, 15 (2013) 2632-2649.
- [8] Li, J.; Wu, N., Semiconductor-based photocatalysts and photoelectrochemical cells for solar fuel generation: a review. *Catalysis Science & Technology*, 5 (2015) 1360-1384.
- [10] Friedmann, D.; Mendive, C.; Bahnemann, D., TiO₂ for water treatment: parameters affecting the kinetics and mechanisms of photocatalysis. *Applied Catalysis B: Environmental*, 99 (2010) 398-406.
- [11] Chen, X.; Shen, S.; Guo, L.; Mao, S. S., Semiconductor-based photocatalytic hydrogen generation. *Chemical Reviews*, 110 (2010) 6503-6570.
- [12] Carraway, E. R.; Hoffman, A. J.; Hoffmann, M. R., Photocatalytic oxidation of organic acids on quantum-sized semiconductor colloids. *Environmental science & technology*, 28 (1994) 786-793.
- [13] Hoffman, A. J.; Carraway, E. R.; Hoffmann, M. R., Photocatalytic production of H₂O₂ and organic peroxides on quantum-sized semiconductor colloids. *Environmental science & technology*, 28 (1994) 776-785.
- [14] Ahmed, S.; Rasul, M.; Martens, W. N.; Brown, R.; Hashib, M., Advances in heterogeneous photocatalytic degradation of phenols and dyes in wastewater: a review. *Water, Air, & Soil Pollution*, 215 (2011) 3-29.
- [15] Fujishima, A.; Rao, T. N.; Tryk, D. A., Titanium dioxide photocatalysis. *Journal of Photochemistry and Photobiology C: Photochemistry Reviews*, 1 (2000), 1-21.
- [16] Fujishima, A.; Zhang, X., Titanium dioxide photocatalysis: present situation and future approaches. *Comptes Rendus Chimie*, 9 (2006) 750-760.

- [17] Chacón, C.; Rodríguez-Pérez, M.; Oskam, G.; Rodríguez-Gattorno, G., Synthesis and characterization of WO₃ polymorphs: monoclinic, orthorhombic and hexagonal structures. *Journal of Materials Science: Materials in Electronics*, 1-6.
- [18] Li, X.; Wen, J.; Low, J.; Fang, Y.; Yu, J., Design and fabrication of semiconductor photocatalyst for photocatalytic reduction of CO₂ to solar fuel. *Science China Materials*, 57 (2014), 70-100.
- [19] Deb, S. K., Opportunities and challenges in science and technology of WO₃ for electrochromic and related applications. *Solar Energy Materials and Solar Cells*, 92 (2008) 245-258.
- [20] Granqvist, C. G., Oxide electrochromics: An introduction to devices and materials. *Solar Energy Materials and Solar Cells*, 99 (2012) 1-13.
- [21] Sayama, K.; Hayashi, H.; Arai, T.; Yanagida, M.; Gunji, T.; Sugihara, H., Highly active WO₃ semiconductor photocatalyst prepared from amorphous peroxotungstic acid for the degradation of various organic compounds. *Applied Catalysis B: Environmental*, 94 (2010) 150-157.
- [23] Pokhrel, S.; Birkenstock, J.; Schowalter, M.; Rosenauer, A.; Mädler, L., Growth of ultrafine single crystalline WO₃ nanoparticles using flame spray pyrolysis. *Crystal Growth & Design*, 10 (2009) 632-639.
- [24] Iliev, V.; Tomova, D.; Rakovsky, S.; Eliyas, A.; Puma, G. L., Enhancement of photocatalytic oxidation of oxalic acid by gold modified WO₃/TiO₂ photocatalysts under UV and visible light irradiation. *Journal of Molecular Catalysis A: Chemical*, 327 (2010), 51-57.
- [25] Liu, Y.; Ohko, Y.; Zhang, R.; Yang, Y.; Zhang, Z., Degradation of malachite green on Pd/WO₃ photocatalysts under simulated solar light. *Journal of hazardous materials*, 184 (2010) 386-391.
- [26] Xi, G.; Yue, B.; Cao, J.; Ye, J., Fe₃O₄/WO₃ Hierarchical Core-Shell Structure: High - Performance and Recyclable Visible - Light Photocatalysis. *Chemistry-A European Journal*, 17 (2011) 5145-5154.
- [26] White, C. M.; Jang, J. S.; Lee, S. H.; Pankow, J.; Dillon, A. C., Photocatalytic Activity and Photoelectrochemical Property of Nano-WO₃ Powders Made by Hot-

- Wire Chemical Vapor Deposition. *Electrochemical and Solid-State Letters*, 13 (2010) B120-B122.
- [27] Shiraishi, Y.; Sugano, Y.; Ichikawa, S.; Hirai, T., Visible light-induced partial oxidation of cyclohexane on WO_3 loaded with Pt nanoparticles. *Catalysis Science & Technology*, 2 (2012) 400-405.
- [28] Xi, G.; Yan, Y.; Ma, Q.; Li, J.; Yang, H.; Lu, X.; Wang, C., Synthesis of multiple - shell WO_3 hollow spheres by a binary carbonaceous template route and their applications in visible - light photocatalysis. *Chemistry-A European Journal*, 18 (2012) 13949-13953.
- [29] Huang, H.; Yue, Z.; Song, Y.; Du, Y.; Yang, P., Mesoporous tungsten oxides as photocatalysts for O_2 evolution under irradiation of visible light. *Materials Letters*, 88(2012) 57-60.
- [30] Chakraborty, A. K.; Kebede, M. A., Preparation and characterization of $\text{WO}_3/\text{Bi}_3\text{O}_4\text{Cl}$ nanocomposite and its photocatalytic behavior under visible light irradiation. *Reaction Kinetics, Mechanisms and Catalysis*, 106 (2012), 83-98.
- [31] Zhang, F.; Zhao, W.; Zhang, K., Enhanced photocatalytic activity by the tunnel effect of microstructured $\text{InVO}_4/\text{WO}_3$ heterojunctions. *Reaction Kinetics, Mechanisms and Catalysis*, 108 (2013), 253-261.
- [32] Amano, F.; Ishinaga, E.; Yamakata, A., Effect of particle size on the photocatalytic activity of WO_3 particles for water oxidation. *The Journal of Physical Chemistry C*, 117 (2013) 22584-22590.
- [33] Gunji, T.; Tsuda, T.; Jeevagan, A. J.; Hashimoto, M.; Kaneko, S.; Tanabe, T.; Matsumoto, F., Site-Selective Deposition of Ordered Intermetallic PtPb Nanoparticle Co-Catalysts on WO_3 Surfaces to Enhance Photocatalytic Activity. *ECS Transactions*, 61 (2014), 55-59.
- [34] Lee, J.; Gouma, P. I., Flame - Spray - Processed $\text{CuO}-\text{WO}_3$ Nanopowders as Photocatalysts. *Journal of the American Ceramic Society*, 97 (2014), 3719-3720.
- [35] DePuccio, D. P.; Botella, P.; O'Rourke, B.; Landry, C. C., Degradation of Methylene Blue Using Porous WO_3 , SiO_2-WO_3 , and Their Au-Loaded Analogs: Adsorption and Photocatalytic Studies. *ACS applied materials & interfaces*, 7 (2015), 1987-1996.

- [36] Madhan, D.; Parthibavarman, M.; Rajkumar, P.; Sangeetha, M., Influence of Zn doping on structural, optical and photocatalytic activity of WO₃ nanoparticles by a novel microwave irradiation technique. *Journal of Materials Science: Materials in Electronics* 2015, 1-8.
- [37] Gondal, M. A.; Dastageer, M. A.; Khalil, A. B.; Rashid, S. G.; Baig, U., Photocatalytic deactivation of sulfate reducing bacteria—a comparative study with different catalysts and the preeminence of Pd-loaded WO₃ nanoparticles. *RSC Advances*, 5 (2015) 51399-51406.
- [38] Okuyama, K.; Lenggoro, I. W., Preparation of nanoparticles via spray route. *Chemical Engineering Science*, 58 (2003) 537-547.
- [39] Arutanti, O.; Ogi, T.; Nandiyanto, A. B. D.; Iskandar, F.; Okuyama, K., Controllable crystallite and particle sizes of WO₃ particles prepared by a spray - pyrolysis method and their photocatalytic activity. *AIChE Journal*, 60 (2014) 41-49.
- [40] Wang, W.-N.; Purwanto, A.; Lenggoro, I. W.; Okuyama, K.; Chang, H.; Jang, H. D., Investigation on the correlations between droplet and particle size distribution in ultrasonic spray pyrolysis. *Industrial & Engineering Chemistry Research*, 47 (2008), 1650-1659.
- [41] Arutanti, O.; Nandiyanto, A. B. D.; Ogi, T.; Iskandar, F.; Kim, T. O.; Okuyama, K., Synthesis of composite WO₃/TiO₂ nanoparticles by flame-assisted spray pyrolysis and their photocatalytic activity. *Journal of Alloys and Compounds*, 591 (2014) 121-126.
- [42] Pratsinis, S. E., Flame aerosol synthesis of ceramic powders. *Progress in Energy and Combustion Science*, 24 (1998), 197-219.
- [43] Arif, A. F.; Balgis, R.; Ogi, T.; Mori, T.; Okuyama, K., Experimental and theoretical approach to evaluation of nanostructured carbon particles derived from phenolic resin via spray pyrolysis. *Chemical Engineering Journal*, 271 (2015), 79-86.

Chapter 2

Controllable Crystallite and Particle Sizes of WO₃ Particles Prepared by a Spray-Pyrolysis Method and Their Photocatalytic Activity

2.1. Introduction

Tungsten trioxide (WO₃) is one of the most prospective catalysts because it possesses many excellence properties (e.g. good photo-stability, excellent absorption of solar radiation (visible light), biologically and chemically inert, good thermal stability, etc) [1, 2]. However, there are several problems regarding to availability and price of WO₃.³ For this reason, preparation of WO₃ material with high photocatalytic activity and lower tungsten usage is inevitable [4-10].

To produce WO₃ material with excellent performances, many methods have been reported. However, most of the current reports are in film form,² while reports in the synthesis of particles are typically less. In fact, implementation of photocatalyst films in large-scale industrial processes is difficult. For circumventing the problems associated with the production of WO₃ particles, several methods have been suggested, including sol-gel, hydrothermal, chemical vapor deposition, sputtering, and anodic oxidation [4,7,9,11,12]. Although their methods are able to produce particles, most reports described successful production of particles with only partial information on controlling crystallite and particle sizes, as well as their impact on photocatalytic activity.

Information about correlations between material properties parameter (i.e. crystallite and particle sizes) and photocatalytic activity of WO₃ particles are still lacking. Most reports did not discriminate the influence of "crystallite with a constant particle size" or "particle size with a constant crystallite size" on photocatalytic activity.

In fact, investigation of WO₃ particles with controllable crystallite and particle sizes is important.

In our previous studies, we synthesized WO₃ particles with controllable particle size [13], composition (adding Pt dopant) [14], and porous structure [3]. However, we did not report in detail about the influence of crystallite size yet. Here, the purpose of this study was to synthesize WO₃ particles with controllable crystallite and particle sizes and to investigate the correlation of crystallite/ particle size and photocatalytic activity.

To produce WO₃ particles, we used a spray-pyrolysis method because this method can produce agglomeration-free particles [15, 16]. Thus, the effect of crystallite and particle sizes on photocatalytic performance can be investigated precisely. We selected ammonium tungstate pentahydrate (ATP) as a model for WO₃ source because conversion of this chemical into WO₃ is free of impurities [3]. Detailed investigation of the effect of synthesis temperature and precursor concentration was also presented along with the proposal of the particle formation mechanism, in which this information is typically disregarded in the current WO₃ particle synthesis reports. Interestingly, the present method was effective to control crystallite and particle size only by changing synthesis temperature and precursor concentration. To support our study, we used electron microscopes, x-ray diffraction, nitrogen sorption, and thermal analysis.

We also investigated the effect of crystallite and particle sizes on photocatalytic performance. As a model for organic waste, we used rhodamine B (RhB). RhB had high photostability and water solubility rather than other dyes (e.g. methylene blue), making this chemical difficult to be degraded using conventional waste water treatment methods. RhB is also one of the most used dyes in industrial applications, making that the successful treatment of this chemical can be directly applied for realistic applications. The result showed that both crystallite and particle sizes played an important role in photocatalytic activity in degrading RhB. We also optimized the process for gaining high performance of photocatalyst, which is useful for synthesis of particles particularly with a view to screening and enhancing the material properties.

2.2 Experimental

2.2.1 Synthesis of WO₃ particles

To synthesize WO_3 particles, ATP ($(NH_4)_{10}(W_{12}O_{41}) \cdot 5H_2O$; purity 88–90%; Kanto Chemical Co., Inc., Japan) was used and diluted into ultra-pure water (UPW). The diluted ATP (namely the precursor) was then put into the particle production system, shown in **Figure 2.1**. This reactor system consist of an ultrasonic nebulizer (NE-U17; Omron Healthcare Co., Ltd., Japan; operated at 1.7 MHz; to generate droplet), a tubular ceramic reactor (1.3 m in length and 30 mm in inner diameter), and an electrostatic precipitator (10,000 V; 120°C). Detailed electrostatic precipitator is described in detail in our previous work¹⁷. To introduce the generated droplet into the tubular furnace, we used a flow of carrier gas (air; 5 L/min). To produce particles with controllable crystallite and particle sizes, we varied the synthesis temperature (from 120 to 1300°C) and the initial precursor concentration (from 2.5 to 15 mmol/L).

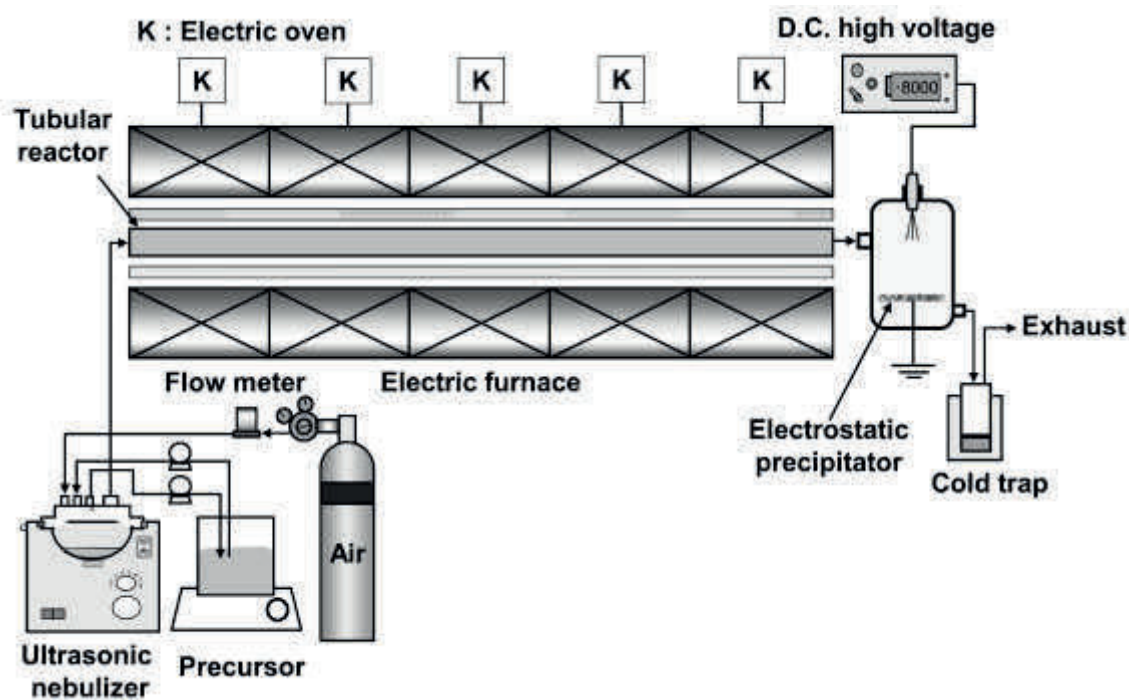


Fig. 2.1. Schematic illustration of experimental setup.

2.2.2 Characterizations

The morphology of the prepared particles were examined using a scanning electron microscope (SEM, Hitachi S-5000, Japan; operated at 20 kV), and a transmission electron microscope (TEM, JEM-3000F, Japan; operated at 300 kV). An

X-ray diffraction (XRD; RINT2000V, Rigaku Denki, Japan; using Cu K α radiation ($\lambda = 1.54 \text{ \AA}$); operated at 40 kV and 30 mA with a scan step of 0.02°) was used to evaluate the crystal structure. To determine the specific surface area, a nitrogen adsorption analysis (BET; BELSORP 28SA; Bel Japan, Japan) was used. We also analyzed sample using a thermogravimetric and differential thermal analyzer (TG-DTA; Exstar6000, Seiko Instruments Inc., Japan; heating rate = $5 \text{ }^\circ\text{C}/\text{min}$; carrier gas: air, 200 mL/min).

To investigate the photocatalytic activity of the prepared particles, the photodecomposition of RhB under solar irradiation (PEC-L11, Peccell Technologies, Inc., Japan; AM 1.5G ($100 \text{ mW}/\text{cm}^2$)) was measured. In simplification, the photodecomposition process used: 2 ppm of aqueous solution of RhB, 200 mg of prepared particles, and 500 mL of UPW. To maintain concentration dissolved oxygen in the solution, 200 mL/min of oxygen gas was bubbled into the reactor. Detailed photodegradation system is described in our previous work [3]. To measure the concentration of remained RhB, sample was taken and analyzed using a UV-Vis spectrophotometer (UV3150, Shimadzu, Japan; evaluated in the wavelength range of 400 – 700 nm at room temperature).

2.3 Results and discussions

2.3.1 Effect of synthesis temperature on physicochemical of WO₃ properties

To investigate the effect of synthesis temperature on particles formation precisely, we used precursor with concentration of 10 mmol/L because this concentration is appropriate to produce submicron particles, based on our previous work [3]. Too high concentration has problems in the ATP solubility in water, whereas too low precursor concentration caused less production rate.

Figure 2.2 shows the XRD patterns of spray-pyrolyzed particles prepared with various synthesis temperatures (600 to 1300°C). The XRD patterns suggested that the prepared particles had two types of crystal structures: hexagonal (JCPDS no. 75-2187) and monoclinic (JCPDS no. 72-1465). The hexagonal structure was prepared at a synthesis temperature of around 600°C . A mixture of monoclinic and hexagonal structures was formed at higher synthesis temperatures from $700 - 1050^\circ\text{C}$. The crystal structure changed to hexagonal structure at temperature of above 1050°C . From the

Scherer equation, the crystallite size increased from 18 to 41 nm with the increasing of synthesis temperatures from 600 to 1000°C. The crystallite sizes were 37, 29, 25, and 23 nm in corresponding to the synthesis temperature of 1050, 1100, 1200, and 1300°C, respectively.

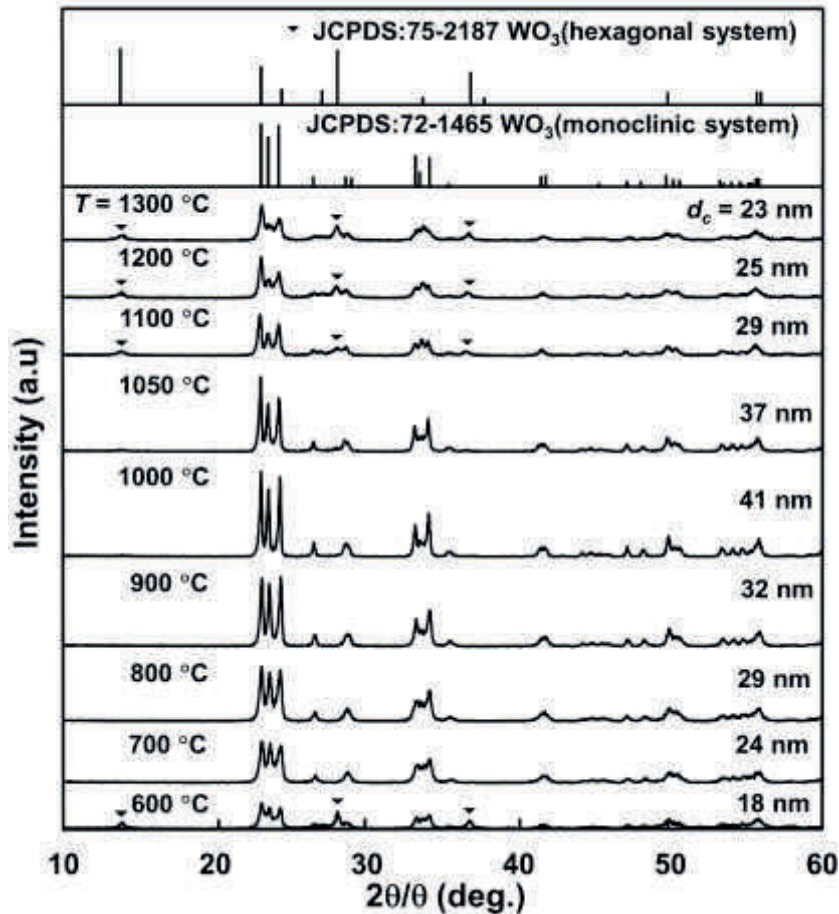


Fig.2.2. XRD patterns of particles prepared with various synthesis temperatures at constant initial concentration of 10 mmol/L.

Figure 2.3 shows the SEM images of the particles prepared at various synthesis temperatures from 600 to 1300°C. In the range of 600 and 1000°C, the prepared particles were in spherical shape with a mean particle size of about 500 nm (Figure 2.3(a)-(e)). The increasing of temperature further to 1050°C led the decreasing in particle size to around 488 nm (Figure 2.3(f)). The size of the prepared particles greatly

decreased to 177 nm, 105 nm, and 87 nm, corresponding to the synthesis temperature of 1100, 1200, and 1300°C, respectively (**Figure 2.3(g)-(i)**).

Figure 2.4 shows the TEM analysis of particles prepared at various synthesis temperatures (from 700 to 1300°C). **Figure 2.4(a)** shows that when using a synthesis temperature of 700°C, particles with a spherical shape are produced. The observation of outer morphology gained by TEM results were in a qualitative agreement with the SEM results in **Figure 2.3b**. When the temperature was increased to 800°C, particles with

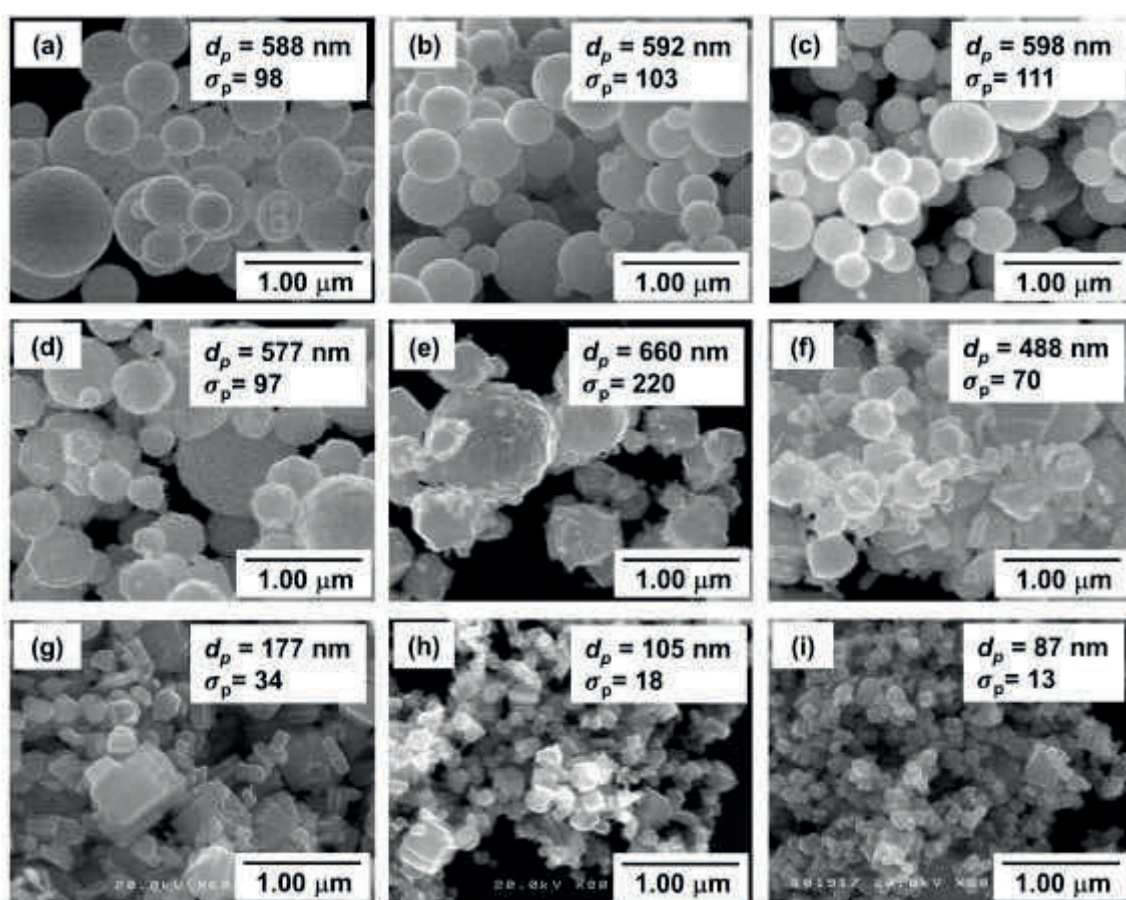


Fig. 2.3. SEM images of particles prepared at various synthesis temperatures: (a) 600; (b) 700; (c) 800; (d) 900; (e) 1000; (f) 1050; (g) 1100; (h) 1200; and (e) 1300°C.

Particles were produced using 10 mmol/L of ATP.

a rough surface were generated (**Figure 2.4(b)**). As the calcination temperature was increased to 900°C, incomplete spherical particles with a highly faceted shape were

produced (**Figure 2.4(c)**). The use of higher synthesis temperatures, changes in the particle morphology were observed (**Figure 2.4(d)-(e)**). Synthesis temperatures of 1200 and 1300°C gave the creation of hexagonal shaped nanoparticles. The lattice fringe spacing of WO_3 particles was 5.18; 4.62; 5.05; 5.17; and 5.03 Å, corresponding to synthesis temperatures 700, 800, 900, 1200 and 1300°C, respectively.

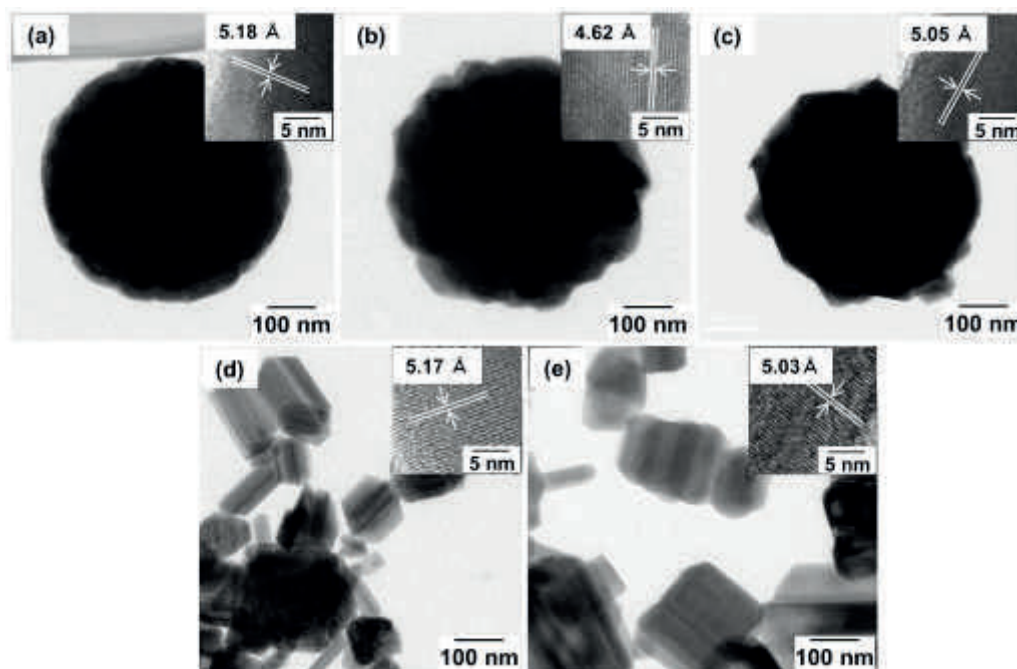


Fig. 2.4. TEM images of particles prepared with precursor concentration of 10 mmol/L ATP under different synthesis temperatures: (a) 700; (b) 800; (c) 900; (d) 1200; and (e) 1300°C.

To clarify the structure inside the particles, a nitrogen adsorption analysis was conducted shown in the **Figure 2.5**. The analysis showed that all particles exhibited a characteristic type-II isotherm (**Figure 2.5(a)**), indicating the prepared particles were non-porous. The Barrett-Joyner-Halenda (BJH) method was also confirmed that no micro and mesoporous structures were identified in all samples, as shown in **Figure 2.5(b)**.

In the range of 600 to 1000°C, increase in synthesis temperature causes increase in the material crystallization, indicated by the increase in crystallite size due to the

same initial concentration of ATP. However, there is no significant change in the particle size. Further increases in the temperature cause the modification of particle outer shape. This result confirms that the higher temperature process causes the more additional energy supply for improving crystallite growth. Thus, the higher temperature leads the production of particles with larger crystallite size.

In addition, anomaly results were found for the case of particles prepared using temperatures of above 1000°C . The particle sizes decrease drastically and there is a modification in the crystal structure. WO_3 material seems to be evaporated during the process. Then, when the evaporated WO_3 components are cooled (contacting temperature of below than 1000°C), they are re-constructing, re-assembling, and coalescing to form stable crystal condition. Thus, the particles with different crystal structures are formed in the final product. Due to the limitation for the cooling time process, the particles with nanometer sizes are produced.

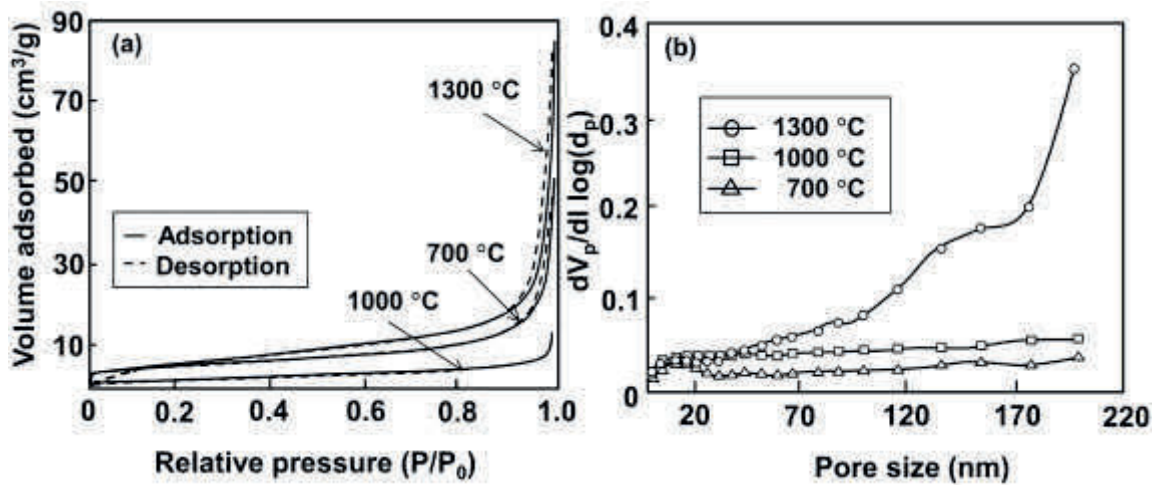


Fig. 2.5. (a) Nitrogen adsorption and desorption of particles prepared under different synthesis temperatures, (b) pore size distribution analysis.

The possibly mechanism of WO_3 particle formation during the spray-pyrolysis method is described. The mechanism is divided in two parts: (1) pretreatment ($< 600^\circ\text{C}$), and (2) crystallization ($600 - 1300^\circ\text{C}$).

In the pretreatment process, the main principle of this step is to deliver and rapidly heat an initial solution/slurry via the direct injection of very small droplets.[22] Droplets are generated from the atomization of precursor using ultrasonic nebulizer, in which these droplets are then introduced into the heated reactor. Contacting droplets with temperature of 120-300°C, solvent evaporates. Further additional temperature, thermal decomposition of ATP occurs, producing amorphous WO₃ particles. With the increase of temperature (400-600°C), these amorphous particles transform into higher crystalline WO₃ particles.

Figure 2.6 shows TG-DTA analysis of ammonium tungstate pentahydrate and SEM images of the prepared particles. However, there is a change in mass examined by the TG-DTA analysis results. In the temperature of 120°C, a mass loss of 6 wt% was found. The mass was then slightly decreasing (about 3 wt%) with the increases in temperature up to 240°C. In the range of 240 to 340°C, major decreases in the mass was found (up to 10 wt%). Then, the mass loss continued up to temperature of 500°C. However, this mass loss was relatively less (about 1 wt%). The mass was stable after applying temperature of more than 500°C. The insert of photograph images shows of the prepared particles in every step of thermal decomposition process. Samples prepared at temperatures of 120 and 240°C were white. Color started to change from white to bluish when using a temperature of 300°C. Then, a change in the color was found at 400°C, in which the color changed into blue. Further changes in color were found when using temperature of 600°C. Color transformed into yellowish green.

Figure 2.7 shows the SEM images of particles prepared at 10 mmol/L. When the synthesis temperature at 120°C, the particles sizes were 740 nm. When the synthesis temperature increase to 240°C, the particles sizes increased to 923 nm. By increasing temperature up to 300°C, the particles sizes were 890 nm. Particle size decreased to 677 nm when the synthesis temperature increased to 400°C. At high synthesis temperature, the particle sizes reduced to 562 nm. The insert of XRD patterns show that the synthesis temperature allowed material with different phases and patterns. Samples were amorphous when prepared using temperature of less than 300°C. When using 400°C, XRD peaks started to appear. Strong peaks were observed when using the temperature

of 600°C. According to JCPDS no. 76 2187, all peaks were WO₃ with hexagonal structure.

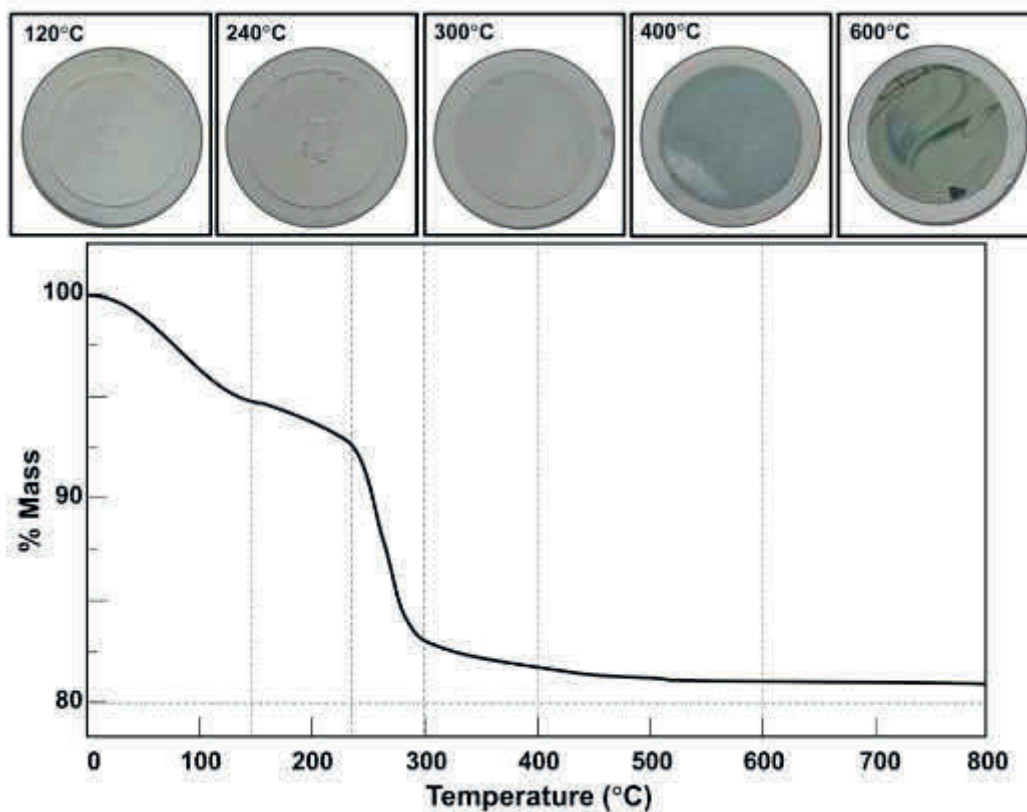


Fig.2.6. TG-DTA analysis and Photograph images in the course of thermal decomposition of ammonium tungstate pentahydrate process.

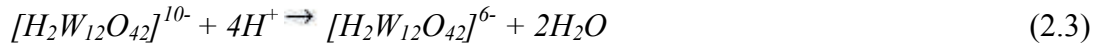
Based on above results, the formation of WO₃ particles can be described in the following [1-3]:

1. At 50 – 120°C, anhydrous compound formation occurs. During this process, most water is released, in which the simple reaction can be described using the following reaction:



2. At 120 – 240°C, paratungstate B anion formation happens. This anion is formed from the following reactions:





3. At 240 – 400°C, hydrate and ammonia are removed from the droplet. This condition leads the major degradation of mass in the droplet. In addition, as a consequence of this removal, WO₃ amorphous is formed (confirming by the appearance of XRD peaks in the sample prepared at 400°C).

At more than 500°C, WO₃ amorphous transformation occurs. This condition results the formation of WO₃ with hexagonal crystal structures (verifying by strong XRD peaks in the sample prepared at 600°C).

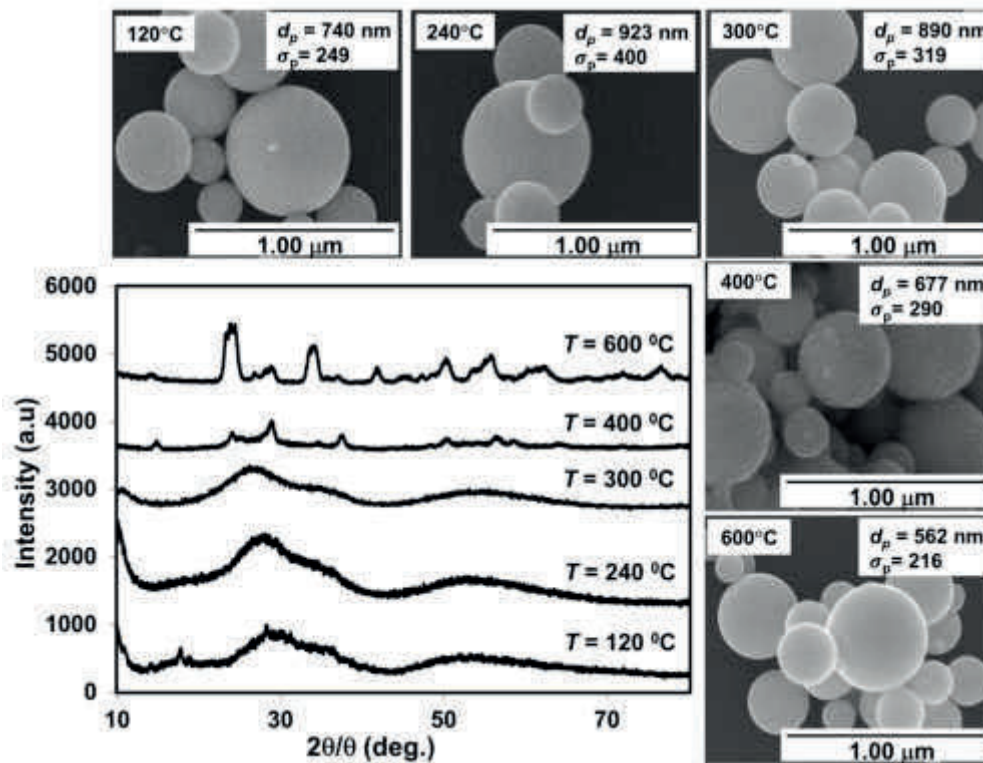


Fig. 2.7. SEM images and XRD patterns in the course of thermal decomposition of ammonium tungstate pentahydrate.

In the crystallization zone, there are two phenomena (**Figure 2.8**). One is particle synthesis with non-evaporation process (600-1000°C) and the other is particle synthesis with evaporation process (>1000°C).

The first phenomena are shown in **route R1** and **R2**. **Route R1** in **Figure 2.8** is the formation of spherical submicron particles. This can be obtained when the process is at temperature of below than 900°C. Adding a higher temperature process (between 900 and 1000°C) leads the production of submicron aspherical particles with faceted shapes (**route R2**).

When applying crystallization process with temperatures of higher than 1000°C, second phenomena happen (shown in **route R3** and **R4**). WO₃ material evaporates. When using temperature of between 1000 and 1100°C, incomplete evaporation happens (**route R3**). As a result, particles with a broad size distribution are prepared. When using temperature of higher than 1100°C (**route R4**), all products are nanoparticles.

2.3.2 Effect of initial precursor concentration

To investigate the effect of initial concentration on particle size and morphology, we selected the synthesis temperature of 900 and 1200°C, in which these temperatures can be used as a model for synthesis process with non-evaporation and evaporation phenomena, respectively.

Figure 2.9 shows the SEM images of particles prepared with various initial precursor concentrations at 900°C. Submicron particles with a spherical shape were obtained for all cases. Particles sizes increased with increasing precursor concentration. The Ferret diameters of particles (shown in **Figure 2.9(a)-(d)**) were 388, 454, 579, and 767 nm, corresponding to initial precursor concentrations of 2.5, 5, 10, and 15 mmol/L, respectively.

Figure 2.10 shows the SEM images of particles prepared with various precursor concentrations at 1200°C. A strong correlation between precursor concentration and particle size was obtained. Increases in precursor concentration affected the increases in particle size. In addition, we also found that the precursor concentration modify particle shape.

When using the precursor concentration of 2.5 mmol/L, spherical particles with a mean size of 58 nm were produced (**Figure 2.10(a)**). When the precursor concentration was increased to 5 mmol/L, a mean particle size increased to 60 nm. **Figure 2.10(b)**.

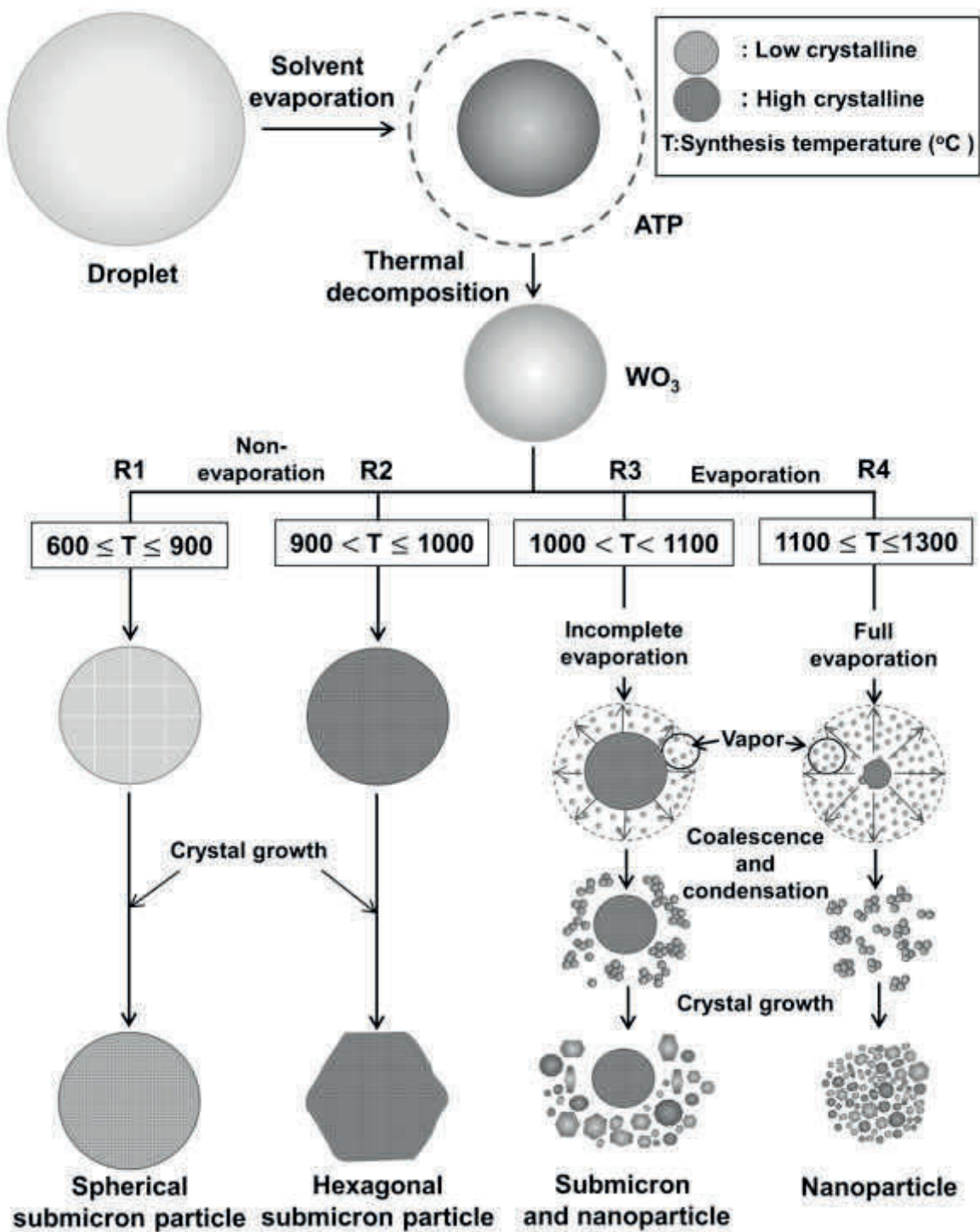


Fig. 2.8. Mechanism of the formation of particles in spray-pyrolysis method as the effect of various synthesis temperatures.

By increasing the precursor concentration to 15 mmol/L, particles with a diamond like shape and a mean size of 677 nm were created (**Figure 2.10(c)**).

In addition, we found interesting result. From above experimental result in **Figure 2.9** and **2.10**. XRD patterns of sample in **Figure 2.9** shows there is no change in XRD phase and pattern. However, XRD patterns from sample in **Figure 2.10** shows the occurrence of changes in pattern and crystallite size (18 to 50 nm). This change is due to the particle evaporation at high temperature as shown in **Figure 2.8**. All data are presented in **Figure 2.11**.

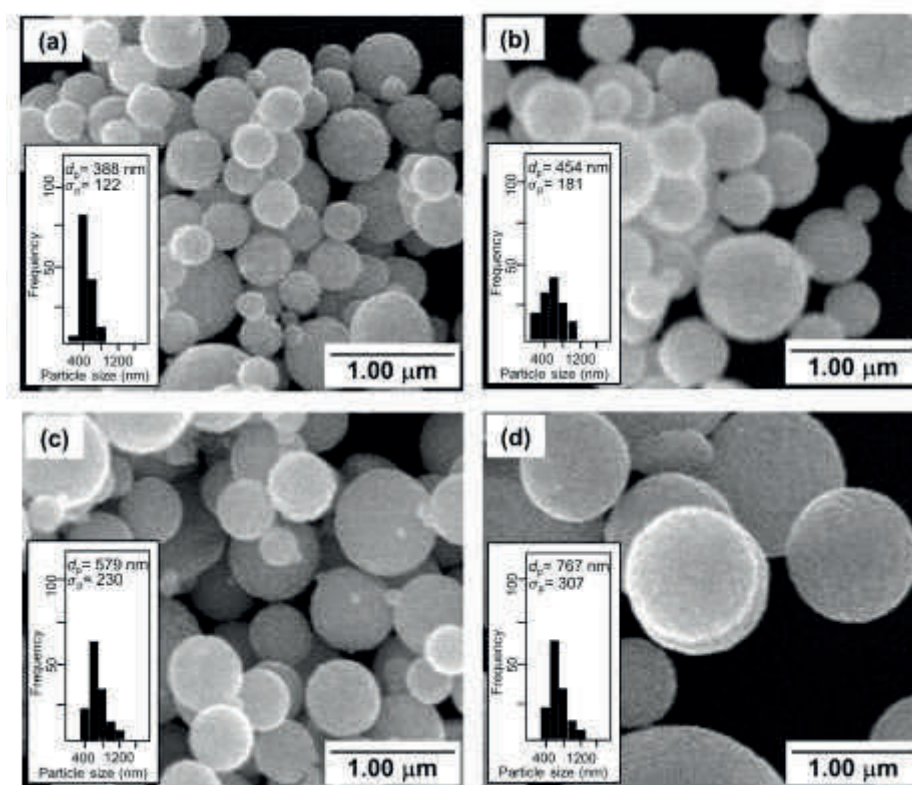


Fig. 2.9. SEM images of particles prepared with various initial precursor concentrations: (a) 2.5; (b) 5; (c) 10; (d) 15 mmol/L at 900°C. Particles were produced using 10 mmol/L of ATP.

Figure 2.12 shows effect of precursor concentration on particle size in detail with theoretical calculation result. Experimental results are shown by “solid dot” for synthesis temperature of 900°C and "solid square" for synthesis temperature of 1200°C,

whereas the theoretical calculations are shown by “dashed line”. The theoretical calculation is gained using the following equation [15]:

$$D_p = D_d C_D \left(\frac{1}{(1-\nu)} \sum_{i=1}^n \frac{M_i \cdot C_i}{\rho_i} \right)^{1/3} \quad (2.4)$$

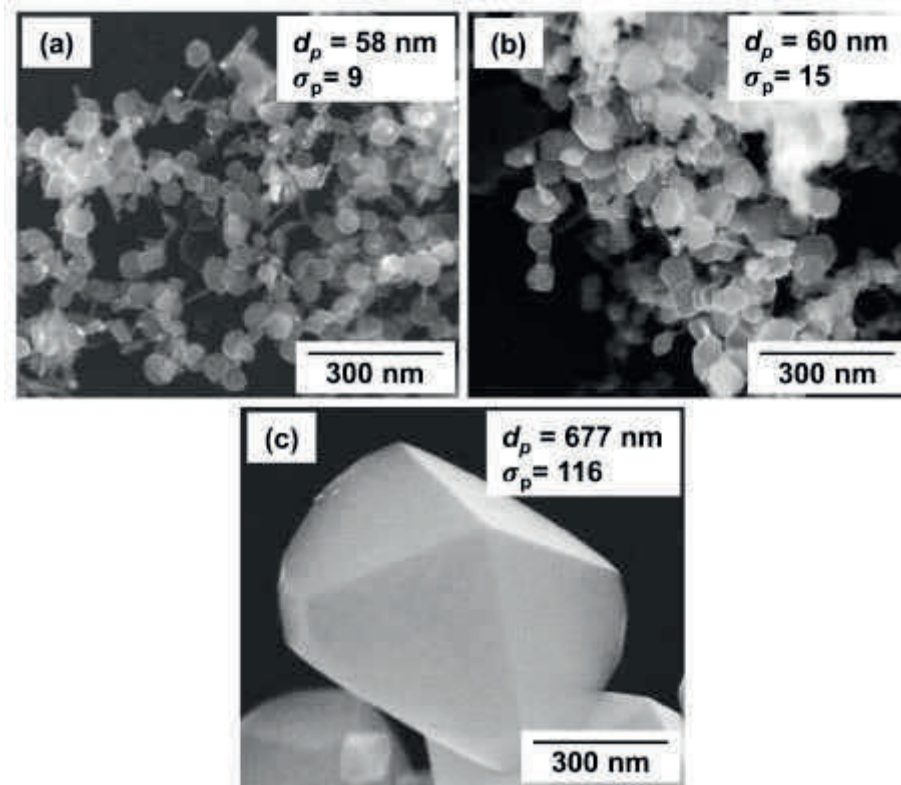


Fig.2.10. SEM images of particles prepared with various initial precursor concentrations under synthesis temperature at 1200°C: (a) 2.5; (b) 5; and (c) 15 mmol/L.

where D_p is the mean diameter of the prepared particle (μm), D_d is the mean diameter of the mean diameter of droplet (μm), C_D is the constant (0.0464), and ε is the particle porosity. M is the molecular weight, C is the initial concentration (g/L), and ρ is the density (g/mL). In the ultrasonic nebulizer, generated droplet diameter (D_d) is 4.5 μm .

The results show that increases in the precursor concentration allow the production of larger particles. For the case of temperature of 900°C, the increment of particle size is in a good agreement with theoretical analysis result. Small differences

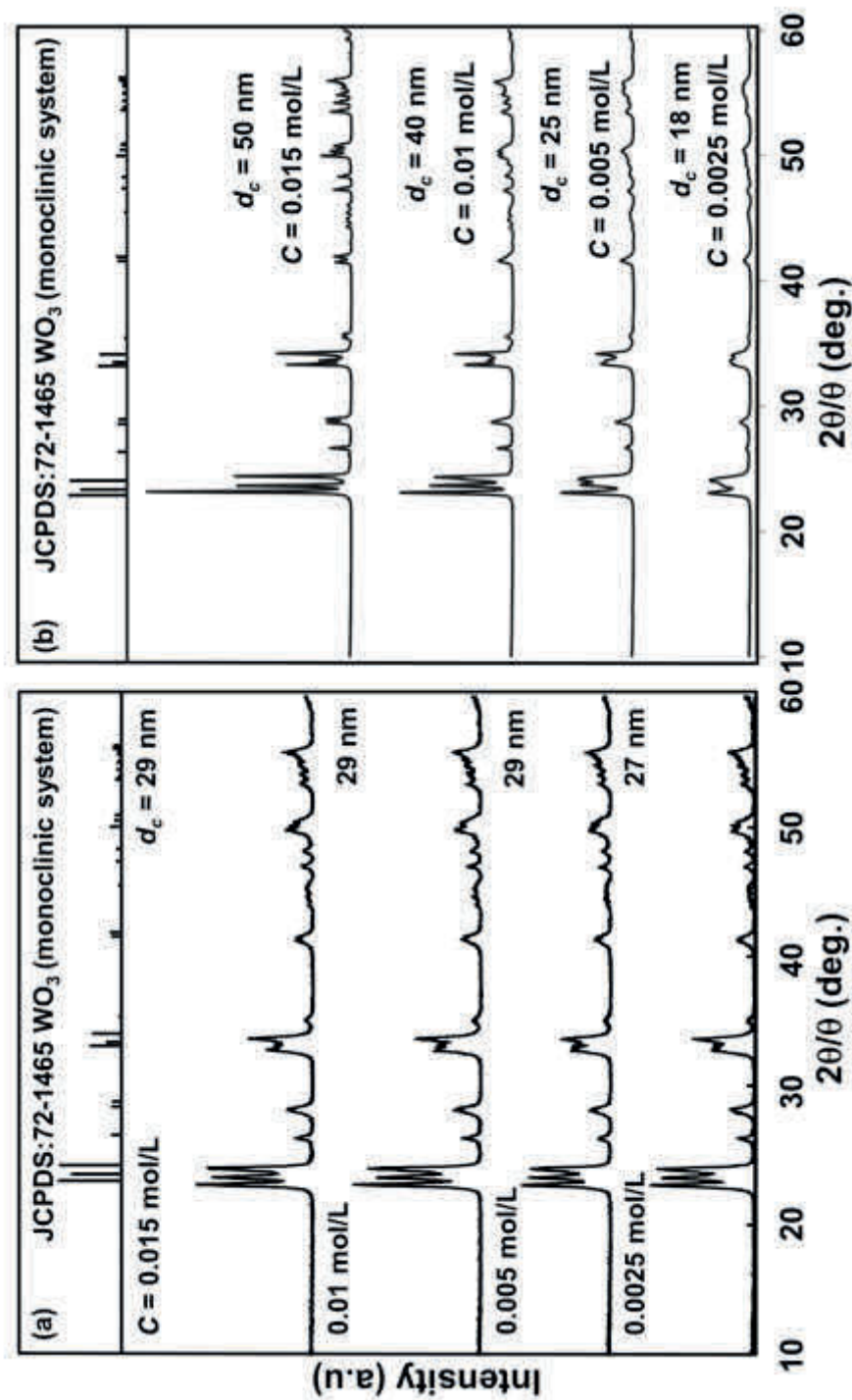


Fig. 2.11. XRD patterns of particles prepared with various precursor concentrations at constant synthesis temperature: (a) 900°C and (b) 1200°C.

are due to the existence of sintering phenomenon during the spray-pyrolysis process. However, for the case of samples prepared with temperature of 1200°C , the trend in particle size is far from theoretical analysis. This deviation is due to the existence of WO_3 material evaporation phenomena. In addition, when using high concentration at 1200°C , sizes of particles are near to that of theoretical results. There are some heat transfer problems during the spray pyrolysis process, making evaporation of WO_3 material incomplete.

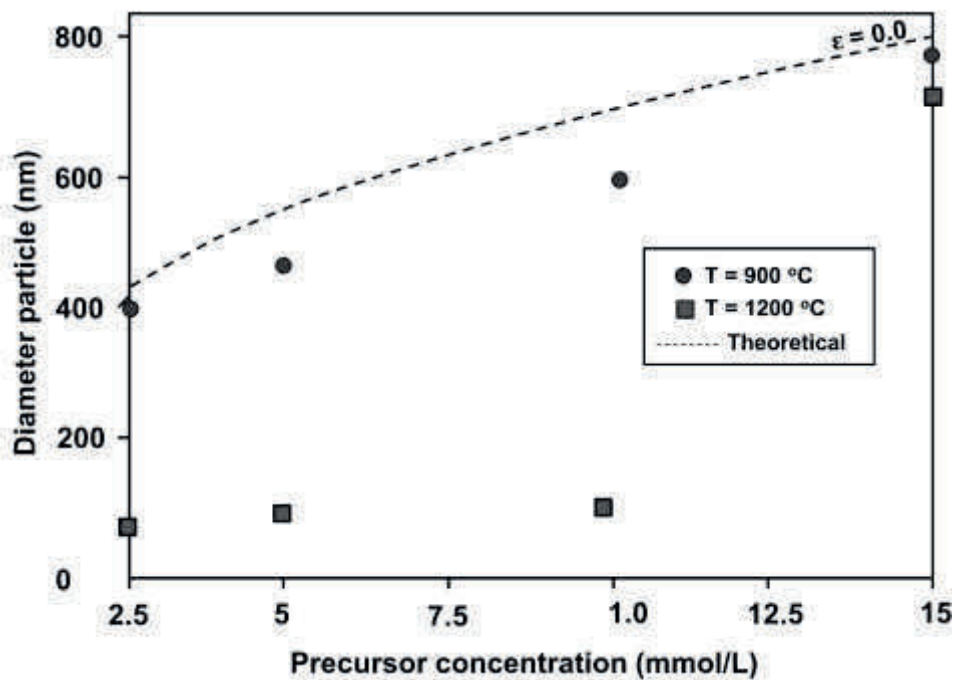


Fig. 2.12. Comparison of the particle diameter between experimental and theoretical calculation.

2.3.3 Investigation of effect of particle size on photocatalytic performance

Photodegradation of RhB using various sizes of particles is shown in Figure 2.13. The RhB concentration gradually decreased with increasing processing time (shown in solid lines), while the RhB was stable in the absence of a catalyst (shown in a dotted line). The lost RhB concentrations after 1-hour photocatalytic process were from 12 to 15 %, when using catalyst with a mean size of from 767 to 388 nm, respectively. The rate of photocatalysis (k) was the fastest for particles with a mean size of 388 nm (k

= 1.3672 min^{-1}) and the slowest for particles with a mean size of 767 nm ($k = 0.9254 \text{ min}^{-1}$). Particles with a mean size of between 388 and 767 nm had intermediate photodecomposition rates, in which particles with a mean size of 454 and 579 nm had a k value of 1.2637 and 1.1397 min^{-1} , respectively.

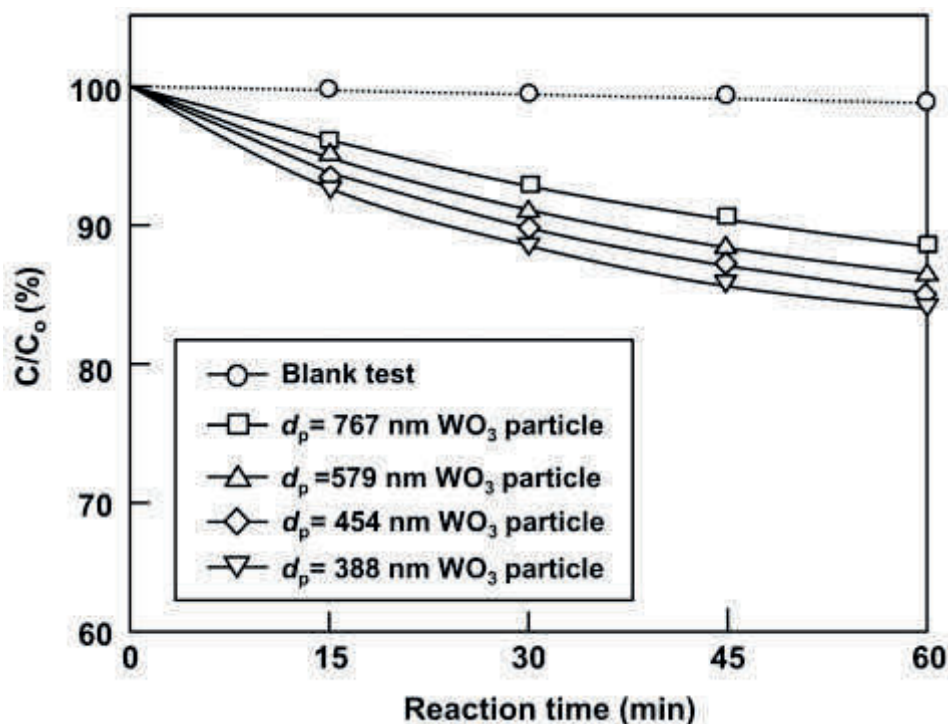


Fig.2.13. Photodegradation of RhB by WO_3 particles with various particle sizes.

The crystal phase of all catalysts were the same (shown in **Figure 2.11**), indicating that the fundamental reason for the different photocatalytic behaviors was due to the effect of the particle size. In the same weight of photocatalysts used in the tests, the particle number increases with the decrease of particle size. This condition will be followed by the increase of total surface area of the catalyst. Detailed explanation of the correlation of particle size and surface area is reported in our previous work [3].

2.3.4 Investigation of effect of crystallite size on photocatalytic performance

Photodegradation of RhB as the effect of crystallite size of particles is shown in **Figure 2.14**. Similar to above photodecomposition analysis in **Figure 2.12**, the RhB

concentration gradually decreased with increasing processing time (shown in solid and dashed lines), while RhB was stable in the absence of a catalyst (shown in a dotted line). We found that increases in crystallite size caused increasing of photodegradation rate. The lost RhB concentration after 1-hour photocatalytic process were from 8 to 34%, when using catalyst synthesized using temperature of from 600 to 1200°C. However, the lost RhB concentration was 27% when using catalyst synthesized using temperature 1300°C. The improvement of photocatalytic activity was probably because the larger crystallite size results in the more number of active sites in the catalyst. However, we found anomaly for the case of samples prepared with higher temperatures (shown as dashed lines).

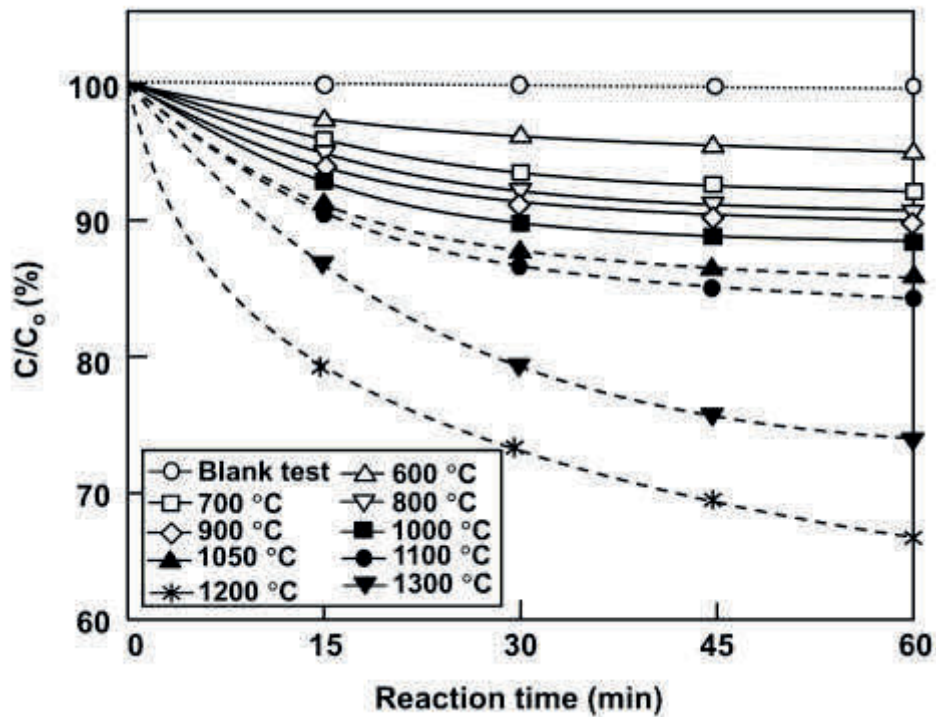


Fig. 2.14. Photodecomposition of RhB by WO_3 particles with various crystal sizes.

Figure 2.15 shows the detail correlations of synthesis temperature, particle size (d_p), surface area (S_{BET}), crystallite size (d_c), and kinetic photodecomposition rate (k). To clarify the discussion, the figure is divided into three zones, based on the synthesis

temperature: (1) 600 – 1000°C (**the first zone**), (2) 1000 – 1200°C (**the second zone**), (3) above 1200°C (**the third zone**).

In **the first zone**, increasing synthesis temperature corresponds to an increase of both crystallite size and photocatalytic activity. The particles size and the surface area are constant. Therefore, the correlation between crystallite size and photocatalytic activity can be investigated directly. It confirms that the ability of catalyst to decompose RhB increases due to increasing crystallite size.

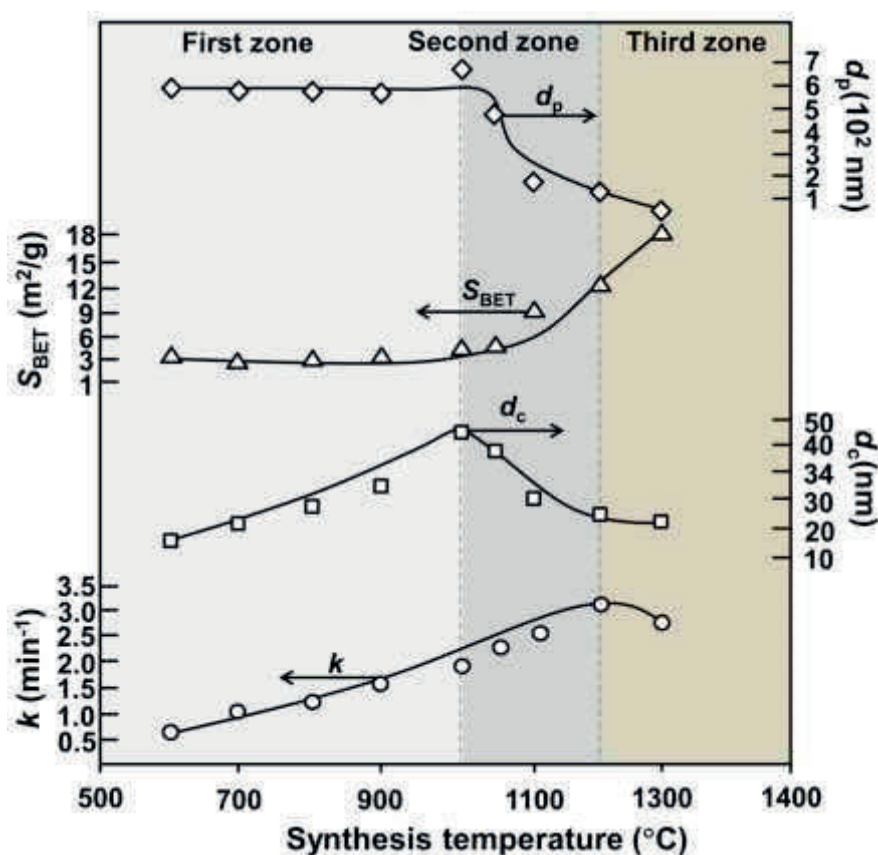


Fig.2.15. Effect of synthesis temperatures on particle sizes (d_p), surface area (S_{BET}), crystallite sizes (d_c), and photodecomposition rates (k).

In **the second zone**, both particle size and crystal size increase with the increasing of the synthesis temperature. Although the crystal size decreases, the photocatalytic activity increases. As explained in **Figure 2.8**, using high temperature of above 1000°C causes a reduction of both crystallite and particle sizes. In general,

increase of temperature process leads the production of nanoparticles (shown in **Figure 2.3** and **2.4**), in which the use of nanoparticles gives additional factors (i.e. surface area) for the improvement of photodegradation process.

In **the third zone**, although particle sizes decreases, photocatalytic activity decreases slightly. This may reflect the reason in dominance of slight decrease in crystallite size for decreasing photocatalytic performance.

In addition, the crystal size at 1300°C is similar to that at 700°C. However, the photocatalytic performances of both particle types were different. This is because of the different specific surface area of both particles.

From above results, the optimum synthesis temperature to produce the catalyst with the highest photocatalytic activity was 1200°C and using a precursor concentration of 10 mmol/L. It is also found that the synthesis temperature has a more significant effect than that precursor concentration. However, in addition to both factors, the crystal phase and structure are also influencing the photocatalytic performance. For this reason, the further studies (e.g. crystal phase and pattern, additional doping, etc.) are needed for clarifying how to improve photocatalyst. We believe that insights gained from this type of research will contribute to more fabrication innovation.

2.4 Conclusions

The studies on the controllable crystallite and particle sizes of WO₃ particles prepared by a spray-pyrolysis method and their photocatalytic performance have been reported. We controlled the crystallite (from 18 to 50 nm) and particle sizes (from 58 to 677 nm) by changing the synthesis temperature in wide range (120-1200°C) and initial precursor concentration (2.5-15 mmol/L). The capability of photocatalyst can be optimized by changing both the crystallite and the particle sizes. The optimum condition to produce the highest photocatalytic performance of WO₃ particles was at the temperature of 1200°C (crystal size: 25 nm) and initial concentration 10 mmol/L (particle size: 105 nm). The proposal mechanism was also reported to support the level of control over crystallite/particle size by the spray-pyrolysis method. Hopefully, this report is useful for synthesis of particles, particularly with a view to screening and enhancing the material properties.

2.5 References

- [1] Bhatkhande, D.S.; Pangarkar, V.G.; Beenackers, A.A., Photocatalytic degradation for environmental applications—a review. *Journal of Chemical Technology and Biotechnology*, 77(2002) 102-116.
- [2] Bertus, L.; Duta, A.; Synthesis of WO₃ thin films by surfactant mediated spray pyrolysis. *Ceramics International*, 38 (2012) 2873-2882.
- [3] Nandiyanto, A.B.D.; Arutanti, O.; Ogi, T.; Iskandar, F.; Kim, T.O., Okuyama K. Synthesis of spherical macroporous WO₃ particles and their high photocatalytic performance. *Chemical Engineering Science*, 101 (2013) 523-532.
- [4] Zheng, H.; Ou, J.Z.; Strano, M.S.; Kaner, R.B.; Mitchell, A.; Kalanta, Z.K., Nanostructured tungsten oxide—properties, synthesis, and applications. *Advanced Functional Materials*, 21 (2011) 2175-2196.
- [5] Lei, H.; Tang, Y-J.; Wei, J-J.; Li, J.; Li, X-B.; Shi, H-L.; Synthesis of tungsten nanoparticles by sonoelectrochemistry, *Ultrasonic Sonochemistry*, 14 (2007) 81-83.
- [6] Wang, F.; Li, C.; Yu, J.C., Hexagonal tungsten trioxide nanorods as a rapid adsorbent for methylene blue, *Separation and Purification Technology*, 91 (2012) 103-107.
- [7] Pokhrel, S.; Birkenstock, J.; Schowalter, M.; Rosenauer, A.; Mädler, L., Growth of ultrafine single crystalline WO₃ nanoparticles using flame spray pyrolysis, *Crystal Growth Design*, 10 (2009) 632-639.
- [8] Lin, H-C.; Su, C-Y.; Yang, Z-K.; Lin, C-K.; Ou, K-L., A facile route to tungsten oxide nanomaterials with controlled morphology and structure, *Particuology*, 9 (2011) 517-521.
- [9] Hong, S.J.; Jun, H.; Borse, P.H.; Lee, J.S., Size effects of WO₃ nanocrystals for photooxidation of water in particulate suspension and photoelectrochemical film systems, *International Journal of Hydrogen Energy*, 34 (2009) 3234-3242.
- [10] Boulova, M.; Lucazeau, G., Crystallite nanosize effect on the structural transitions of WO₃ studied by raman spectroscopy, *Journal of Solid State Chemistry*, 167 (2002) 425-434.

- [11] Morales, W.; Cason, M.; Aina, O.; de Tacconi, N.R.; Rajeshwar, K., Combustion synthesis and characterization of nanocrystalline WO₃, *Journal of American Chemical Society*, 130 (2008) 6318-6319.
- [12] Huang, R.; Shen, Y.; Zhao, L.; Yan, M., Effect of hydrothermal temperature on structure and photochromic properties of WO₃ powder, *Advanced Powder Technology*, 23 (2012) 211-214.
- [13] Hidayat, D.; Purwanto, A.; Wang, W-N.; Okuyama, K., Preparation of size-controlled tungsten oxide nanoparticles and evaluation of their adsorption performance, *Materials Research Bulletin*, 45 (2010) 165-173.
- [14] Purwanto, A.; Widiyandari, H.; Ogi, T.; Okuyama, K., Role of particle size for platinum-loaded tungsten oxide nanoparticles during dye photodegradation under solar-simulated irradiation, *Catalyst Communications*, 12 (2011) 525-529.
- [15] Nandiyanto, A.B.D.; Okuyama, K., Progress in developing spray-drying methods for the production of controlled morphology particles: From the nanometer to submicrometer size ranges, *Advanced Powder Technology*, 22 (2011) 1-19.
- [16] Wang, W-N.; Widiyastuti, W.; Ogi, T.; Lenggoro, I.W.; Okuyama, K., Correlations between crystallite/particle size and photoluminescence properties of submicrometer phosphors, *Chemistry of Materials*, 19 (2007) 1723-1730.
- [17] Okuyama, K.; Shimada, M.; Adachi, M.; Tohge, N., Preparation of ultrafine superconductive Bi-Ca-Sr-Cu-O particles by metalorganic chemical vapor deposition, *Journal of Aerosol Science*, 24 (1993) 357-366.

Chapter 3

Synthesis of Composite WO₃/TiO₂ Nanoparticles by Flame-Assisted Spray-Pyrolysis and Their Photocatalytic Activity

3.1. Introduction

Most of researches in the photocatalytic field have mainly focused on titanium dioxide (TiO₂) [1]. This material is inexpensive, largely available, chemical and thermal stability, and harmless [2,3]. However, conventional TiO₂ is only active under UV light irradiation [4]. As an alternative of photocatalyst, WO₃ has been proposed as a good candidate [5]. WO₃ is effective because of its narrow band gap properties, making this material is active in the visible solar spectrum [6]. However, WO₃ is scarce, making its use to be affected by rising prices and export restrictions imposed by producer countries.

Efficient photocatalyst materials with good performances are therefore essential in the face of increasing demand but decreasing resources. Recently, combination of the above material candidates has been selected and becoming an interesting subject in the photocatalytic field [7–9]. Beside possibility for the process under visible solar spectrum [6], other advantages gained from the use of this composite are: (1) conduction band of WO₃, when TiO₂ is exist, is suitable to allow transfer of photogenerated electron and charge separation phenomena [10] and (2) combination of these material is able to reduce the total production cost because the price of this composite material is cheaper than that of pure WO₃ material (the price of TiO₂ is cheaper than that of WO₃) [11].

Puddu et al. [12] and Ke et al. [13] reported the synthesis of composite WO₃/TiO₂ nanoparticles using a hydrothermal method. All the mentioned reports succeed to enhance the photocatalytic activity. However, their methods involve time-

consuming, complicated, and multistep processes. Agglomeration condition of the particles produced and control of material size/shape are also not their concern. Akurati et al. [14] synthesized WO₃/TiO₂ nanoparticles by a flame spray-pyrolysis method. Although their method is effective to produce composite TiO₂/WO₃ nanoparticles, their main subject was to investigate relationship between surface acidity and photocatalytic performance only. Further, their process needs complicated process, in which the liquid precursor and solvent are in separate vessels and mixed externally. Using similar method to Akurati et al., Michalow et al. [15] also reported the synthesis of WO₃/TiO₂ nanoparticles. However, their focus is to investigate effect of thermal post-treatment to the prepared particles on crystallite size and photocatalytic activity, and there is no information about particle size and morphology explicitly.

Information about correlations between composition of WO₃ and TiO₂ in the wide range composition value and material properties (i.e. size, morphology, crystallinity, light adsorbent, and photocatalytic activity) are still lacking. Most reports show only the successful synthesis of composite WO₃/TiO₂ nanoparticles. Further, most reports used TiO₂ as a catalytic base material, which in turn employed WO₃ in small amount (less than 10 wt%). Therefore, the explanation in detail about the effect of high concentration of WO₃ in the catalyst properties has not been focused yet. In fact, information about wide range composition of WO₃ and TiO₂ is important for practitioner, in which this composition has a relationship with scaling-up prediction and estimation. Because to the best of our knowledge, there is no report on the investigation on effect of WO₃ and TiO₂ composition on material properties prepared using flame spray pyrolysis, here, the purpose of this study was to investigate effect of amount of WO₃ and TiO₂ in wide range composition on particle morphology (i.e., outer size and shape), crystallinity, light absorbance, and photocatalytic performance in detail.

In our previous studies, we reported several strategies to improve catalytic performance of WO₃ nanoparticles: particle size and morphology, and crystallite size and structure [11,16,17]. However, in our previous reports, we focused on the synthesis of pure WO₃ only and did not report in detail about the influence of additional other semiconductor on the properties of WO₃ catalyst performance yet.

To synthesize composite WO₃/TiO₂ nanoparticles, a flame-assisted spray-pyrolysis method was used. This method is effective to produce agglomeration-free particles and potential for high production rate and one-step process applications. [18,19] We used ammonium metatungstate (AMT, as a WO₃ source) and titanium isopropoxide (TTIP, as a TiO₂ source), which were added directly into ultrasonic nebulizer reactor to produce composite WO₃/TiO₂ nanoparticles. Different from other reports, we did not use either pre-mixing process or particle post treatment; thus, the present synthetic procedure can be said as a one-step process. We selected AMT and TTIP as main raw materials because conversion products of these raw chemicals are free of impurities. Experimental results showed that the particles were free of agglomeration and high crystallinity. We also found that the change in the composition of AMT and TTIP had impacts on catalytic product properties (e.g., particle size (from 20 to 90 nm) and morphology, crystallinity), in which these properties affected on photocatalytic activity. To confirm the fundamental reason for this catalytic improvement, the effect of WO₃ and TiO₂ amounts on surface area, light absorbance, and charge separation analysis was also investigated. In this study, the photocatalytic process was conducted only under visible light condition, whereas the process under UV light irradiation will not be discussed in this study.

3.2 Experimental

3.2.1 Raw chemicals

The composite nanoparticles were produced from a precursor containing AMT ((NH₄)₆(H₂W₁₂O₄₀·xH₂O); Sigma-aldrich Co., USA; purity ≥ 99%) as a WO₃ source, TTIP ((Ti[OCH(CH₃)₂]₄); Kanto Chemical Co. Inc, USA; purity ≥ 97%) as a TiO₂ source, and dimethyl formamide (DMF, N,N-dimethyl formamide; Sigma-aldrich Co., USA; anhydrous 99.8%) as a solvent. To investigate the photocatalytic activity we used amaranth (Wako Pure Chemicals, Japan) as a model of organic pollutant.

3.2.2 Preparation of composite WO₃/TiO₂ nanoparticles

The precursor was prepared by dissolving AMT in 50 mL of DMF. The precursor was then stirred at 400 rpm at a temperature of 40 °C. After 40 min of mixing,

TTIP was added to the precursor and stirred for several minutes. We varied the composition of AMT/TTIP: 0/100; 10/90; 25/75; 55/45; 70/30; and 100/0 wt%.

The precursor was then put into the particle production system. Detailed schematic illustration of the particle production system is shown in **Figure 3.1**. The particle production system consists of an ultrasonic nebulizer (NE-U17, Omron Healthcare Co., Ltd., Tokyo, Japan; operated at 1.7 MHz), a diffusion flame burner, a glass flame reactor, and a bag filter to collect the particles. The precursor was firstly atomized using an ultrasonic nebulizer to generate droplets. The generated droplets were then carried into the diffusion flame burner by a flow of nitrogen gas at 1 L/min. Methane gas was used as the fuel gas at a flow rate of 1 L/min. To maintain a complete combustion reaction, oxygen gas was introduced at a flow rate of 2.5 L/min. In addition, the flow rate of gases was fixed to produce the combustion process with a temperature of around 800 °C.

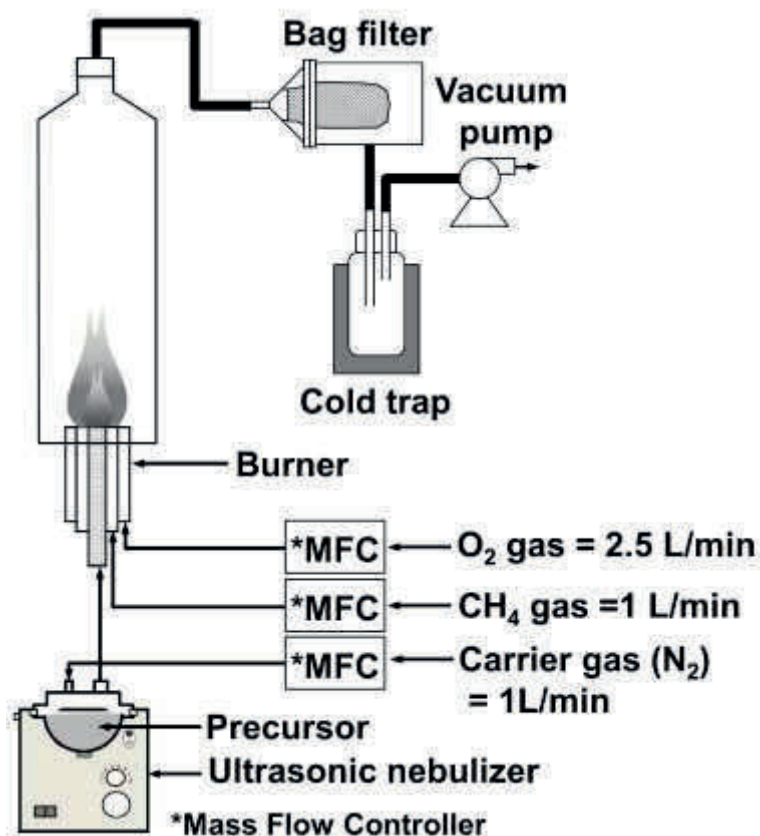


Fig. 3.1. Experimental set up of flame-assisted spray-pyrolysis.

3.2.2 Characterizations

The crystal structure of the prepared particles was determined using an X-ray diffraction analysis (XRD; RINT2000V, Rigaku Denki, Tokyo, Japan; using Cu K α radiation). The morphology and inner structure of the prepared particles were examined using a scanning electron microscope (SEM; Hitachi S-5000, Japan; operated at 20 kV) and a transmission electron microscope (TEM; JEM-3000F, Japan; operated at 300 kV). Elemental mapping of the prepared particles was carried out with a post-column 90° energy filter system (GIF-2000 Gatan Inc., USA). The specific surface area was analyzed using a Brunauer-Emmett-Teller measurement (BET; Bel Japan, BELSORP 28SA, Japan). The absorbance spectra of the prepared particles were measured with a UV-Vis spectrophotometer (UV 2450, Shimadzu, Kyoto, Japan).

To investigate the photocatalytic activity of the prepared particles, the photodecomposition of amaranth under a solar illuminator (PEC-L11, Pecell Technologies, Inc., Japan; AM 1.5G (100 mW/cm²)) was conducted for 1 h. 10 ppm of amaranth was diluted with 100 mg of the prepared particles in 100 mL of ultra-pure water. The solution was stirred at 100 rpm for 2 h in dark conditions to provide saturation conditions for the adsorption of the amaranth-photocatalyst. 200 mL/min of oxygen gas was bubbled into the reactor to maintain the saturation concentration of dissolved oxygen in the solution. A photodegradation sample was taken from the reactor suspension, centrifuged at 15,000 rpm for 5 min, and analyzed using a UV-Vis spectrophotometer (UV2450, Shimadzu; wavelength range of 400 – 700 nm).

3.3 Results and discussion

3.3.1 Synthesis of composite WO₃/TiO₂ nanoparticles

Figure 3.2 shows XRD patterns of the particles prepared using different composition of AMT and TTIP. Diffraction peaks of the monoclinic phase of WO₃ (JCPDS no. 72-1465) and anatase TiO₂ (JCPDS no. 71-1167) were identified for all variations, indicating that the prepared particles contained WO₃ and TiO₂. We found that all samples were in a good crystallinity structure. Neither change in the crystal phase nor structure was found, indicating that changing the composition did not alter the type of conversion of AMT and TTIP into WO₃ and TiO₂, respectively. However, changes in

the ratio resulted in a change in crystal size only. Increases in the AMT amount resulted in an increase in WO_3 crystal size but a decrease in TiO_2 crystal size. Scherrer analysis showed that the crystal size of WO_3 (at 23.1°) and TiO_2 peaks (at 25.3°) changed. When AMT was not added, only TiO_2 with a crystal size of 41 nm appeared. When AMT was added from 25 to 100 wt%, crystal size of WO_3 and TiO_2 were “from 5.4 to 11” and “39 to 31”, respectively. To clarify the effect of mass composition on crystallite size, the results are summarized in **Table 3.1**.

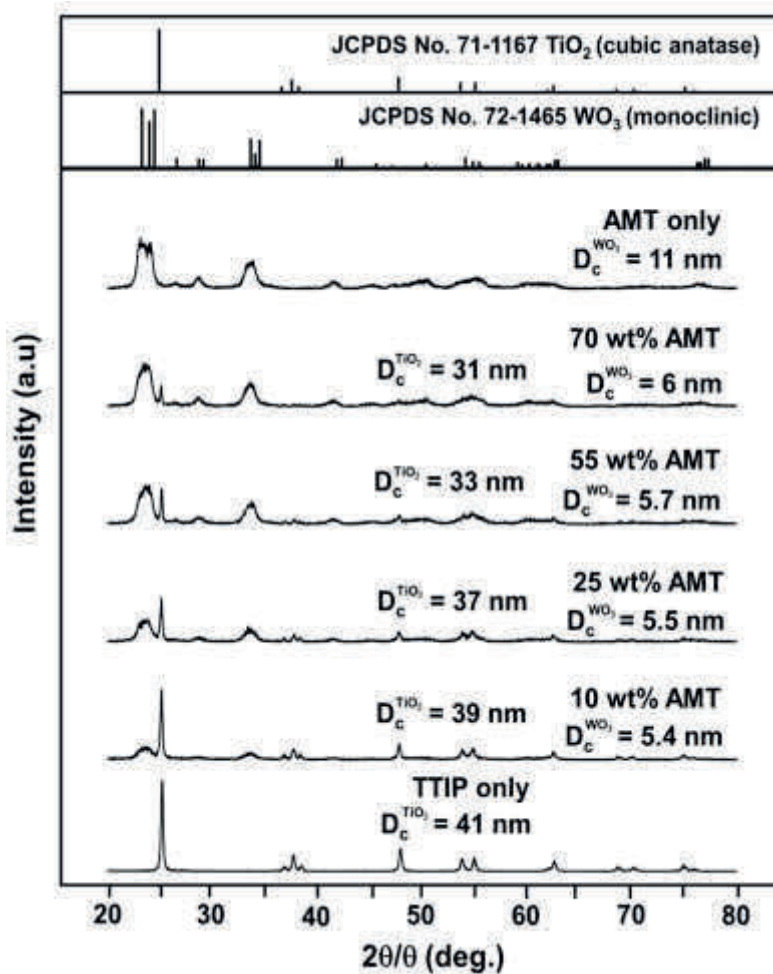


Fig. 3.2. XRD patterns of particles prepared with various compositions of AMT and TTIP.

Figure 3.3 shows SEM images of the particles prepared with various compositions of AMT and TTIP. The prepared particles were not agglomerated in all

variations. When using 0 wt% of AMT, larger particles with a spherical shape were produced (**Figure 3.3(a)**). When the amount of AMT was 10 wt%, smaller particles started to appear in addition to larger particles (**Figure 3.3(b)**). Further increasing the amount of AMT from 25 to 70 wt% resulted in a decrease in the number of large and spherical particles (**Figure 3.3(c)**). The use of 100 wt% AMT resulted in the production of particles of nanometer size and irregular shape (**Figure 3.3(d)**). The results conclude that increases in AMT amount lead to the production of smaller-sized particles.

Table 3.1. Crystallite size of the prepared particles with various concentrations of AMT and TTIP.

| AMT (%wt) | TTIP (%wt) | Crystal size WO ₃ (nm) | Crystal size TiO ₂ (nm) |
|-----------|------------|-----------------------------------|------------------------------------|
| 0 | 100 | - | 41 |
| 10 | 90 | 5.4 | 39 |
| 25 | 75 | 5.5 | 37 |
| 55 | 45 | 5.7 | 33 |
| 70 | 30 | 6 | 31 |
| 100 | 0 | 11 | - |

Figure 3.4 shows the effect of AMT amount on particle size and surface area. Experimental results show that increasing the AMT amount results in the decrease in particle size (dp) (from 89 to 24 nm) but an increase in surface area (S_{BET}) (from 18 to 46 m²g⁻¹). The particle size distributions of the prepared particles are shown in **Figure 3.5**.

Figure 3.6 shows TEM and HRTEM images of the prepared particles at various compositions of AMT/TTIP. **Figure 3.6(a1-d1)** are low-magnified TEM images, whereas **Figure 3.6(a2-d2)** are the high-magnified TEM images. A strong relationship between the concentration of AMT and the morphology of the prepared particles was found. The TEM analysis showed that the prepared particles were dense and free of agglomeration in all cases. These results are in a good agreement with the SEM analysis

shown in **Figure 3.3**. In the high-magnified TEM images, the lattice fringes of 3.6 and 3.8 Å were detected in the prepared particle. These lattice fringes of 3.6 and 3.8 Å are identical to the (101) plane of cubic anatase TiO_2 and the (002) monoclinic WO_3 , respectively. These values correlate well with the XRD patterns in **Figure 3.2**.

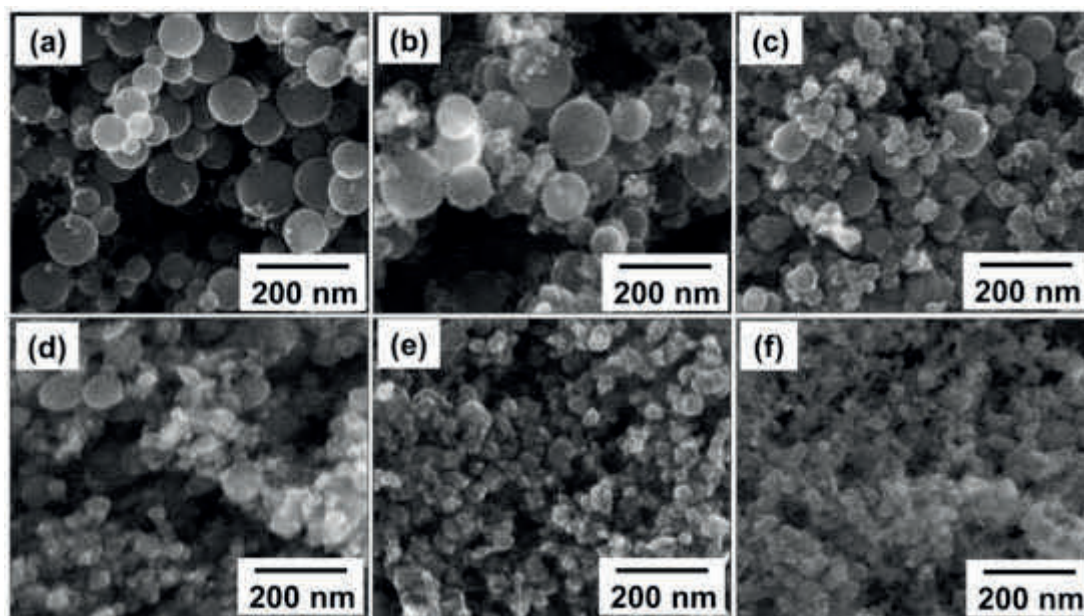


Fig. 3.3. SEM images of particle prepared with various compositions aof AMT and TTIP: (a) 0:100, (b) 10:90, (c) 25:75, (d) 55:45, (e) 70:30, and (f) 100:0 wt%.

Elemental mapping images of the particles prepared with various amounts of AMT are shown in **Table 3.2**. The STEM images show samples containing spherical particles and irregular-shaped nanoparticles. The elemental mapping results show that the prepared particles contained O, W, and Ti. Well-distributed color intensities inside the prepared particles were found, confirming that the prepared particles contained WO_3 and TiO_2 . However, we found that changing the AMT amount led to a change in the different color intensities, indicating that this parameter ratio affected the elemental composition within the particle.

Figure 3.7 shows light absorbance analysis of samples prepared with various amounts of AMT. An increase in AMT amount shifted the light wavelength. By increasing the AMT amount from 0 to 100 wt%, the wavelength of light absorbance

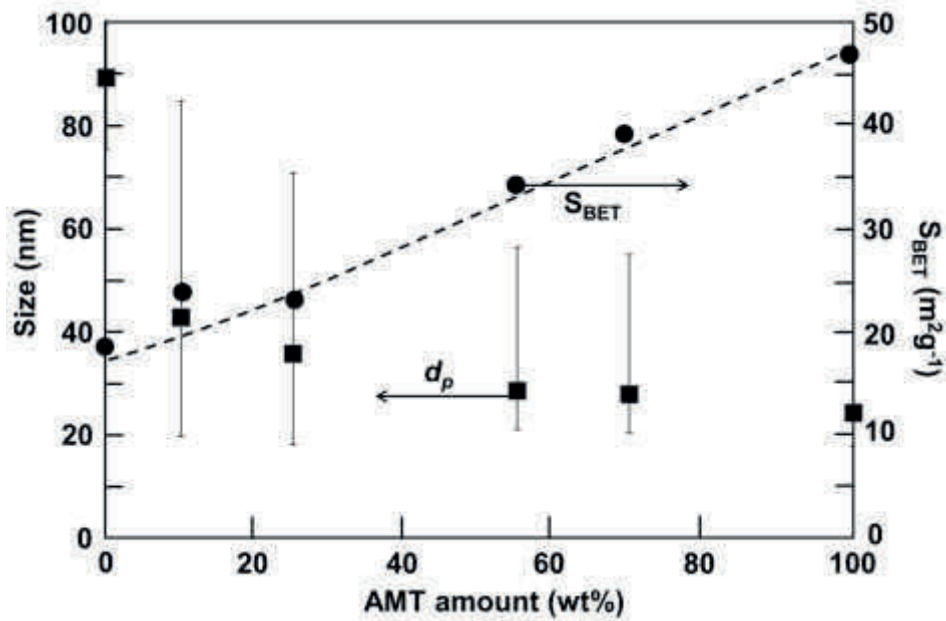


Fig. 3.4. Effect of AMT amount on particle size, and surface area of the prepared particles.

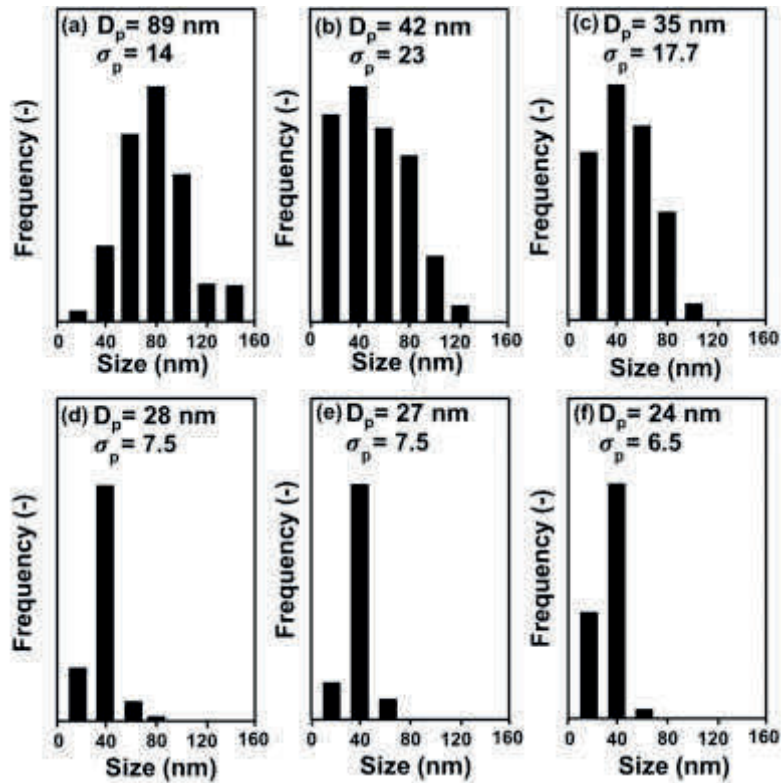


Fig. 3.5. Particle size distribution of nanocomposite prepared with various mass ratio of AMT and TTIP: (a) 0:100, (b) 10:90, (c) 25:75, (d) 55:45, (e) 70:30, and (f) 100:0 wt%.

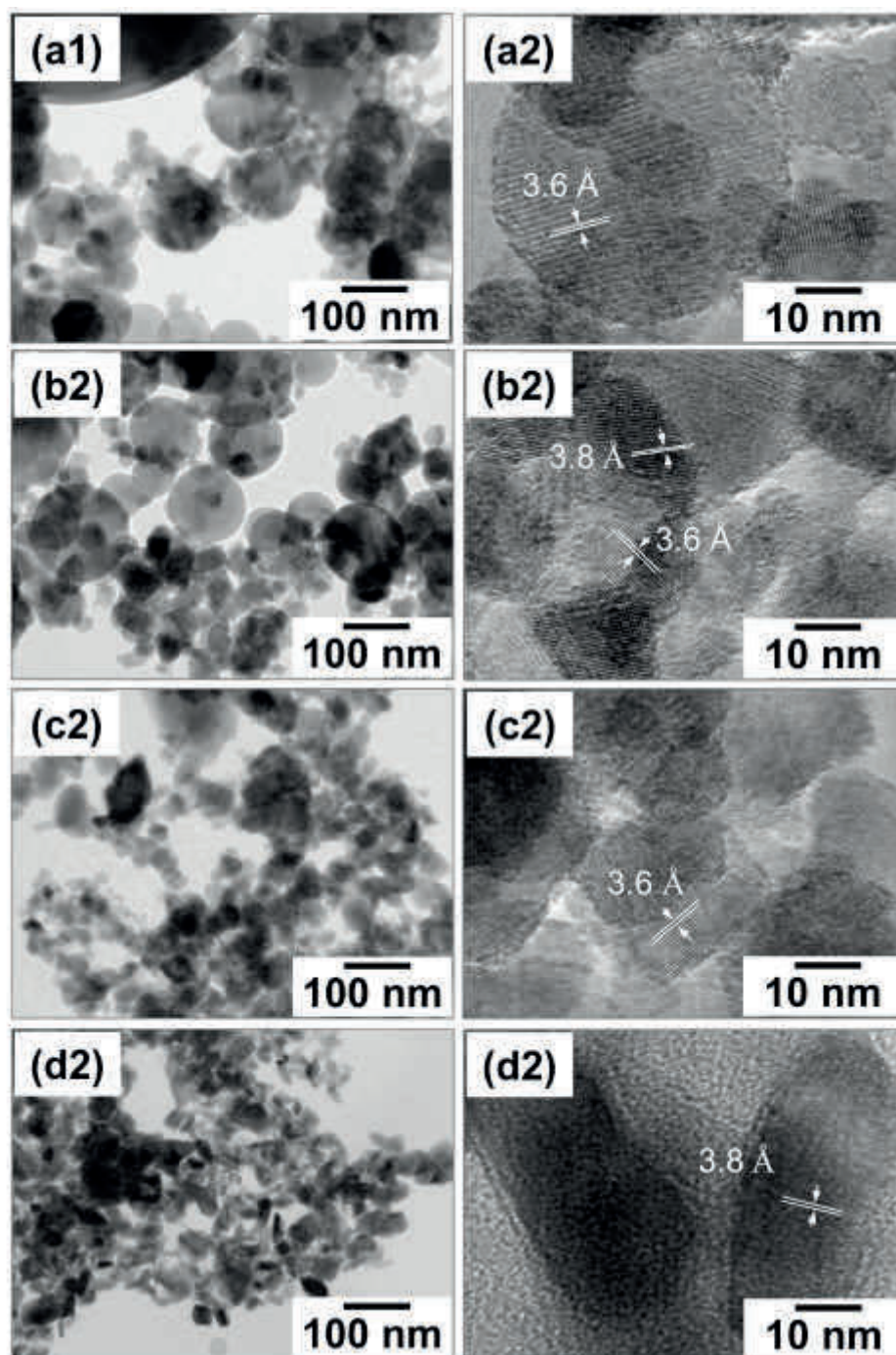
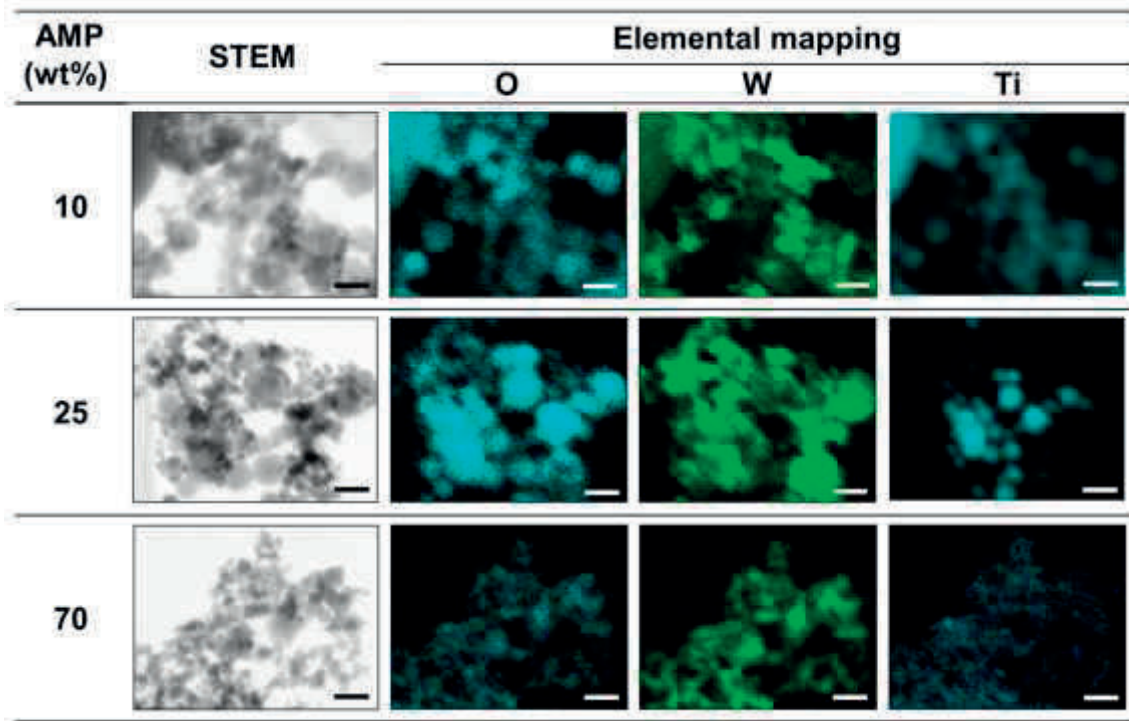


Fig. 3.6. TEM images ((a1),(b1),(c1),(d1)) and HRTEM images ((a2),(b2),(c2),(d2)) of nanocomposite particles prepared with various composition of AMT and TTIP. Sample (a1,a2), (b1,b2),(c1,c2), and (d1,d2) were prepared using AMT and TTIP (wt%): 10:90; 25:75; 70:30; and 100:0, respectively.

Table 3.2. STEM and elemental mapping images of particles prepared with various amounts of AMT. Scale bars are 100 nm.



shifted from 371 to 416 nm, respectively. This indicates a change in wavelength from blue to red.

The change in wavelength can be correlated to a change in the band gap of the prepared particles. The evaluation band gap can be determined, as follows[20, 21]

$$E = (hc)/\lambda \quad (3.1)$$

where E is the band gap energy (eV), h is the Planck's constant of 6.62×10^{-34} (J·sec), C is the speed of light (3×10^8 m/s), and λ is the cut off wavelength (nm). Using Eq. 1, the band gap energy of the prepared particles were found to be 3.35; 3.33; 3.16; 3.00; and 2.98 eV, corresponding to AMT amount of 0; 10; 25; 70; and 100 wt%, respectively.

3.3.2 Evaluation of the photocatalytic activity of the prepared composite particles

Figure 3.8 shows the photodegradation profiles of 10 ppm of amaranth with the additional of the prepared particles (as a catalyst) using a solar simulator. No amaranth degradation was found in the absence of a catalyst (shown in dashed line), while the

additional of a catalyst to the solution caused a change in the amaranth concentration (shown by the solid lines). The concentration of amaranth gradually decreased over time. The photodegradation ability of the catalyst prepared with 0 wt% of AMT was the worst (remaining amaranth of about 97 %). Increases in the AMT amount from 10 to 100 wt% for the synthesis of the catalyst resulted in an improvement in photocatalytic activity, and the final concentration of amaranth decreased from 90 to 74 %, respectively.

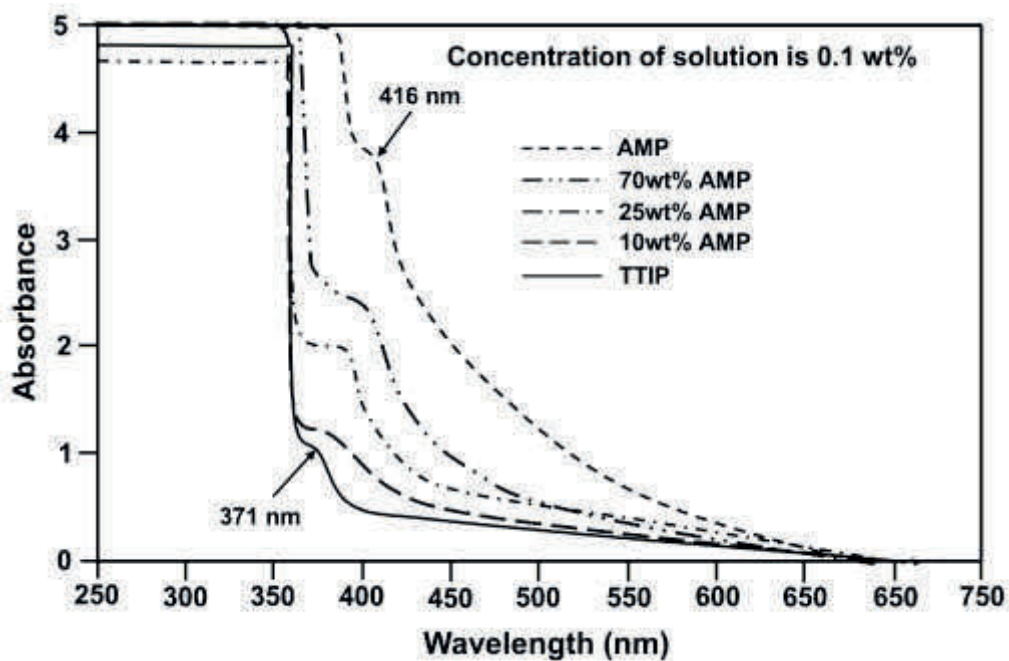


Fig. 3.7. UV-Vis absorbance spectra of the particles prepared with various compositions AMT and TTIP.

Figure 3.9 shows a detailed correlation among the surface area (S_{BET}), the band gap (E_g), and the photodecomposition rates (k) of the prepared particles as the effect of the AMT amount. To simplify the calculation of photodecomposition rates, Langmuir-Hinshelwood theory was used. We found that the increases in AMT amount affected the increases in surface area and photodecomposition rates, and the decrease in band gap energy.

To clarify the effect of AMT amount, we classified the results into two categories. The first category is when the AMT amount is less than 25 wt%, whereas the second category is when the AMT amount is more than 25 wt%.

In the first category, the k value increases drastically, while the S_{BET} values slightly increase. This result confirms that increases in photocatalytic are significantly as same as the decreases in band gap value. The E_g value from **Figure 3.7** changes from 3.35 to 3.16 eV with a change in AMT amount from 0 to 25 wt%, respectively. This result shows that the change of E_g is quite different and the deviation ratio for (band gap)/(AMT) is (0.19 eV)/(25 wt%).

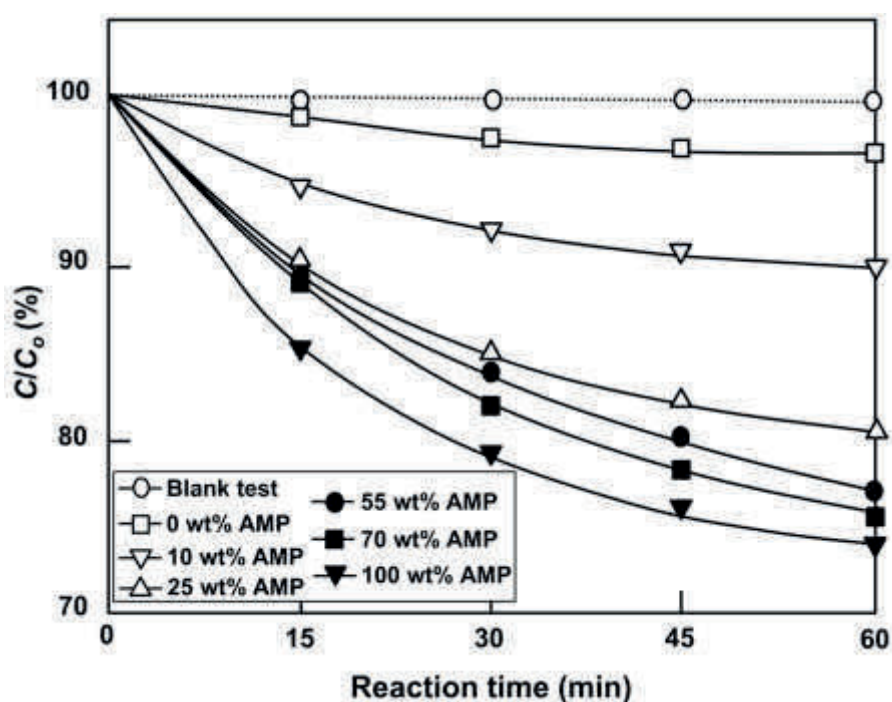


Fig. 3.8. Photodegradation profiles of 10 ppm amaranth with various amounts of AMT.

C and C_0 are the concentration of amaranth at the initial and measured times, respectively.

Different with the first category, in the second category the S_{BET} values are directly proportional with the AMT amount. However, the increase in photocatalytic activity is not significant much than that in the first category. From the **Figure 3.7**, the

band gap value changes from 3.16 to 2.98 eV. The deviation ratio of (band gap)/(AMT) is (0.18 eV)/(75 wt%).

From both categories, the change of photocatalytic activity is mainly influenced by band gap energy. However, beside the presence of band gap, the surface area are also plays an important role, where increases in the surface area allow the improvement of photocatalytic performance. This effect if surface area under the same crystallinity are confirmed and discussed in detail in our previous works [11,17].

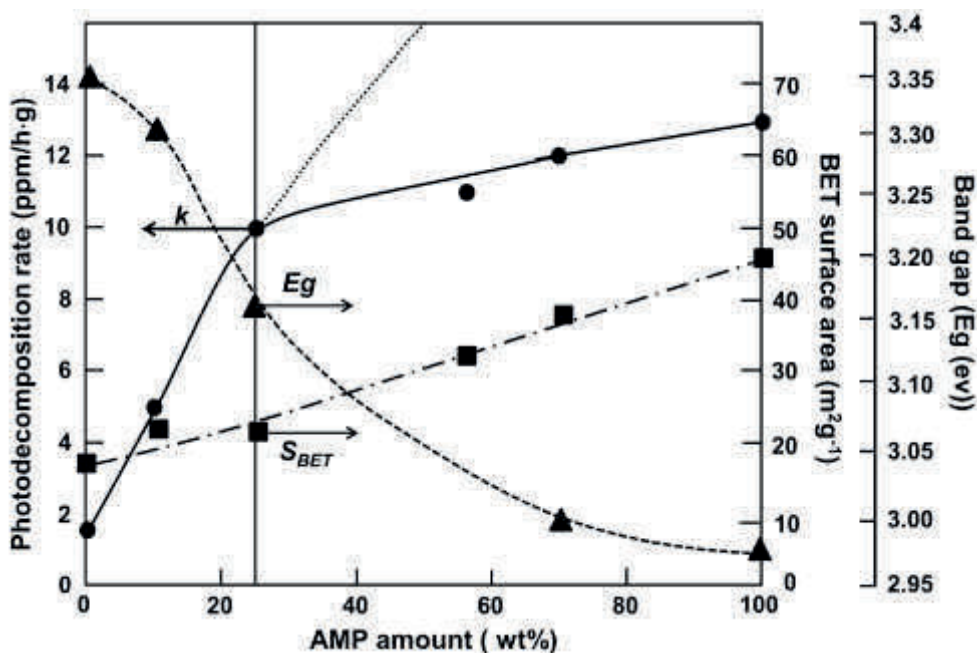


Fig.3.9. The effect of AMT amount in the physical chemical properties of particles.

Experimental results for pure TiO_2 (0 wt% of AMT) and pure WO_3 (100 wt% of AMT) are in a good agreement with theoretical analysis. The band gap of WO_3 is narrower than that of TiO_2 , resulting in photodegradation ability of WO_3 being better than that of TiO_2 under visible light. However, when WO_3 and TiO_2 are combined, no linear correlation between AMT amount and the k line (solid line in **Figure 3.9**) is apparent. This is because of an interesting phenomenon relating to the recombination of electrons and holes in the composite material.

To verify the above-mentioned recombination of electrons and holes phenomenon, we propose a mechanism for the couple-system, as shown in **Figure 3.10**.

In the photocatalytic system, the catalyst will be activated by an appropriate amount of energy. In the single system (WO_3 or TiO_2 only), when the catalyst is illuminated by photons (**Route R_1**), pairs of holes (h^+) in the valence band (VB), and electrons (e^-) in the conduction band (CB) are created (**Route R_2**). WO_3 has a band gap of around 2.92 eV (**Route R_{21}**) and can be activated by visible light, whereas TiO_2 with a band gap of 3.35 eV is more effective at absorbing UV light (**Route R_{22}**). Therefore, the amount of electrons that are produced in the WO_3 system is greater than that for the TiO_2 system because it absorbs more photons.

When the catalyst contains two material systems (i.e., WO_3 and TiO_2), a change occurs in the photocatalytic mechanism route (i.e., **Route R_3** and **Route R_4**). In this system, both the upper edge of VB- WO_3 and the lower edge of CB- WO_3 are lower than those of TiO_2 [22]. Illumination by photons causes the h^+ in VB- WO_3 to move to VB- TiO_2 (**Route R_3**), and also the e^- from CB- TiO_2 to moves to CB- WO_3 . This condition prevents recombination of e^- and h^+ , causing unique phenomenon (known as charge separation). This charge separation enhances the production of OH radicals, which is effective for increasing the photocatalytic performance.

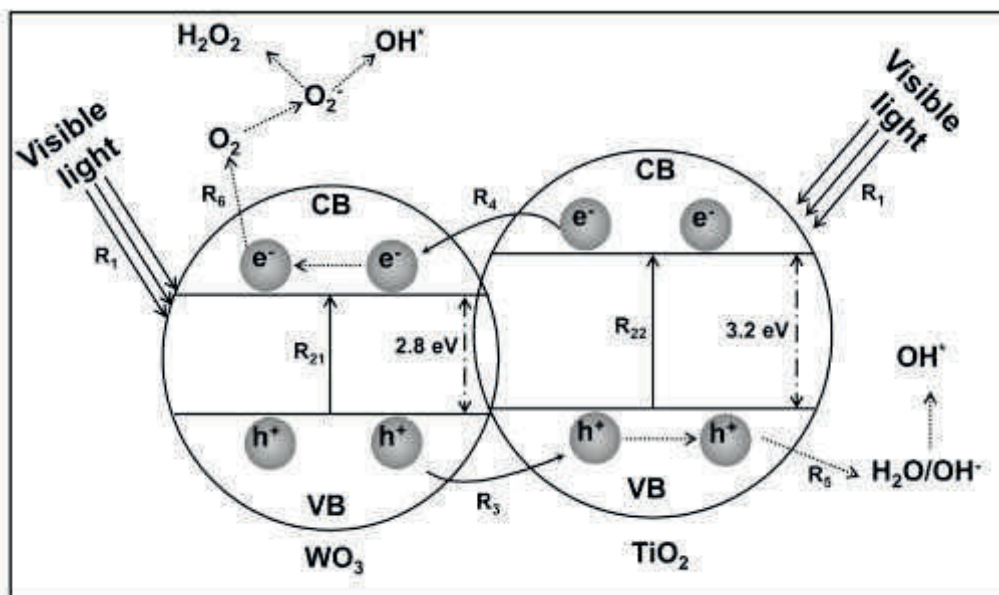


Fig. 3.10. The proposal photocatalytic mechanism of particle containing WO_3 and TiO_2 .

The relation between this model in **Figure 3.10** and result in **Figure 3.9** can be described in the following. When the presence of WO₃ within the normal limits (AMT is less than 25 wt%), the amount of electron in VB-WO₃ that react with O₂ will be greater than the amount participating in the recombination process. As a consequence, better photocatalytic performance than pure TiO₂ catalyst can be gained. These results explain the drastically improvement in the photodecomposition rates when using AMT of less than 25 wt%. However, when the concentration of AMT is more than 25 wt%, more electrons will be accumulated in VB-WO₃, causing recombination and thus decreasing the photocatalytic activity. Since the speed of recombination between e⁻ and h⁺ in the WO₃ system is faster than the speed of the reaction between e⁻ and O₂ [14], the photocatalytic performance will be decreased. Although there is some improvement in the photocatalytic activity, the improvement is due to the influence of surface area in the chemical-to-catalyst interaction.

3.4 Conclusion

Composite WO₃/TiO₂ nanoparticles were successfully prepared by the flame-assisted spray-pyrolysis. The effect of amount of WO₃ and TiO₂ in wide range composition (0-100 wt%) on particle morphology (i.e., outer size and shape), crystallinity, light absorbance, and photocatalytic performance was investigated in detail. Experimental result showed that the photocatalytic performance of the composite WO₃/TiO₂ nanoparticles was higher than that of the catalyst containing 100 wt% of TiO₂. The improvement of photocatalytic activity is mainly influenced by band gap energy. However, beside the presence of band gap, the surface area also plays an important role in the change of photocatalytic activity. Although our present photocatalytic activity is still low, the information about the effect of WO₃ and TiO₂ composition in the catalyst open new information for creating more varied properties for application explorations.

3.5 References

- [1] Chen, X.; Mao, S.S., Titanium dioxide nanomaterials: synthesis, properties, modifications, and applications, *Chemical Review*, 107 (2007) 2891-2959.

- [2] Daghrrir, R.; Drogui, P.; Robert, D., Modified TiO₂ for environmental photocatalytic applications: A Review, *Industrial & Engineering Chemistry Research*, 52 (2013) 3581-3599.
- [3] Bhatkhande, D.S.; Pangarkar, V.G.; Beenackers, A.A., Photocatalytic degradation for environmental applications—a review, *Journal of Chemical Technology and Biotechnology*, 77 (2002) 102-116.
- [4] Yang, H.; Shi, R.; Zhang, K.; Hu, Y.; Tang, A.; Li, X., Synthesis of WO₃/TiO₂ nanocomposites via sol-gel method, *Journal of Alloys and Compounds*, 398 (2005) 200-202.
- [5] Bertus, L.; Faure, C.; Danine, A.; Labrugère, C.; Campet, G.; Rougier, A.; Duta, A., Synthesis and characterization of WO₃ thin films by surfactant assisted spray pyrolysis for electrochromic applications, *Materials Chemistry and Physics*, 140 (2013) 49-59.
- [6] Zheng, H.; Ou, J.Z.; Strano, M.S.; Kaner, R.B.; Mitchell, A.; Kalantar-zadeh, K., Nanostructured tungsten oxide-properties, synthesis, and applications, *Advanced Functional Materials*, 21 (2011) 2175-2196.
- [7] Papp, J.; Soled, S.; Dwight, K.; Wold, A., Surface acidity and photocatalytic activity of TiO₂, WO₃/TiO₂, and MoO₃/TiO₂ photocatalysts, *Chemistry of Materials*, 6 (1994) 496-500.
- [8] Kwon, T.; Song, Y.; Lee, I.; Choi, J.; Rag, D.Y., Photocatalytic behavior of WO₃-loaded TiO₂ in an oxidation reaction, *Journal of Catalysis*, 191 (2000) 192-199.
- [9] Xiao, M.; Wang, L.; Huang, X.; Wu, Y.; Dang, Z.; Synthesis and characterization of WO₃/titanate nanotubes nanocomposite with enhanced photocatalytic properties, *Journal of Alloys and Compounds*, 470 (2009) 486-491.
- [10] He, T.; Ma, Y.; Cao, Y.; Hu, X.; Liu, H.; Zhang, G.; Yang, W.; Yao, J.; Photochromism of WO₃ colloids combined with TiO₂ nanoparticles, *Journal of Physical Chemistry B*, 106 (2002) 12670-12676.
- [11] Nandiyanto, A.B. D.; Arutanti, O.; Ogi, T.; Iskandar, F.; Kim, T.O.; Okuyama, K. Synthesis of spherical macroporous WO₃ particles and their high photocatalytic performance, *Chemical Engineering Science*, 101 (2013) 523-532.

- [12] Puddu, V.R.; Mokaya,; Puma, G.L., novel one step hydrothermal synthesis of TiO₂/WO₃ nanocomposites with enhanced photocatalytic activity, *Chemical Communications* (2007) 4749-4751.
- [13] Ke, D.; Liu, H.; Peng, T.; Liu, X.; Dai, K., Preparation and photocatalytic activity of WO₃/TiO₂ nanocomposite particles, *Materials Letters*, 62 (2008) 447-450.
- [14] Akurati, K.K.; Vital, A.; Dellemann, J.-P.; Michalow, K.; Graule, T.; Ferri, D.; Baiker, A., Flame-made WO₃/TiO₂ nanoparticles: Relation between surface acidity, structure and photocatalytic activity, *Applied Catalysis B: Environmental*, 79 (2008) 53-62.
- [15] Michalow, K.A.; Heel, A.; Vital, A.; Amberg, M.; Fortunato, G.; Kowalski, K.; Graule, T.J.; Rekas, M., Effect of thermal treatment on the photocatalytic activity in visible light of TiO₂-W flame spray synthesised nanopowders, *Topics Catalysis*, 52 (2009) 1051-1059.
- [16] Hidayat, D.; Purwanto, A.; Wang, W.-N.; Okuyama, K.; Preparation of size-controlled tungsten oxide nanoparticles and evaluation of their adsorption performance, *Material Research Bulletin*, 45 (2010) 165-173.
- [17] Arutanti, O.; Ogi, T.; Nandiyanto, A.B.D.; Iskandar, F.; Okuyama, K., Controllable crystallite and particle sizes of WO₃ particles prepared by a spray - pyrolysis method and their photocatalytic activity, *AIChE Journal*, 60 (2013) 41-49.
- [18] Strobel, R.; Baiker, A.; Pratsinis, S.E., Aerosol flame synthesis of catalysts, *Advanced Powder Technology*, 17 (2006) 457-480.
- [19] Widiyastuti, W.; Purwanto, A.; Wang, W.N.; Iskandar, F.; Setyawan, H.; Okuyama, K., Nanoparticle formation solid-fed flame synthesis: Experiment and modeling, *AIChE Journal*, 55 (2009) 885-895.
- [20] Dharma, J.; Pisal, A.; Shelton, C., Simple Method of Measuring the Band Gap Energy Value of TiO₂ in the Powder Form using a UV/Vis/NIR Spectrometer, *Application Note*, (2009).
- [21] Luo, X.-B.; Deng, F.; Min, L.; Luo, S.-L.; Guo, B.; Zeng, G.; Au, C., Facile one-step synthesis of inorganic-framework molecularly imprinted TiO₂/WO₃ nanocomposite and its molecular recognitive photocatalytic degradation of target contaminant, *Environmental Science and Technology*, 47 (2013) 7404-7412.

- [22] Srinivasan, A.; Miyauchi, M.; Chemically stable WO₃ based thin-film for visible-light induced oxidation and superhydrophilicity, *Journal of Physical Chemistry C*, 116 (2012) 15421-15426.

Chapter 4

Synthesis of Spherical Macroporous WO₃ Particles and Their High Photocatalytic Performance

4.1. Introduction

Recently, tungsten trioxide (WO₃) has been widely studied because it has an affinity for visible light, and is chemically inert, thermally stable, and harmless [1-3]. These excellent properties make this material useful for solar-related applications such as photocatalysts, solar cells, water splitting, and hydrogen generation. However, there are several problems regarding the use of this material, particularly with regard to its availability. The material is scarce, and its use is affected by rising prices and export restrictions imposed by producer countries. Efficient materials with good performances are therefore essential in the face of increasing demand but decreasing resources [4].

To solve the above problems, design of materials in the nanometer-sized ranges is the best. However, the use of this type of material remains problems. The application of nanoparticles is known to have greater adverse health effects than larger particles because of the possibility for them to be deposited into the alveoli and potentially be absorbed through the skin. Further, when the nanoparticles are disposed of directly, there are environmental problems to overcome. Therefore, specific processes for separating these nanomaterials (after nanoparticles are not used any longer) are crucial although the separation process is typically expensive. These difficulties and costs in the separation process are not found when using larger particles [5].

Design of materials with porous structures has been much studied to solve this difficulty. An increase in the porous structural order improves the material performance and also reduces the amounts of raw materials used [5]. However, there is little information on porous WO₃ in the literature. Until recently, there were only few papers on porous WO₃. Baeck *et al.*, [6] Teoh *et al.*, [7] and Li *et al.* [8] used surfactants as

templates, and materials with mesoporous structures were successfully prepared. However, the surfactant sometimes cannot be removed completely,[9] which may produce impurities and adversely affect the material performance. Instead of surfactants, Singh *et al.*[10] and Chen *et al.*[11] proposed the use of gas bubbles to form pores. Although such methods are effective, the synthetic procedures are complicated and require the use of electrochemical devices, limiting scaling-up of production. Huang *et al.*[9] suggested controlling particle growth to produce micro-flower particles. Control of the particle morphology has been reported, but the use of sodium tungsten can create problems, and additional purification processes are needed to remove sodium from the final product. In addition, the above methods result in the formation of mesoporous structures, which are not applicable to the photodecomposition of large molecules because of limitations in mass transfer, diffusivity, and penetration of molecules and photons into or out of the mesoporous system [12].

To develop materials with pores larger than those in the mesoporous range, Sadakane *et al.*,[13] Sumida *et al.*,[14] and Chen *et al.*[15] proposed the use of submicron polymer spheres as templates. Macropores with spherical pore shapes were obtained. However, the process has limitations as it can only be used to produce films. Lv *et al.*[16] further developed the process by using carbon spheres as the template. Porous particles were successfully produced, but because carbon could damage the catalytic performance, carbon removal is of particular concern. Leghari *et al.*[17] and Amano *et al.*[18] suggested using hydrothermal processes instead of templating methods. Although hydrothermal processes successfully create macroporous structures under template-free condition, these processes have limitations such as formation of pores with irregular sizes and structures, and difficulties in producing monodispersed particles.

Most reports show that the above methods have been successfully used to prepare porous WO_3 , but the physical appearance of the product (i.e., roughness, porosity, agglomeration, and irregular shape of the prepared particles) and the mechanism of porous particle formation have not been considered. Also, these methods have the disadvantages of high costs, time-consuming processes, low throughput, and unsuitability for large-scale production. Furthermore, correlations between porous

structure and material performance have not yet been discussed, while such information is crucial for optimizing the performances of porous particles.

In our previous works, we reported the synthesis of porous particles with controllable pore size and particle outer diameter using liquid-phase synthesis [12] and spray methods [12,19,21-23]. Optimization of the process parameters (i.e., surface charge, size, and concentration of colloidal nanoparticles) was also investigated in detail to get highly ordered porous film and particles [22]. With this optimization, control of particle morphology, porous structure, pore size, particle outer diameter are possible. This optimization is then used for developing the synthesis of particles from the smallest engineered porous silica nanoparticles [12] to micrometer-sized particles [21,22].

Based on our previous works, the purpose of this study was to develop a method for the rapid synthesis of spherical macroporous WO₃ particles with controllable porous structure and particle diameter (from 0.3 to 2 μm) and to examine the correlations between the porous structure and the photocatalytic performance over non-porous WO₃ particles. We limited our synthesis method in preparing particles with few hundred nanometers of pores with the prospect of reducing diffusion limitation of molecules with larger size and high concentration. In general, the use of these types of pores can be possible for applications in molecules with variation of sizes and concentrations. The spherical macroporous WO₃ particles were prepared by a spray-pyrolysis of a precursor suspension containing ammonium tungsten pentahydrate (ATP) as a tungsten source and polystyrene (PS) spheres as a colloidal template. Unlike other methods that involve complicated and time-consuming processes, the present method enables one-step production of macroporous WO₃ particles with a residence time of several seconds, which is promising for industrial applications. Several process parameters (i.e. initial precursor concentration and mass ratio between host and template) were investigated to get highly ordered porous particles. In addition, although the processing time is a crucial factor in the particle formation in the spray method (i.e. providing conversion of raw material, giving more time for solvent evaporation, and offering self-assembly of components into their maximum structure), we did not focus on this parameter in the

present paper because this parameter has been discussed in detail in our previous work [19].

Experimental results showed that the porous structure and particle diameter were controllable only by varying the PS/ATP mass ratio and the initial precursor concentration, respectively; while most previous WO₃ papers have not dealt with these good porous structure and outer diameter control. Due to the advantage of the template method [5,22], the present method also allows the production of particles with spherical macropores. A detailed investigation was performed to determine the optimum amount of PS needed to obtain maximum photocatalytic performance, and the photocatalytic rate was compared with that of non-porous WO₃ particles. As a result of the macroporous structure, the number of catalytic active site increases, resulting the particles with macroporous structure to have better performance than those with dense structure. A mechanism for porous WO₃ particle formation is also proposed; where this has not been covered in previous reports.

4.2 Experimental

4.2.1 Raw materials

Macroporous WO₃ particles were prepared from a precursor containing ATP (Kanto Chemical Co., Inc., Japan) and 230-nm additive-free cationic PS spheres in the aqueous solution. The PS spheres were synthesized from a simple polymerization of styrene monomer (styrene; Kanto Chemical Co., Inc., Japan) under surfactant-free conditions. 2,2-azobis (isobutyramidine) dihydrochloride (AIBA; Sigma-Aldrich, US) was used as an initiator in the styrene polymerization to produce PS spheres. A detailed synthetic method of additive-free PS spheres has been previously reported. (Nandiyanto *et al.*, 2012) To produce PS spheres with a mean diameter of 230 nm, we used styrene of 2.00 wt% and AIBA of 0.04 wt%, which was processed at temperature of 75°C. All chemicals were used without further purification.

4.2.2. Preparation of Macroporous WO₃ Particles.

The precursor was sonicated for several minutes at room temperature to ensure that both ATP and PS spheres were well-dispersed in the suspension. To investigate the

effect of PS/ATP mass ratio on the porous structurization, various mass ratios of PS/ATP from 0.00 to 0.64 were used. To investigate the effect of precursor concentration, we used a precursor with concentration from 10 to 100 g/L.

The sonicated precursor was then placed in an ultrasonic nebulizer (Omron Corp. model NE-U12, operated at a frequency of 1.7 MHz), which was used to generate monodispersed droplets of several micrometers in diameter. The generated droplets were then introduced into a ceramic tubular furnace ($D = 30$ mm and $L = 1.30$ m; two fixed-temperature zones: 200 and 700°C) using a carrier gas (air; a flow rate of 5 L/min). The prepared particles were then collected using a filter. The detailed experimental apparatus is shown in our previous papers [5,12,20].

4.2.3 Characterization.

The prepared particles were characterized using a scanning electron microscopy (SEM; Hitachi S-5000, operated at 20 kV) and a transmission electron microscopy (TEM; JEM-3000F, JEOL, operated at 300 kV) to examine the size, morphology, and structure of the prepared particles. The crystallinity of the particles was examined using an X-ray diffraction (XRD; Rigaku Denki RINT2000, with Cu $K\alpha$ radiation; angular domain 20–80° (2θ)). To observe the specific surface area of the prepared particles, Brunauer–Emmett–Teller measurements (BET; BELSORP 28SA, Bel Japan, nitrogen adsorption isotherms at 77.15 K) were performed. Samples were also characterized using a thermogravimetric analysis (TGA; TGA-60, Shimadzu, Japan; heating rate = 5 °C/min; carrier gas: He, 40 mL/min; reaction gas: air, 30 mL/min).

To investigate the effect of particle pore structure on the material performance, the photodegradation of 2.00 mg/L of rhodamine B (RhB; Wako Pure Chemical Industries Ltd., Japan) by the prepared particles (0.40 g/L) under visible-light irradiation was examined. The photodegradation was performed in a photoreactor system equipped with a solar simulator (PEC-L11, Peccell Technologies Inc., Japan, simulated sunlight conditions, AM 1.5G (100 mW/cm²)). The process was conducted under continuous agitation (400 rpm; magnetic stirrer) at 25°C. To keep the concentration of dissolved oxygen in the solution constant during the experiments, air was bubbled into the reactor at a flow rate of 0.20 L/min. Before beginning the photodegradation reaction, the

suspension was left in the dark for 30 min to establish equilibrium (adsorption/desorption) between the RhB and the prepared WO₃ particles. The RhB concentration in the first sample after dark conditioning was taken as the initial concentration (C_0 ; $t = 0$ min). For measuring the degradation of RhB in the solution, samples were taken from the reactor (actual concentration, C) at sampling time t , and analyzed using a UV-Vis spectrophotometer (UV-3150, Shimadzu, Japan). Photodegradation was monitored for 60 minutes, which was sufficient time to observe the effect of the porous structure on the photodegradation of RhB.

4.3 Results and discussions

4.3.1 Investigation of Physicochemical Properties of Raw Materials and Prepared Particles

The TGA results for a sample containing PS and ATP in a PS/ATP mass ratio of 0.60 is shown in **Figure 4.1**. As comparisons, two reference samples were analyzed: ATP only and PS only. The TGA results showed that loss of mass occurred with increasing temperature. The mass loss below 220°C was the result of loss of physically adsorbed solvent in the sample. After reaching 220°C, a large mass loss was detected for PS/ATP; this was the result of two factors: (i) conversion of ATP (in the range from 220 to 300°C) and (ii) decomposition of PS (in the range from 270 to 410°C). Finally, at temperatures above 420°C, the weight was relatively stable.

Figure 4.2 shows the nitrogen sorption properties of the spray-pyrolyzed particles with and without additional PS. The nitrogen sorption analysis showed that the sample prepared with PS exhibited a characteristic type-II isotherm, whereas the isotherm of the sample without PS was relatively constant (**Figure 4.2a**). The maximum volume adsorption for the sample without PS was negligible (about 8 cm³/g) compared with that for the sample with PS (about 150 cm³/g). The Barrett–Joyner–Halenda (BJH) results show differences between the curve distributions of the samples (**Figure 4.2b**). The curve distribution for the sample without PS was relatively constant, with no pore detection, whereas that of the sample containing PS had a peak at about 150 nm. Since the added PS had a size of more than 150 nm, the appearance of this peak was the result of inverse replication of the PS.

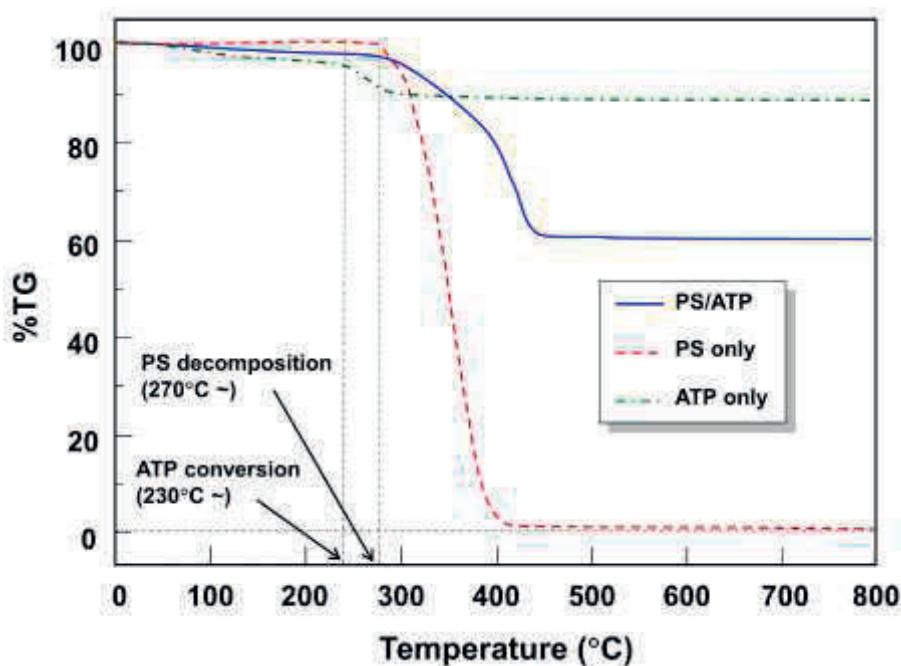


Fig. 4.1. TGA results for PS/ATP, PS only, and ATP only.

Based on the above TG-DTA (Figure 4.1) and surface area analysis results (Figure 4.2), a proposed process is shown schematically in Figure 4.3. Four steps occur during spray-pyrolysis: (i) a self-assembly process, which involves three processes, i.e., solvent evaporation, colloidal transportation, and self-assembly crystallization (this step produces a composite PS/ATP material); (ii) ATP decomposition and component restructuring, which results in formation of a composite PS/WO₃ amorphous material; (iii) PS removal, in which PS is released from the composite, with retention of the porous structure in the WO₃ amorphous particles; and (iv) WO₃ phase transition from amorphous to crystalline. All the processes were completed within several seconds.

4.3.2. Effect of PS/ATP Mass Ratio on Porous Structure inside WO₃ Particles.

XRD patterns of the spray-pyrolyzed particles prepared from precursors with various PS/ATP mass ratios are shown in Figure 4.4. The XRD patterns show that all the synthesized particles are WO₃. The precursor without PS leads to production of monoclinic particles, whereas those with PS give particles with tetragonal and monoclinic phases. When PS is present in the precursor, the PS spheres absorb heat for evaporation. There are therefore heat-transfer changes in the droplets, modifying the

usual conversion of ATP to WO₃. This phenomenon will be investigated in detail in our next work. The Scherrer crystal sizes of the samples at the monoclinic peak of 23° are 28, 25, 25, 25, 23, and 28 nm, corresponding to PS/ATP ratios of 0.00, 0.13, 0.27, 0.40, 0.54, and 0.60, respectively. These results imply that increasing the amount of PS does not change crystal size.

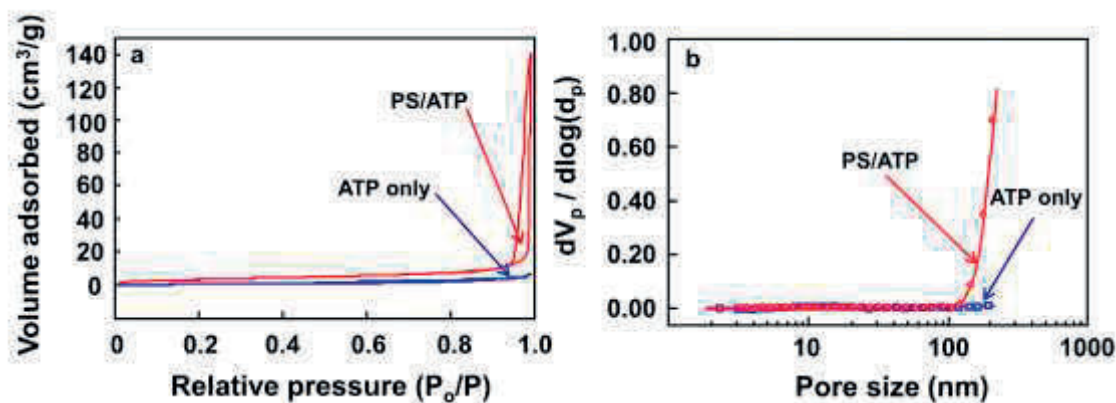


Fig. 4.2. Nitrogen adsorption analysis of prepared particles (a) and pore size distribution analysis using the BJH method (b).

SEM images of the particles produced using various PS/ATP mass ratios are shown in **Figure 4.5**. Spherical particles were obtained in all cases. The spray-pyrolyzed particles produced without PS were non-porous and spherical (**Figure 4.5a**). The addition of PS to the initial precursor solution resulted in the production of porous particles (**Figure 4.5b–f**). However, excess PS created some broken particles (non-spherical shapes with fragmented structures; **Figure 4.5g**). The shapes of the pores are the same with those of initial PS, and the pore numbers depend on the amount of PS, indicating that the fundamental reason for formation of the porous structure is the presence of PS in the initial mixed solution. These mass ratio results were in a good agreement with our hypothesis in our previous work.[22] To examine the porous structures inside the particles, TEM images of the particles prepared with various PS/ATP mass ratios were obtained; they are shown in **Table 1**. The relationship between the mass ratio of PS/ATP and evolution of the porous structure was determined. To describe the process of pore structure formation, the suggested PS arrangement in

the particles is also shown in the table. When the precursor without PS was used, solid particles were produced (Sample A). However, when PS was added to the precursor, pores were detected in the particles (Samples B–D). The shapes and sizes of the pores were identical. The pore number was directly proportional to the amount of PS. However, the TEM results for Samples B–D show inhomogeneous pore distributions in the particles. Most of the pores were on the outside of the particles, whereas there were some PS-unoccupied areas inside the particles (shown by red arrows in the figures in Table 4.1). These TEM results clarified the finding from the SEM images shown in

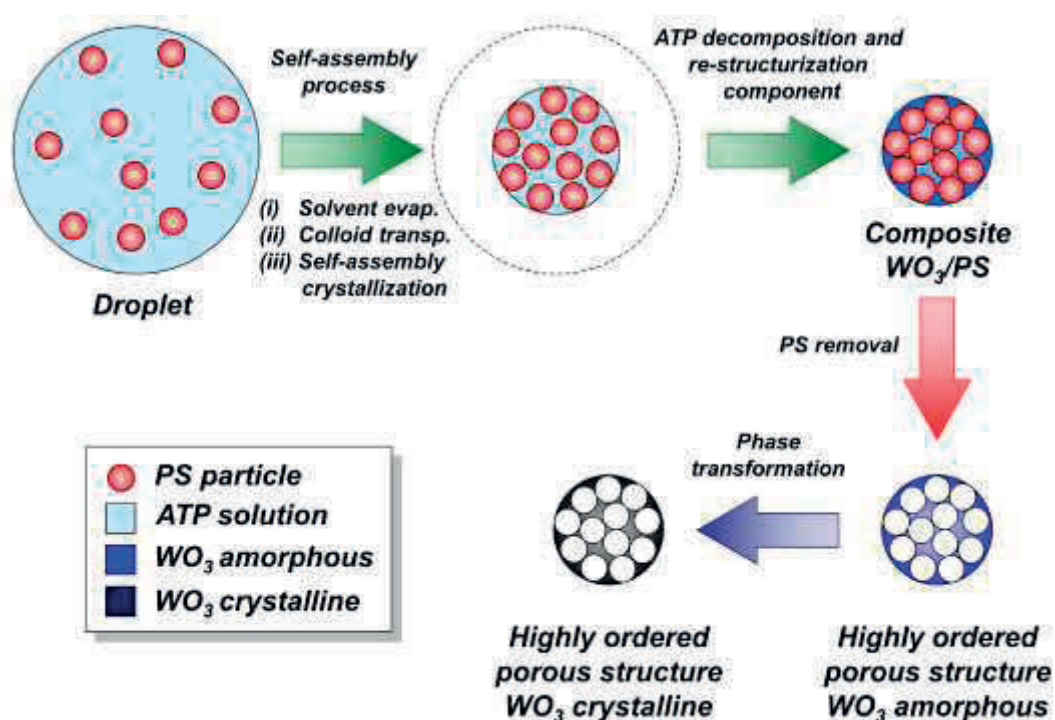


Fig. 4.3. Schematic diagram of mechanism of porous WO₃ particle formation during spray-pyrolysis.

Figure 4.5d–f that the particles produced using some of the PS/ATP mass ratios had the same porous structures on the outer surfaces of the particles. During the self-assembly process, the PS spheres are initially arranged on the outer layer, and fill the next layer after all the outer layer spaces are fully occupied. The optimum condition for obtaining highly ordered porous particles was achieved when the PS/ATP mass ratio was 0.60.

The maximum packing arrangement of macropores was only achieved using this mass ratio, and deviations from this mass ratio resulted in non-optimum porous structures.

To confirm the structures of the pores in the particles, three-dimensional tomography analysis was conducted (**Figure 4.6**). The results were consistent with the above SEM and TEM results, and showed that the addition of PS to the initial precursor allowed the creation of holes in the particles (**Figure 4.6a**), and addition of increasing amounts of PS led to the production of particles with highly ordered macroporous structures (**Figure 4.6b**). In the case of the particle shown in **Figure 4.6b**, connecting holes can be clearly seen, implying that the PS spheres were connected each other.

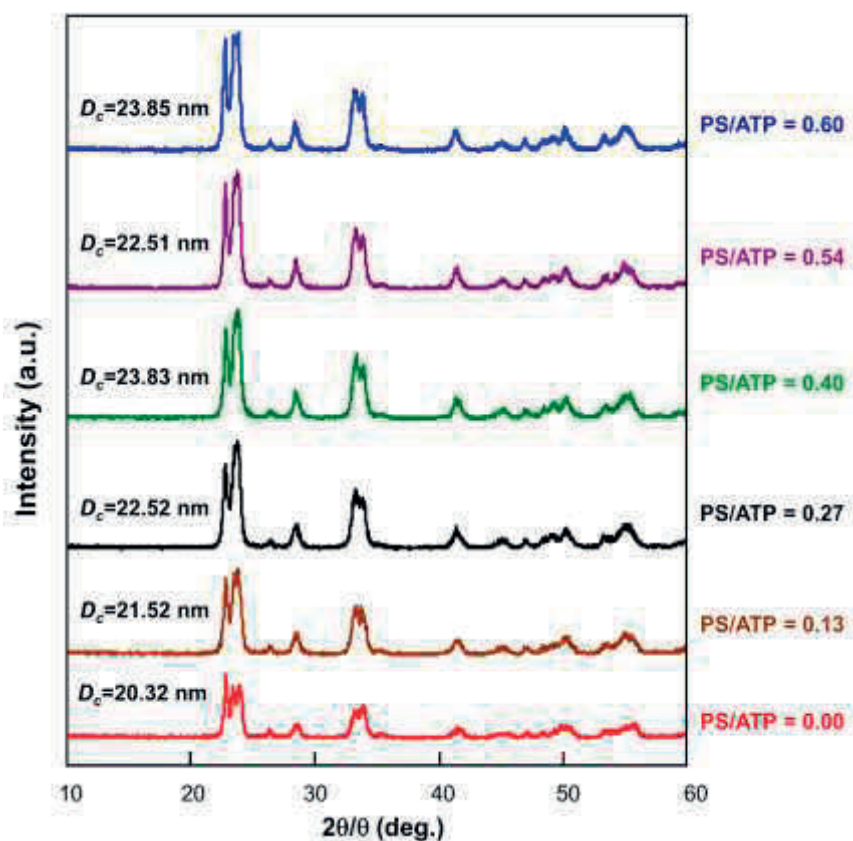


Fig. 4.4. XRD patterns of particles prepared using various PS/ATP mass ratios.

In addition, we found a difference between the pore and the PS sizes, in which this pore formation was different from our previous work that the size of pores is completely identical to those of initial PS spheres. [22] This pore shrinkage

phenomenon is due to two factors. The first factor is due to sintering phenomenon during the template removal process. This pore shrinkage can be controlled by changing template size and process parameters (i.e. temperature, flow rate, heating rate, etc) [19]. The second factor is due to existence of NH₃ that is released from the ATP. In the high temperature, this NH₃ can dissolve PS spheres, making final hole size to be smaller than their initial PS size. However, further investigations are required to confirm this control of pore size.

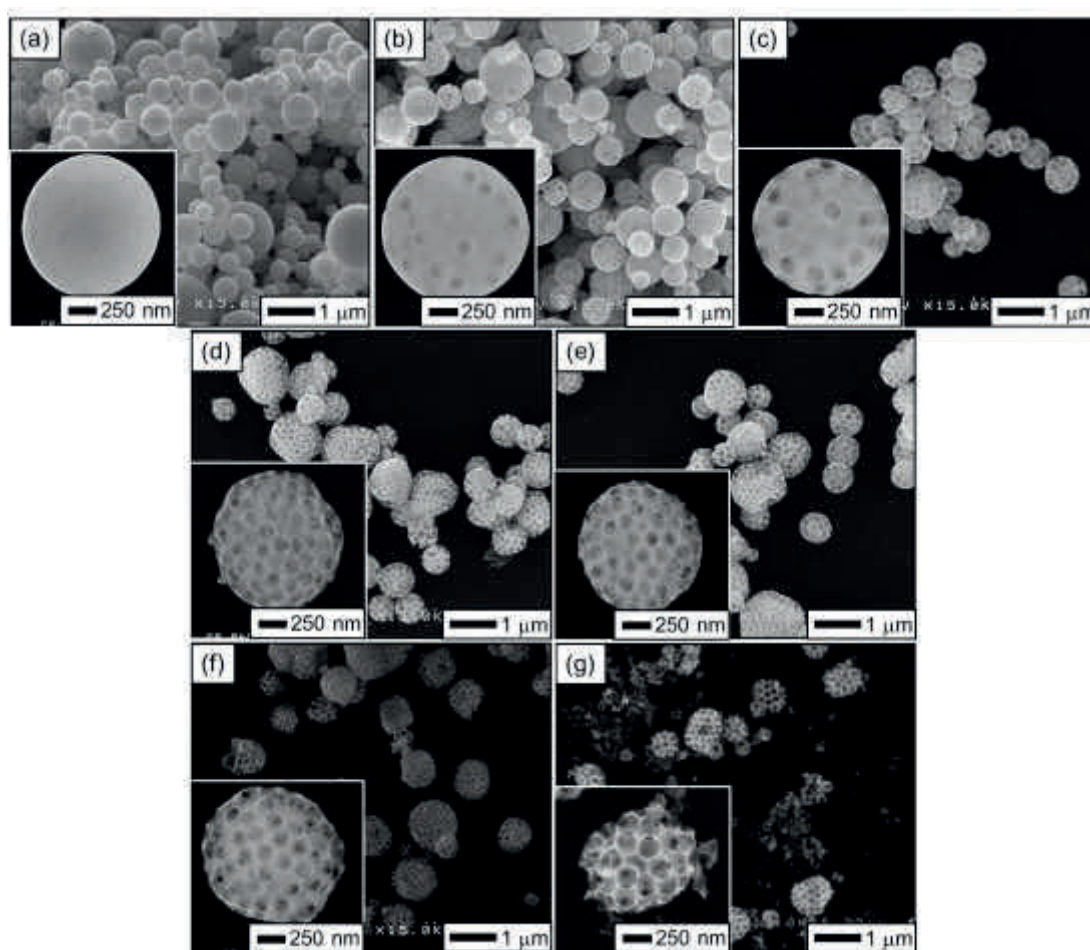
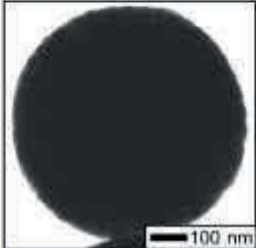
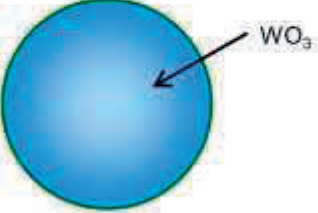
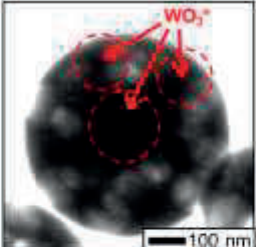
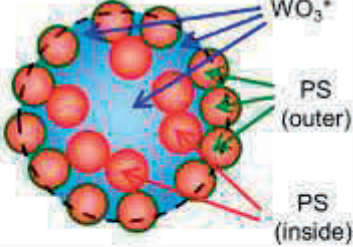
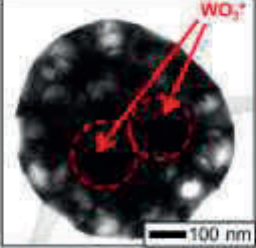
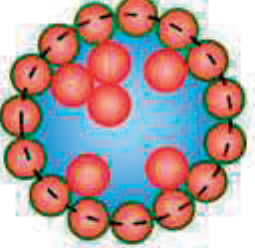
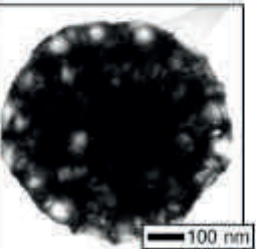
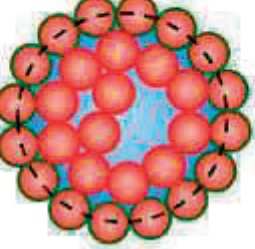


Fig.4.5. SEM images of particles prepared using different PS/ATP mass ratios: (a) 0.00; (b) 0.13; (c) 0.27; (d) 0.40; (e) 0.54; (f) 0.60; and (g) 0.64.

On the basis of the above experimental results in the case of PS/ATP mass ratio, the proposed effect of the PS/ATP mass ratio (x) on the typical particle porous structure

is shown in **Figure 4.7**. The particles were prepared by spray-pyrolysis of precursors containing ATP and PS. After the precursor was atomized and introduced into the furnace, five routes to particle formation are possible, with the final particle morphology depending on the value of x . When a precursor without any additional PS ($x = 0.00$) is used, dense particles are formed (route R1). The addition of PS to the precursor enables the creation of porous particles, as shown in routes R2–R5. When low mass ratio

Table 4.1. TEM Images of Particles Prepared Using Different Mass Ratios of PS/ATP and Predicted PS Arrangements in the Particles.

| Sample | PS/ATP mass ratio | Experimental result | Predicted PS pattern |
|--------|-------------------|---|--|
| A | 0.00 |  |  |
| B | 0.13 |  |  |
| C | 0.40 |  |  |
| D | 0.60 |  |  |

($x < 0.20$) is used, incomplete porous structures are formed in the particles (route R2). The use of a higher mass ratio ($x = 0.20$ – 0.55) leads to the production of porous particles (route R3). However, a good arrangement of pores is achieved only on the outer surface of the particles, and there are areas unoccupied by PS inside the particles. Further increases in the mass ratio to an appropriate value result in the preparation of highly ordered porous particles (route R4). In route 4, unlike the case of route R3, pores are present not only on the outside but also inside the particles. However, above the optimum amount of PS ($x > 0.60$), disrupted and irregular porous particles appear (route R5). Although the maximum porous structures can be produced, the WO₃ skeleton is too thin, making the skeleton unstable and unable to support and maintain the porous structure.

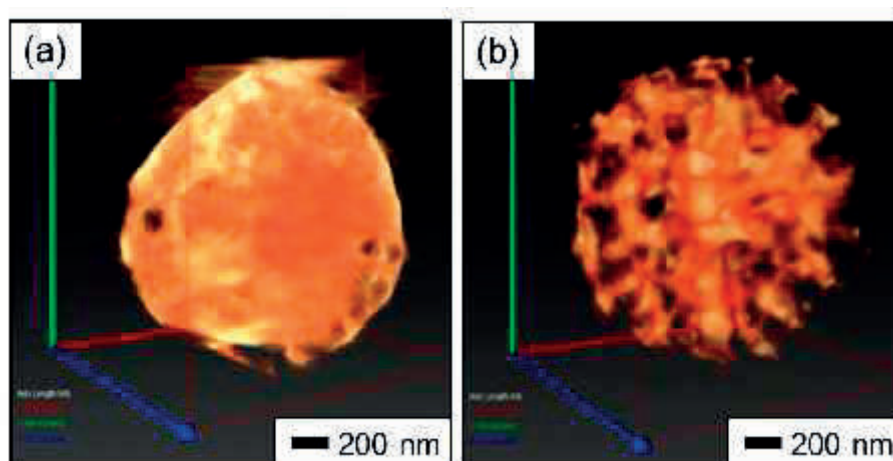


Fig. 4.6. Three-dimensional tomography images of particles prepared using different PS/ATP mass ratios: (a) 0.27 and (b) 0.60.

4.3.3 Effect of Precursor Concentration on Porous Particle Outer Diameter.

SEM images of particles prepared using various initial precursor concentrations are shown in **Figure 4.8**. The results in **Figure 4.8a–d** show that precursor concentrations of down to 10 g/L caused the production of submicron particles. This is consistent with the results of the investigation into the effect of the PS/ATP mass ratio, which showed that changes in the mass ratio affect the number of pores in the particle. When no PS was added, particles with solid structures were

produced (Figure 4.8a). The addition of PS resulted in the appearance of pores in the particles (Figure 4.8b–c). In the case of addition of a low amount of PS (Figure 4.8b), individual pores were clearly observed, and the pores existed separately. However, when large amounts of PS were added (Figure 4.8c), connected pores were created (shown by the red arrows in the figure and described as a “kissing effect”).

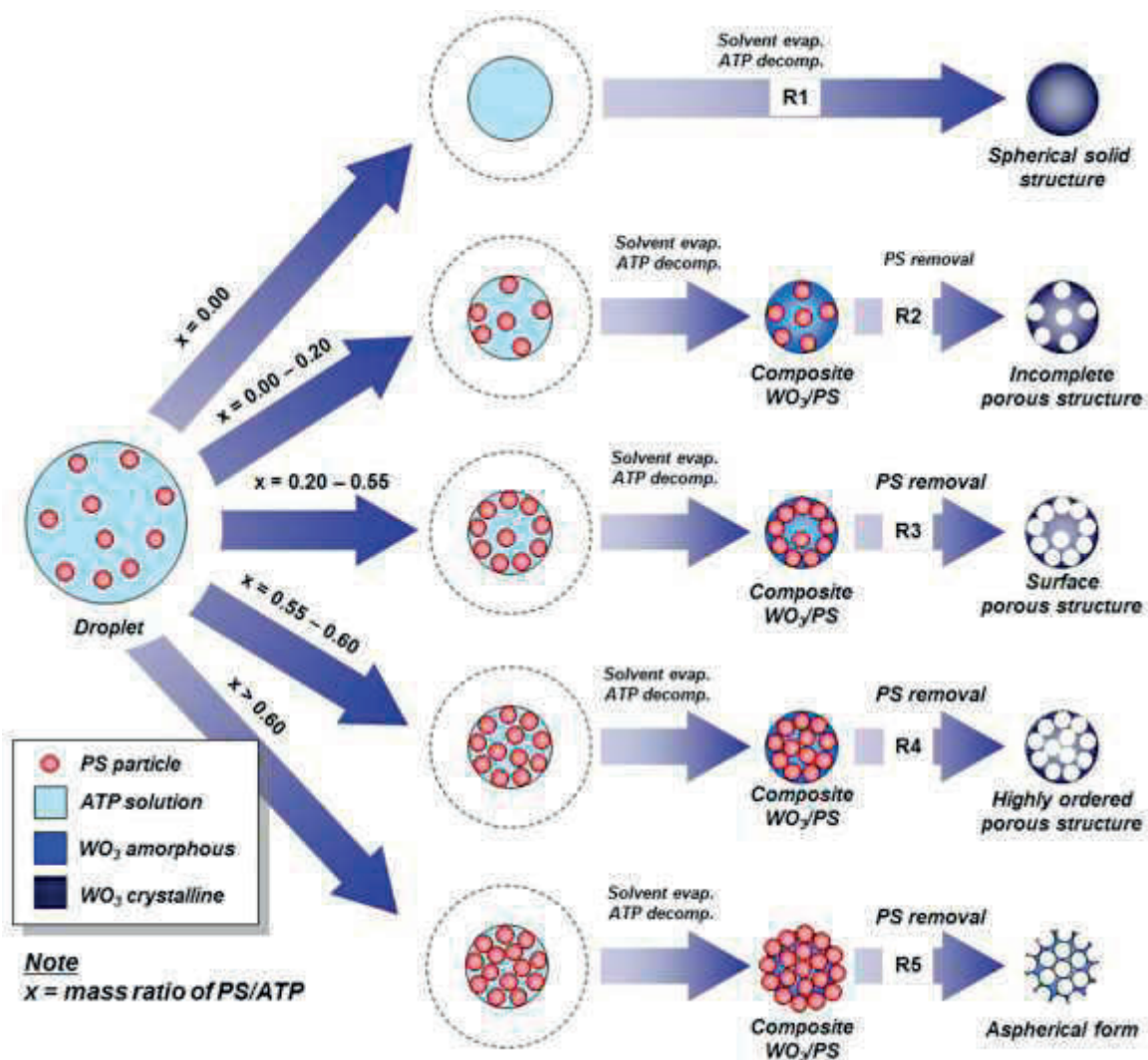


Fig. 4.7. Effect of PS/ATP mass ratio on proposed particle formation mechanism.

Figure 8d and e show low-magnified TEM images of the particles prepared using various initial precursor concentrations and a PS/ATP mass ratio of 0.60. The Ferret diameters of the porous particles produced using initial precursor concentrations

of 10 and 100 g/L were 632 and 1539 nm, respectively. Although the diameter increased with increasing precursor concentration, the porous structures were maintained, demonstrating an additional advantage of the present method: the ability to control the outer diameter of the porous product only by changing precursor concentration.

4.3.4 Enhancement of Material Performance by Porous Structure Formation.

Figure 4.9 shows the effect of pore structure formation in the WO₃ particles on the photodegradation rate of RhB. The molecular structure of RhB is shown in inset (i). A molecule of this size ($1.44 \times 1.09 \times 0.64 \text{ nm}^3$) (Nandiyanto *et al.*, 2009b) can effectively penetrate to the deepest positions inside a porous catalyst if the catalyst has a pore size in the macroporous range. The photodegradation of this type of molecule therefore provides information on the precise effect of the formation of macroporous structures in the particles on the enhancement of material properties.

During the photocatalytic process, the RhB concentration gradually decreased with increasing time (solid lines), while RhB was stable in the absence of a catalyst (dashed line). Simplified Langmuir–Hinshelwood kinetics was used to confirm the photodegradation rate (k) [12]. As shown in the figure, changes in the PS/ATP mass ratio affected the photocatalytic performance. When particles prepared from the precursor with a mass ratio of 0.00 were used as the photocatalyst, the k value was 0.1579 min^{-1} . For particles prepared using precursors containing PS, the k values were in the range $0.2201\text{--}0.3822 \text{ min}^{-1}$. The value of k increased with increasing amount of PS. The best photocatalytic rate was obtained using particles synthesized from a precursor with a PS/ATP mass ratio of 0.60; the photocatalytic rate obtained using these porous particles was 2.5 times that achieved using dense particles. Fading of the red color was also observed (shown in inset ii).

The outer diameters and the crystallite sizes of all the WO₃ samples were the same, showing that the particle morphology played important role in changing photocatalytic behaviors of catalyst. To explain the fundamental reason of the enhancement of photocatalytic activity by the existence of porous structure, a simple geometrical model is used to describe the improvement of photocatalytic performance

by the additional pores in the particle. In applying this topological model to optimize the surface area calculation, several assumptions should be made: (1) There is neither component loss during the self-assembly process; (2) PS spheres facilitate mainly the material construction, whereas other components completely fill the voids between the arrangement of PS spheres only; (4) All PS spheres self-assemble into the maximum pattern, pack with multilayer structure in the droplet, and arrange with no distortion associating with the maximum packing arrangement; (5) All PS spheres are removed completely during the template removal process, leaving pores in the final product; (6) There is no effect in the change volume of ATP after conversion; In general, the volume of ATP and WO₃ are the same; and (7) the generated porous particles have a homogenous pore size and porous structure with no existence of mesoporous pattern.

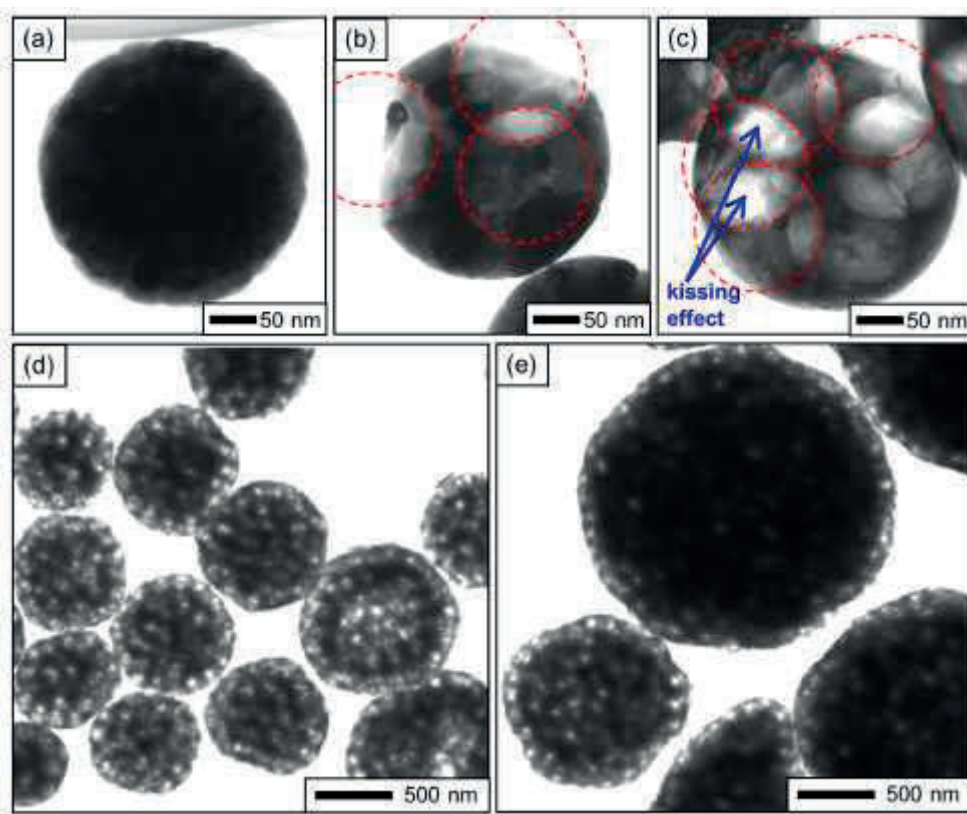


Fig. 4.8. TEM images of particles prepared using various PS/ATP mass ratios, (a) 0.00, (b) 0.40, and (c) 0.60, in a total precursor concentration of 10 g/L; (d) and (e) are low-magnification TEM images of samples (PS/ATP mass ratio 0.60) prepared using total precursor concentrations of 10 and 100 g/L, respectively.

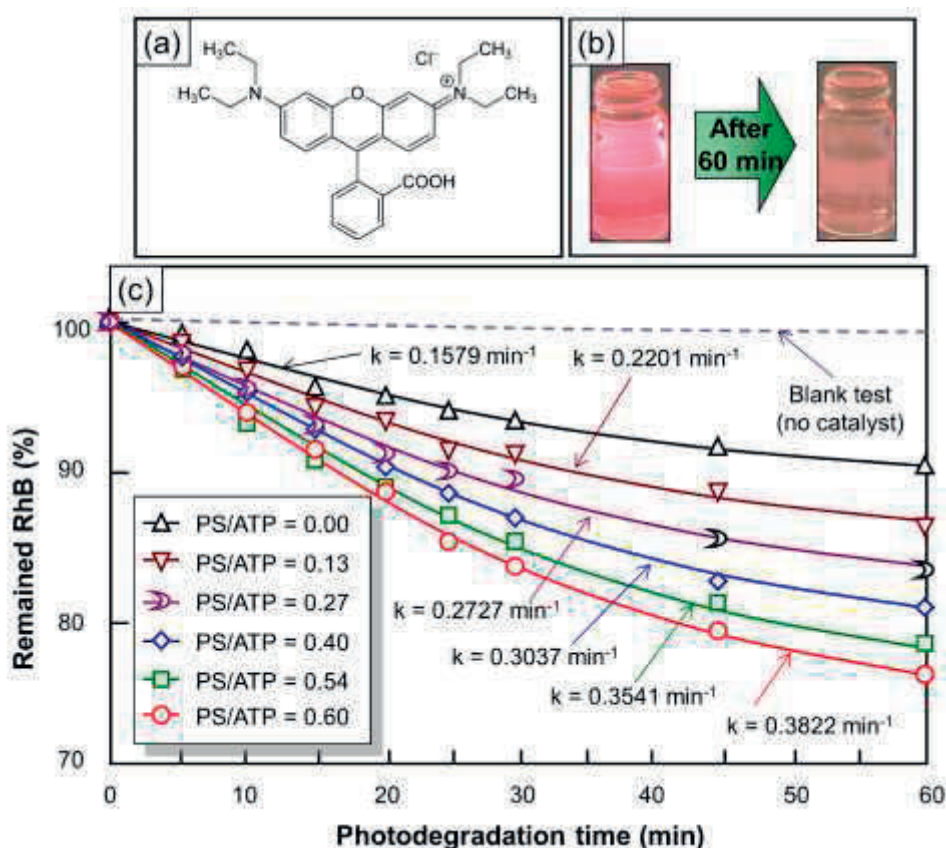


Fig.4.9. Photodegradation of RhB over time by WO₃ particles with various PS/ATP mass ratios. Empirically determined rate constants for each particle type are also given as k values. Insets: (i) molecular structure of RhB and (ii) digital camera photographs of RhB before and after photocatalytic process using WO₃ prepared using a PS/ATP mass ratio of 0.60.

Using the above assumption, the apparent density of porous particle (ρ_{app}) can be calculated as

$$\rho_{app} = v \cdot \rho_{air} + (1 - v) \rho_{ATP} \quad (4.1)$$

where v is the void fraction of the particle occupied by air, ρ_{air} is the density of air, and ρ_{ATP} is the density of ATP. The void fraction of the porous particles is defined by the volume of PS spheres (V_{PS}) and ATP (V_{ATP}) in forming particle. Derivation of the void calculation is

$$V = \frac{V_{PS}}{V_{PS} + V_{ATP}} = \frac{\frac{m_{PS}}{\dots_{PS}}}{\frac{m_{PS}}{\dots_{PS}} + \frac{m_{ATP}}{\dots_{ATP}}} \quad (4.2)$$

where m_{PS} and m_{ATP} are the mass of PS and ATP, respectively. Then, substituting

$$x = \frac{m_{PS}}{m_{ATP}} \text{ to equation (2) results}$$

$$1 - V = \frac{\dots_{PS}}{x \dots_{ATP} + \dots_{PS}} \quad (4.3)$$

Adopting the air density (\dots_{air}) of 0.0012 g/mL, the equation (1) can be simply defined by

$$\dots_{app} = (1 - V) \dots_{ATP} \quad (4.4)$$

After simple transformation, the final expression can be defined as

$$\dots_{app} = \frac{\dots_{ATP} \dots_{PS}}{x \dots_{ATP} + \dots_{ATP}} \quad (4.5)$$

Table 4.2. BET Surface Areas and Photocatalysis Rate Constants (Determined Empirically from Photodegradation of RhB) of Different Types of WO₃ Particles.

| Sample type (PS/ATP) | S_{BET} | S_{BET}^{dense}/S_{BET} | A_m/A_m^{dense} | k/k^{dense} |
|-------------------------|-----------|---------------------------|-------------------|---------------|
| 0.00 | 2.75 | - | - | - |
| 0.13 | 5.80 | 2.11 | 2.20 | 1.38 |
| 0.27 | 7.84 | 2.85 | 3.05 | 1.69 |
| 0.40 | 9.68 | 3.52 | 3.67 | 1.88 |
| 0.54 | 11.49 | 4.18 | 4.15 | 2.19 |
| 0.60 | 12.07 | 4.39 | 4.38 | 2.38 |

Above equation replies that with the additional pores, the density of the particles decreases. For example, applying the standard density of ATP (2.30 g/mL) and PS (1.05 g/mL), the density of porous particles prepared with a PS/ATP mass ratio of 0.60 is 0.99 g/mL, in which this is 43% of density of non-porous WO₃ particles. Therefore, in the

same weight of photocatalysts used in the tests (i.e. with and without porous structure), the particle number increases more than twice, followed by the increase of total surface area of the catalyst.

To confirm the effect of porous structurization, Table 4.2 summarizes the photocatalytic performances and BET surface area of the samples. All the results were in qualitative agreement with each other. The photocatalytic rate was proportional to the mass ratio of PS/ATP, and this mass ratio determined the particle surface area, in which the results were in a good correlation with above theoretical calculation. Particles with porous structure have better photooxidation than those without porous structure. When adding porous structure, the number of active WO₃ components that are on the top surface increases. Indeed, it is well-known that only the top surface of catalyst can be activated by photon and interacting with RhB molecules. This is therefore explaining that the photocatalytic performance of the particles prepared without the addition of PS is the worst, which is because of limitations on chemical interactions and excessive light adsorption on the outer surfaces of the particles only. In the case of porous particles, an increase in the pore number increases the available active surface area, so interactions and chemical reactions between RhB and WO₃ can occur on the active site on the pore inside the catalyst, enabling better photooxidation process. These results suggest that formation of macroporous structures in the particles improved the material performance.

In addition, we found nonlinear correlation among additional pore number, surface area, and photocatalytic activity. This implies that besides existence of porous structures, other parameters (i.e. crystal size, phase and pattern) must be considered in the photocatalytic process. These parameters will be performed in our future work.

Although above demonstrations have shown positive impacts of the existence of pore number on the improvement of catalytic performance, the investigation is within a strictly condition (particle outer diameter of 800 nm and pore size of 150 nm). For this reason, further investigations (e.g. existence of micro and mesoporous structure, macropore size, particle diameter, light penetration, dark conditioning, and crystal structure (size, phase, and pattern)) and detailed kinetic measurements for the improvement of the photocatalytic performance underscores the need for further studies and will be discuss in our future work.

4.4 Conclusions

Macroporous WO₃ particles were successfully prepared by the spray-pyrolysis method with colloidal templating. The porous particles were generated from a precursor solution containing ATP and PS spheres. The porous morphology and particle outer diameter were controlled by adjusting the PS/ATP mass ratio and precursor concentration, respectively. The creation of spherical pores that are identical in shape and size to the PS template potentially provides scope for further development (e.g., control of pore size). The photocatalytic performances of the prepared porous particles were higher than those of non-porous particles with similar outer diameters, confirming the effectiveness of formation of porous structures in enhancing material performance. We also found that a PS/ATP mass ratio of 0.60 provided WO₃ particles with a photocatalytic rate 2.5 times that of dense WO₃ particles. Because of their excellent performances, as a result of their porous structures, we suggest that the prepared porous WO₃ particles could be used widely in chemical and environmental engineering processes, such as industrial wastewater treatment and solar-related applications. Furthermore, this simple process for designing porous structures could be used to prepare many types of particles, with good control of porous structure, pore size, and particle diameter.

4.5 References

- [1] Liu, Y.; Li, Y.; Li, W.; Han, S.; Liu, C., Photoelectrochemical properties and photocatalytic activity of nitrogen-doped nanoporous WO₃ photoelectrodes under visible light, *Applied Surface Science*, 258 (2012) 5038–5045.
- [2] Saepurahman, Abdullah, M.A.; Chong, F.K., Dual-effects of adsorption and photodegradation of methylene blue by tungsten-loaded titanium dioxide, *Chemical Engineering Journal*, 158 (2010) 418-425.
- [3] Sun, S.; Wang, W.; Zeng, S.; Shang, M.; Zhang, L.; Preparation of ordered mesoporous Ag/WO₃ and its highly efficient degradation of acetaldehyde under visible-light irradiation, *Journal of Hazardous Materials*, 178 (2010) 427-433.

- [4] Zheng, H.; Ou, J.Z.; Strano, M.S.; Kaner, R.B.; Mitchell, A.; Kalantar-zadeh, K., Nanostructured tungsten oxide-properties, synthesis, and applications, *Advanced Functional Materials*, 21 (2011) 2175-2196.
- [5] Nandiyanto, A.B.D.; Hagura, N.; Iskandar, F.; Okuyama, K.; Design of a highly ordered and uniform porous structure with multisized pores in film and particle forms using a template-driven self-assembly technique, *Acta Materialia*. 58 (2010) 282-289.
- [6] Baeck, S.H.; Choi, K.S.; Jaramillo, T.F.; Stucky, G.D.; McFarland, E.W.; Enhancement of photocatalytic and electrochromic properties of electrochemically fabricated mesoporous WO₃ thin films, *Advanced Materials*, 15 (2003) 1269-1273.
- [7] Teoh, L.G.; Shieh, J.; Lai, W.H.; Hung, I.M.; Hon, M.H.; Structure and optical properties of mesoporous tungsten oxide, *Journal of Alloys and Compds*, 396 (2005) 251-254.
- [8] Li, L.; Krissanasaeranee, M.; Pattinson, S.W.; Stefik, M.; Wiesner, U.; Steiner, U.; Eder, D., Enhanced photocatalytic properties in well-ordered mesoporous WO₃, *Chemical Communications*, 46 (2010) 7620-7622.
- [9] Huang, J.; Xu, X.; Gu, C.; Fu, G.; Wang, W.; Liu, J., Flower-Like And Hollow Sphere-Like WO₃ porous nanostructures: selective synthesis and their photocatalysis property, *Materials Research Bulletin*, 47 (2012) 3224–3232.
- [10] Singh, S.; Festin, M.; Barden, W.R.T.; Xi, L.; Francis, J.T.; Kruse, P.; Universal method for the fabrication of detachable ultrathin films of several transition metal oxides, *ACS Nano*, 2 (2008) 2363-2373.
- [11] Chen, W.H.; Lai, M.Y.; Tsai, K.T.; Liu, C.Y.; Wang, Y.L.; Spontaneous formation of ordered nanobubbles in anodic tungsten oxide during anodization, *Journal of Physical Chemistry C*, 115 (2011a) 18406-18411.
- [12] Nandiyanto, A.B.D.; Iskandar, F.; Okuyama, K., Macroporous anatase titania particle: aerosol self-assembly fabrication with photocatalytic performance, *Chemical Engineering Journal*, 152 (2009a) 293-296.
- [13] Sadakane, M.; Sasaki, K.; Kunioku, H.; Ohtani, B.; Ueda, W.; Abe, R., Preparation of nano-structured crystalline tungsten (vi) oxide and enhanced photocatalytic

- activity for decomposition of organic compounds under visible light irradiation, *Chemical Communications*, 44 (2008) 6552-6554.
- [14] Sumida, T.; Wada, Y.; Kitamura, T.; Yanagida, S., Electrochemical change of the photonic stop band of the ordered macroporous WO₃ films, *Chemistry Letter*, 31 (2002) 180-181.
- [15] Chen, X.; Ye, J.; Ouyang, S.; Kako, T.; Li, Z.; Zou, Z., Enhanced incident photon-to-electron conversion efficiency of tungsten trioxide photoanodes based on 3D-photonic crystal design, *ACS Nano*, 5 (2011b) 4310-4318.
- [16] Lv, K.; Li, J.; Qing, X.; Li, W.; Chen, Q., Synthesis and photo-degradation application of WO₃/TiO₂ hollow spheres, *Journal of Hazardous Mater*, 189 (2011) 329-335.
- [17] Leghari, S.A.K.; Sajjad, S.; Chen, F.; Zhang, J., WO₃/TiO₂ composite with morphology change via hydrothermal template-free route as an efficient visible light photocatalyst, *Chemical Engineering Journal*, 166 (2011) 906-915.
- [18] amano, f.; nogami, k.; tanaka, m.; ohtani, b., correlation between surface area and photocatalytic activity for acetaldehyde decomposition over bismuth tungstate particles with a hierarchical structure, *langmuir*, 26 (2010) 7174-7180.
- [19] gradoń, l.; janeczko, s.; abdullah, m.; iskandar, f.; okuyama, k., self - organization kinetics of mesoporous nanostructured particles, *aiiche journal*, 50 (2004) 2583-2593.
- [20] nandiyanto, a.b.d.; kim, s.g.; iskandar, f.; okuyama, k., synthesis of spherical mesoporous silica nanoparticles with nanometer-size controllable pores and outer diameters, *microporous and mesoporous materials*, 120 (2009b) 447-453.
- [21] nandiyanto, a.b.d.; okuyama, k., progress in developing spray-drying methods for the production of controlled morphology particles: from the nanometer to submicrometer size ranges, *advanced powder technology*, 22 (2011) 1-19.
- [22] nandiyanto, a.b.d.; suhendi, a.; arutanti, o.; ogi, t.; okuyama, k., influences of surface charge, size, and concentration of colloidal nanoparticles on fabrication of self-organized porous silica in film and particle forms, *langmuir* 29 (2013) 6262-6270.

- [23] nandiyanto, a.b.d.; suhendi, a.; ogi, t.; iwaki, t.; okuyama, k., synthesis of additive-free cationic polystyrene particles with controllable size for hollow template applications, *Colloid Surface A*, 396 (2012) 96-105.

Chapter 5

Influence of Porous Structurization and Pt Addition on the Improvement of Photocatalytic Performance

5.1. Introduction

Tungsten trioxide (WO_3) is one of excellent materials because of its excellent attributes: relatively harmless, chemically and thermally stable, good photostability, and chemically and biologically inert [1]. Its excellent attributes make this material prospective for wide range of applications (e.g. electrocatalysts, sensors, photochromic devices, and photocatalysts) [2-8]. However, its use is limited by several disadvantages: WO_3 is expensive and rare [9]. Further, although WO_3 is active under visible light, pure WO_3 material has a low efficiency.

Extensive efforts have been devoted to improve the performance of WO_3 as a catalyst. We briefly described the previous researches to provide context for the novel approach that will be presented in the present study regarding to the morphology control and Pt addition as a co-catalyst. Huang *et al.* [10] and de Respinis *et al* [1]. reported the synthesis of mesoporous WO_3 materials. Although the presence of mesoporous structure enhances the photocatalytic performance, some limitations associated with mesoporous structures remain. Mesoporous structures can easily collapse upon long heat treatments. Furthermore, the presence of a small pore size regime entails difficulties associated with mass transfer and diffusivity, and the transport of molecules either in or out of the pore system. To maximize the number of active components, Ashkarran *et al.* [11] and Martínez-de La Cruz *et al.*[12] reported the synthesis of nanometer-sized WO_3 particles. The use of nanoparticles is effective to maximize the number of WO_3 active components and improve photocatalytic performance. However, the downstream processes employed for reuse or removal of the nanoparticles is typically expensive, and direct disposal of nanoparticles poses several environmental problems. Incorporation of

Pt metal as co-catalyst was also reported as other alternative ways to improve the catalytic activity of WO_3 [9,13-19]. However, current methods require specific and complex synthetic equipment with rigorous conditions. Furthermore, most of the reports describe the synthesis of WO_3 materials from tungsten salt. The use of tungsten salt typically leads to the formation of a compact and dense material that features inactive components in the inner regions of the catalyst. These inner components cannot interact with the target molecule and light for molecule photodegradation.

In our previous studies, we also successfully synthesized WO_3 particles using a spray-pyrolysis method. We focused on morphological control (i.e., particle size and shape) [20], crystal structure optimization [21], and co-catalyst incorporation [22,23]. However, we did not concern on towards optimizing photocatalytic performance more. Specifically, we used tungsten salt as a WO_3 particles source [24].

Herein, we report the synthesis of spherical macroporous Pt-modified WO_3 particles via a spray-drying method. Different with our previous reports, here we used WO_3 nanoparticles as a WO_3 source that is expected to produce larger surface areas. The internal morphology of WO_3 particles was controlled using polystyrene (PS) sphere as the sacrificial colloidal templates in the initial precursor. The current method also affords control of the porous structure in the particle by varying the PS-to- WO_3 mass ratios, whereas most reported papers have not examined. This method has potential for generating efficient materials but using relatively low amounts of raw materials.

The photocatalytic studies showed that changes in the morphology and incorporation of Pt as a co-catalyst were effective to improve the photocatalytic performance over WO_3 nanoparticles. The experimental results were also supported by a proposal mechanism of the photocatalytic reaction phenomenon. In addition, owing to the size of the prepared particles that is within the submicron range, the particles have prospects in industry-related applications because they can be collected easily from the waste solution and reusable.

5.2 Experimental

5.2.1 Preparation of spherical macroporous Pt-modified WO_3 particles

Spherical macroporous WO₃ particles were prepared from a precursor solution containing WO₃ nanoparticles (Nisshin Engineering Inc., Japan; a mean size of 10 nm) and 250-nm polystyrene spheres (PS; synthesized from styrene monomer (Kanto Chemical Co., Japan) and 2,2'-azobis (isobutyramidine) dihydrochloride (Sigma–Aldrich, USA)). Detailed information on the synthesis of the PS spheres is provided in our previous study.²⁵ To tailor the porous structure of the particle, we varied the PS/WO₃ mass ratio from 0.00 to 0.40. To prepare WO₃ with added Pt co-catalyst, hydrogen hexachloroplatinate (IV) hexahydrate (H₂PtCl₆•6H₂O; Sigma–Aldrich, US) was added to the precursor. In addition, prior to add PS into the precursor, 0.40 wt% of polydiallyldimethylammonium chloride (PDADMAC; Sigma–Aldrich, US) was added. The composition of the precursor solutions used in this study is shown in **Table 5.1**. The precursor was then introduced into the spray-drying apparatus schematically depicted in **Figure 5.1**. Detailed information about spray-drying apparatus and mechanism is reported in elsewhere.²⁶ Briefly, the apparatus consisted of an ultrasonic nebulizer (NE-U12; Omron Corp., Japan; operating at a frequency of 1.7 MHz), a ceramic tubular furnace (diameter of 30 mm and length of 1.3 m) with two temperature-controlled zones set at 200 and 600 °C, and a filter. To introduce the droplet generated by the ultrasonic nebulizer into the tubular furnace, air at a flow rate of 0.5 L/min was used. Additionally, we prepared spherical dense WO₃ particles using ammonium tungstate pentahydrate (ATP; Kanto Chemical Co., Japan) as a dense particle with a smooth surface as other comparison.

5.2.2 Characterization

To examine the morphology of the prepared particles, a scanning electron microscope (SEM; S-5000; Hitachi Co., Japan; operating at 20 kV) and a transmission electron microscope (TEM; JEM-3000 F; JEOL Co., Ltd., Japan; operating at 300 kV) were used. The crystallinity and phase structure of the prepared particles were examined using an X-ray diffraction (XRD; Rigaku Denki RINT2000, Japan; using Cu K α radiation and a 2 θ scanning range of 20–80°). Thermal analysis of the samples was conducted on a thermal gravity and differential thermal analyzer (TG–DTA; Exstar6000; Seiko Instruments, Inc., Japan; using a heating rate of 5°C/min and carrier

Table 5.1. Composition of raw materials used in the precursors.

| Type | WO ₃ source | UPW ^(a) | PS ^(b) | Pt source ^(c) |
|--|--------------------------------------|--------------------|----------------------|--------------------------|
| Dense particles | ATP (6.3 g) | 100 mL | - | - |
| Aggregated particles | WO ₃ nanoparticles (4.00) | 100 mL | - | - |
| Aggregated particles with macropores | WO ₃ nanoparticles (4.00) | 100 mL | 24 mL ^(d) | - |
| | WO ₃ nanoparticles (4.00) | 100 mL | 32 mL ^(e) | - |
| | WO ₃ nanoparticles (4.00) | 100 mL | 40 mL ^(f) | - |
| Aggregated particles with Pt | WO ₃ nanoparticles (4.00) | 100 mL | - | 1.20 mL |
| Aggregated particles with macropores and Pt | WO ₃ nanoparticles (4.00) | 100 mL | 32 mL ^(e) | 1.20 mL |

Note:

^(a) UPW = Ultra pure water;

^(b) We used 2.00 wt% of PS in water. Prior to add PS into the solution, 0.40 wt% of PDADMAC was added;

^(c) Prior to using, Pt source (H₂PtCl₆.6H₂O) was diluted into UPW with a concentration of 0.05 g/mL;

^(d) PS/WO₃ mass ratio = 0.24;

^(e) PS/WO₃ mass ratio = 0.32;

^(f) PS/WO₃ mass ratio = 0.40

gas (air) at a rate of 200 mL/min). Elemental mapping and chemical composition of the prepared particles were evaluated using a scanning transmission electron microscope (STEM) equipped with energy dispersive X-ray spectroscopy (EDS). Surface area was analyzed by using Brunauer-Emmett-Teller measurement (BET; BELSORP 28SA, Bel Japan, nitrogen adsorption isotherms at 77.15 K).

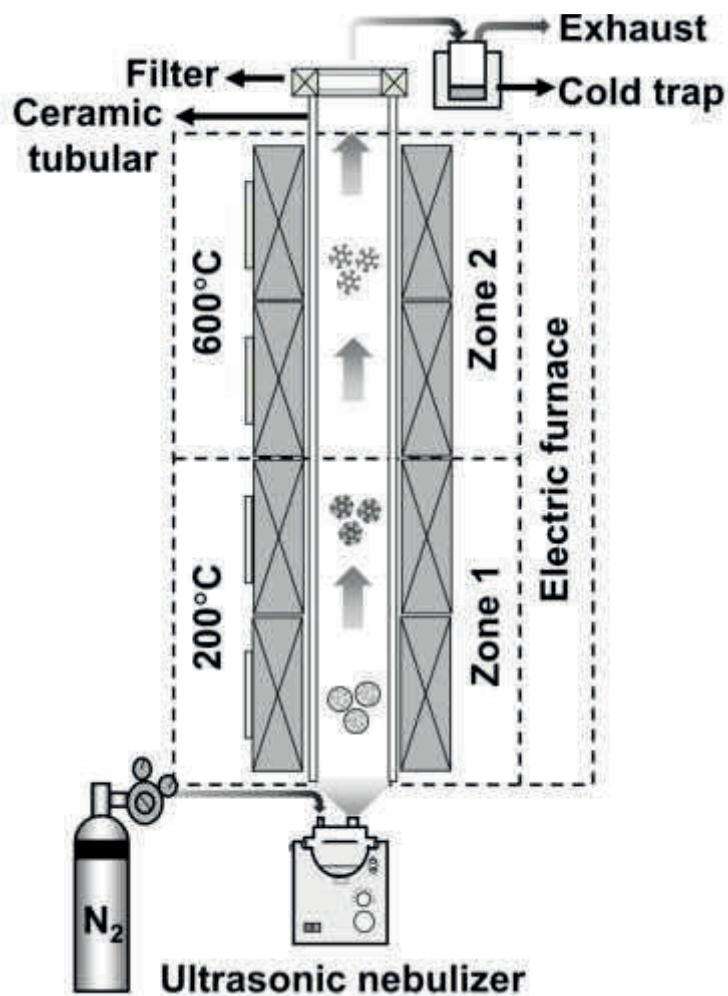


Fig. 5.1. Schematic illustration of the spray-drying apparatus.

The photocatalytic activity of the prepared particles was assessed by mixing 0.20 g of the prepared particles with 1.00 mg of rhodamine B (RhB; Wako Pure Chemical Industries Ltd., Japan) in 500 mL of aqueous solution. The mixed solution was introduced into the batch reactor equipped with a solar simulator system (PECL11, Peccell Technologies, Inc., Japan; AM 1.5G (100 mW/cm²)). To maintain the

concentration of dissolved oxygen during the photocatalytic process, 200 mL/min of oxygen was bubbled into the reactor. To measure the concentration of RhB in the reactor, 3 mL of the mixed solution was sampled every several minutes. Prior to analysis, the sampled solution was then centrifuged at 15,000 rpm for 5 min. The concentration of RhB in the sample was measured using a UV–Vis spectrophotometer (UV-3150; Shimadzu Corp., Japan).

5.3 Results and Discussion

5.3.1 Physicochemical properties of raw material

Figure 5.2 shows electron microscopy images of the raw materials used in this study (i.e. WO_3 nanoparticles and PS spheres). SEM images in **Figure 5.2a and b** showed that relatively monodisperse particles were obtained. The sizes of WO_3 and PS spheres were around 10 and 250 nm, respectively. TEM images in **Figure 5.2c and d** showed that all particles were dense. These results confirm that these colloidal materials can be used for preparing particles with homogenous structures.

To ensure the formation of porous structures within the particles, TG–DTA analysis was conducted (**Figure 5.3**). The three types of samples analyzed were “PS only”, “ WO_3 nanoparticles only”, and “PS/ WO_3 ” (prepared at a PS/ WO_3 mass ratio of 1.00). As observed, WO_3 sample displayed minimal mass losses with increasing heating temperatures. In contrast, samples containing PS (i.e. “PS only” and “PS/ WO_3 ” samples) exhibited a significant mass loss from 270°C. Then, the mass was relatively stable after passing temperatures of 400°C. The final masses of the “PS only” and “PS/ WO_3 ” samples were 0 and 48%, respectively. Because the amount of WO_3 added to the “PS/ WO_3 ” sample coincided with the final mass after the drying process, it can be concluded that the PS component was completely removed, generating pure WO_3 as the final product.

5.3.2. Preparation of spherical macroporous Pt-modified WO_3 particles

Figure 5.4 shows electron microscopy images of particles prepared with varying PS/ WO_3 mass ratios. For comparison, WO_3 particles prepared from ATP solution were also analyzed (**Figure 5.4a**).

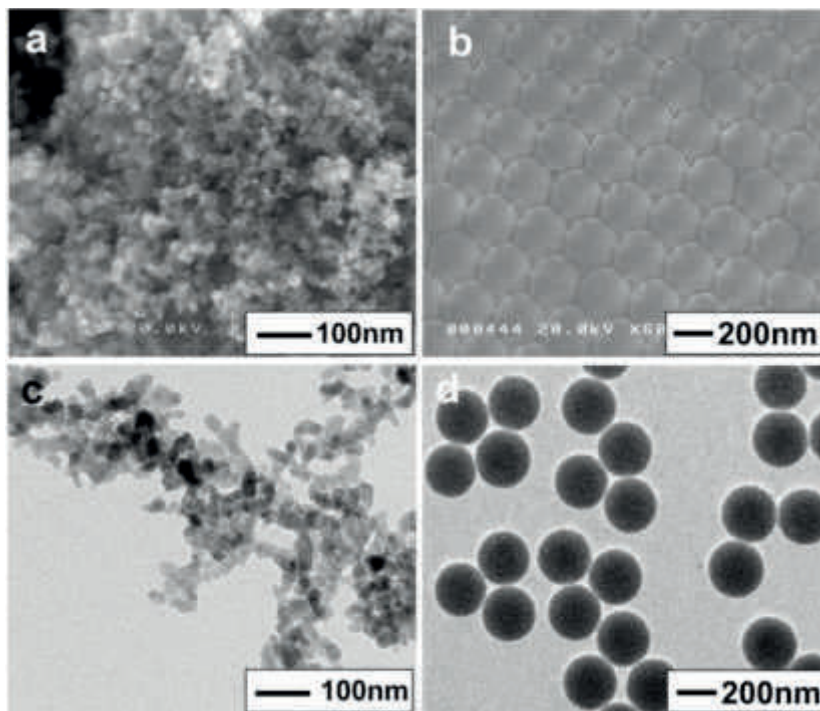


Fig. 5.2. Typical electron microscopy images of the raw materials used in this study: (a, c) WO_3 nanoparticles and (b, d) PS spheres. SEM and TEM images are shown in (a, b) and (c, d), respectively.

The use of precursor containing WO_3 source only resulted in particles without a macroporous structure (**Figure 5.4a and b**). When using the precursor containing ATP as the WO_3 source, the process produced spherical particles with a smooth surface and a mean size of about $0.6 \mu\text{m}$ (**Figure 5.4a**). The use of precursor containing WO_3 nanoparticles without PS addition generated particles with rough surface with a mean size of about $0.6 \mu\text{m}$ (**Figure 5.4b**). These results indicate that surface area of the prepared particles with a rough surface is higher than the particles with a smooth surface.

Figure 5.4c–e depicts SEM images of the spray-dried particles prepared with varying PS/ WO_3 mass ratios. The addition of PS to the precursor allowed the preparation of particles with macropores structure, whereby the number of macropores in the particle increased with increasing PS amounts. However, further increases in the PS amount resulted in fractured particles. The mean sizes of particles (showing in

Figure 4 c-e) were 0.8, 0.8, and 0.7 μm by increasing mass ratio of PS/WO₃ of 0.24, 0.32, and 0.40, respectively.

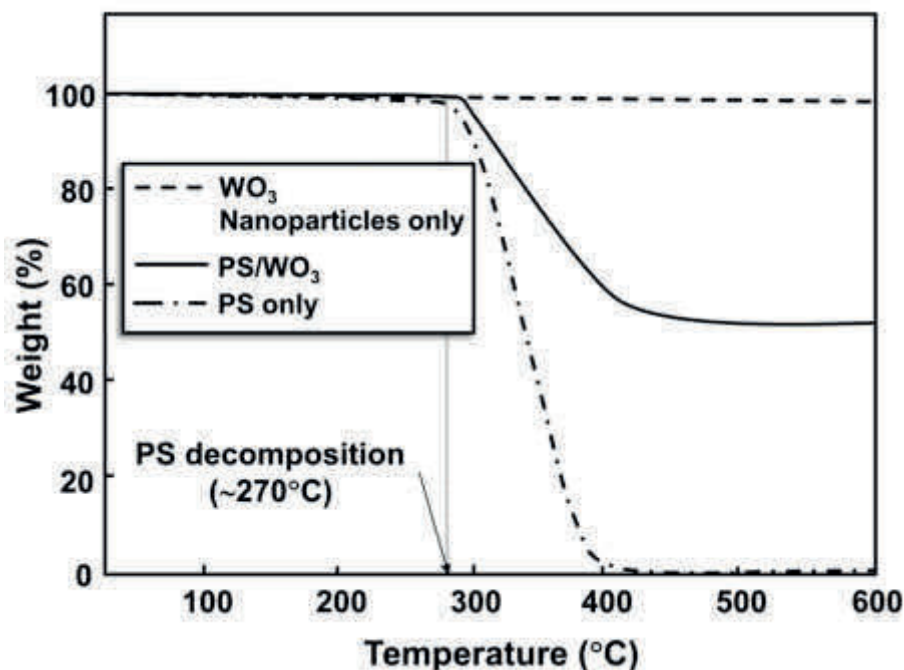


Fig. 5.3. TG-DTA analysis of “WO₃ nanoparticles only”, “PS/WO₃”, and “PS only” samples.

From the above results, the optimum ratio required for the production of highly ordered macroporous structures is 0.32 (**Figure 5.4d**). Deviation from the optimum mass ratio led to a disordered macropore arrangement. Insufficient mass ratios resulted in fewer macropores. In contrast, excessive mass ratios (excess content of PS in the precursor) inhibited disruption of the macroporous structure of the final particle (**Figure 5.4e**).

To further evaluate the macroporous structure of the particle, TEM analysis was conducted (**Figure 5.4f and g**). As shown in **Figure 5.4f**, the skeleton structure was due to the self-assembly of the WO₃ nanoparticles, resulted in the produce of small cavities. Furthermore, Pt metal was detected on the particle surface. Red was the example for the existence of agglomerate Pt on the particle surface (**Figure 5.4f**). The mean size of Pt

was of 1.9 nm. HRTEM image in **Figure 5.4g** exhibits the crystalline structure of WO_3 and Pt with the lattice spacing was of 3.8 Å and 2.29 Å, respectively.

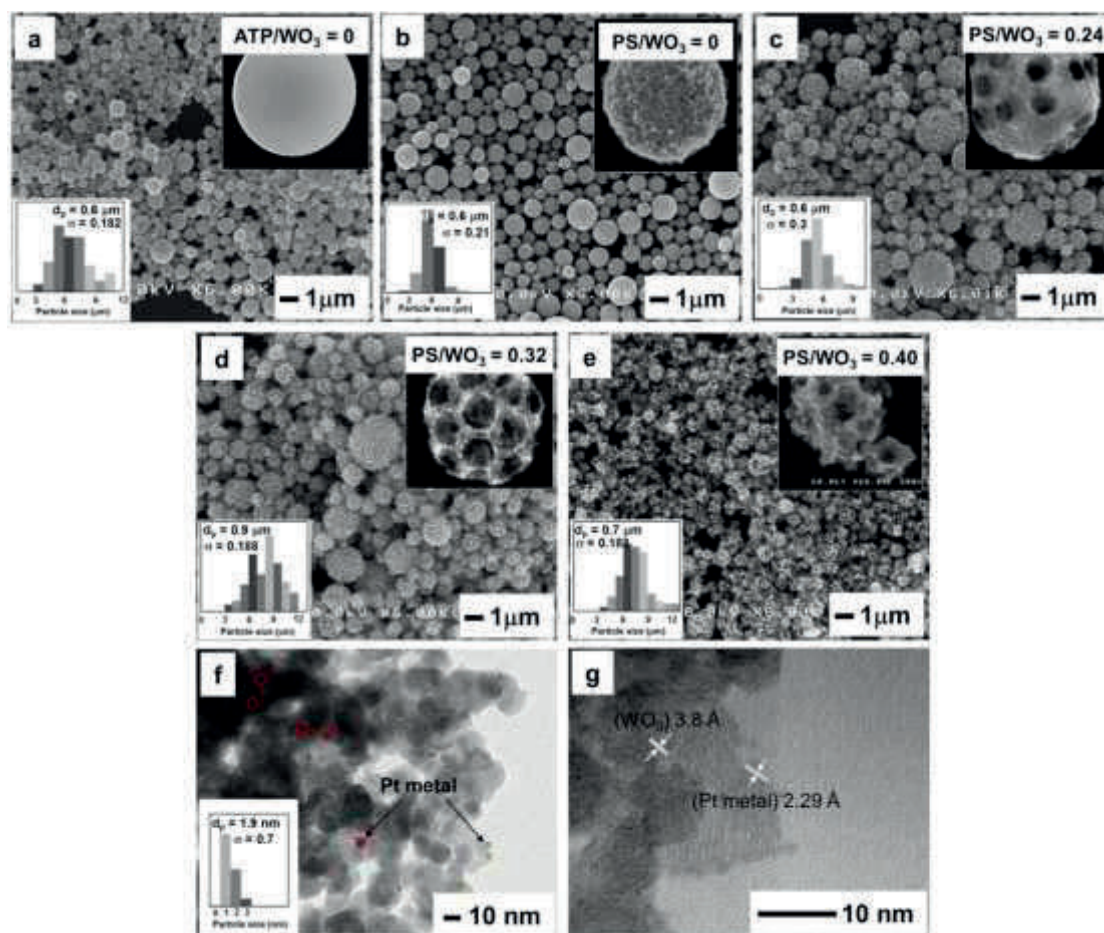


Fig. 5.4. SEM images of the spray-dried particles: (a) prepared from ATP and (b–e) prepared using varying PS/ WO_3 mass ratios of 0.00, 0.24, 0.32, and 0.40, respectively.

Figures (f–g) are the high-resolution TEM images of macroporous particles with the PS/ WO_3 mass ratio of about 0.32.

The structure and crystallite sizes of the prepared particles were identified by XRD patterns as depicted in **Figure 5.5**. The XRD patterns show that the all prepared particle were well consistent to the standard JCPDS no: 72-1465. This number was indexed to monoclinic structure of WO_3 with orientation 002, 020, and 200. The all crystallite sizes were determined to be ~6nm from the broadening peak area by using Scherrer method. The phase and pattern of the nanoparticles and spray-dried particles

were similar, suggesting that spray drying did not induce a change in the WO_3 crystallinity of the particle. Also, Pt peaks were not detected, likely because the content of Pt is lower than the detection limit of the XRD technique.

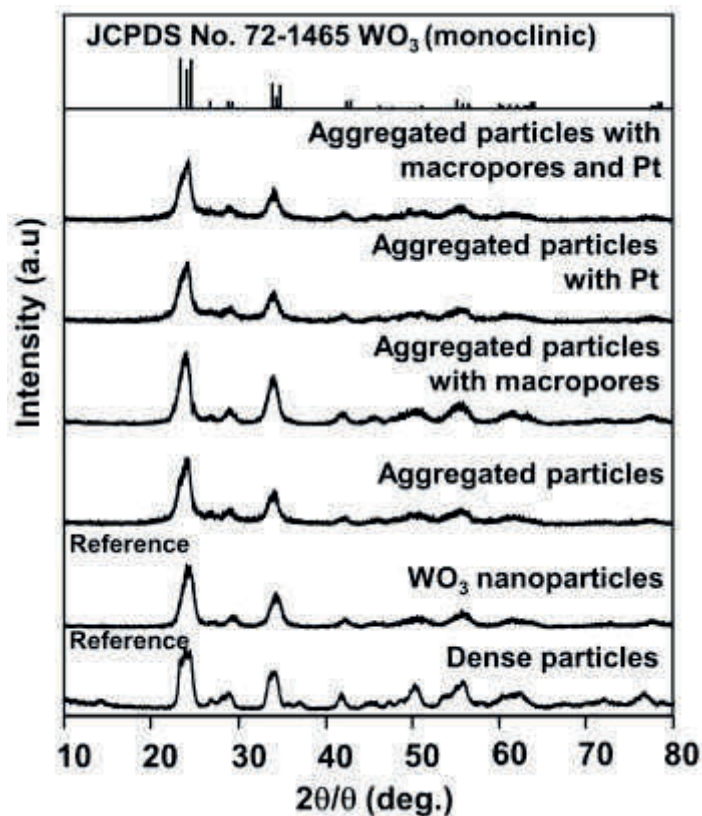


Fig. 5.5. XRD patterns of the as-prepared particles using varying compositions of PS and Pt addition in the precursor.

To confirm the existence Pt in the prepared particles, STEM, elemental mapping was conducted (**Figure 5.6**). STEM analysis revealed that the additional Pt did not affect the formation of the porous structure. The different color intensities confirming that the prepared particles contained W, O, and Pt elements. Yellow color from STEM image indicating that Pt metal was well distributed on the prepared particle. By added 0.28 wt% of Pt metal into the initial precursor, the final amount of Pt content on the prepared particles was of 0.23 wt%.

Based on the above results, the formation mechanism of the porous WO_3 particles is depicted in **Figure 5.7**, comprising the following three successive steps: self-assembly, solidification, and template removal.

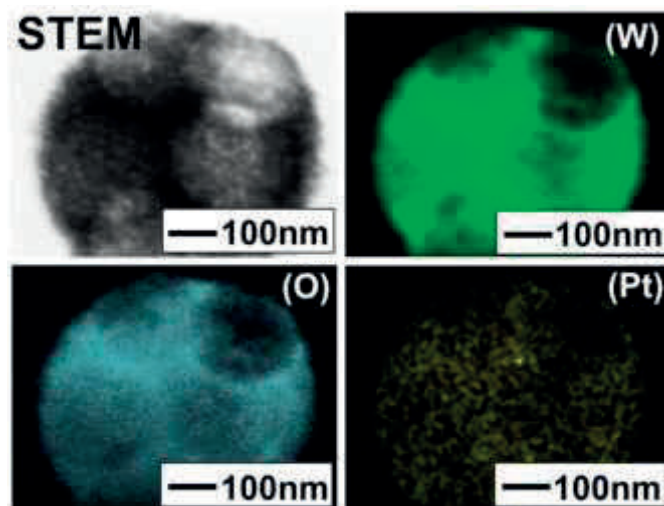


Figure 5.6. STEM image of prepared particle and corresponding elemental mapping images showing the presence of W, O, and Pt elements in the sample.

The self-assembly process occurs at temperatures below 270°C . This step involves solvent evaporation, colloids transportation, and components self-assembly. Additionally, owing to capillary forces, the smaller components (i.e., WO_3 nanoparticles and Pt ions) move faster to the periphery of the droplet than the larger component (i.e., PS).²⁶ Solidification between the components was subsequently occurs. Solvent evaporates from the droplet, forming composite particles. Finally, the composite particles are subjected to the template removal process. Based on TG–DTA analysis (**Figure 5.3**), all PS components are completely removed by 400°C , producing macroporous particles as a final product (**Figure 5.4**). During the synthesis process, the formation of $\text{H}_2\text{PtCl}_6 \cdot 6\text{H}_2\text{O}$ to Pt metal has following four steps.^{27,28} At low temperature, water evaporation occurs and following by the decomposition of all Pt solution to PtCl_4 at temperature starts from 150 to 300°C . When the temperature between 300 and 500°C , the PtCl_4 starts to decomposition become platinum dichloride (PtCl_2). After reaching the temperature of more than 520°C , Pt metal is completely formed.²⁸ The results in the

encapsulation of the large components by WO₃ and Pt components is confirmed by the existence of Pt on the particle surface (**Figure 5.4f**).

5.3.3 Photocatalytic performance of WO₃ particles

Figure 5.8 shows normalized RhB concentrations (with respect to the initial concentration) as a function of time of the photocatalytic experiments conducted under varying WO₃-based catalyst samples. The dotted line represents the blank test (WO₃-free system), whereas the solid line shows the variation in WO₃-based catalysts. As photocatalyst references, we also evaluated the process using WO₃ nanoparticles (open triangle markers) and WO₃ particles prepared from ATP (open circle markers). Unlike the blank test, the RhB concentrations in the presence of all WO₃-based catalysts decreased over time. To evaluate the photocatalytic degradation rate (k), a simplified Langmuir–Hinshelwood kinetics model was used. As observed, the degradation rate of RhB was dependent on the type of WO₃ catalyst. The lowest photocatalytic rate was obtained using WO₃ catalyst prepared from ATP ($k = 0.966 \cdot 10^{-3} \text{ min}^{-1}$). Changing the WO₃ source from ATP to WO₃ nanoparticles resulted in WO₃ catalyst with a higher catalytic performance (open square markers; $k = 2.352 \cdot 10^{-3} \text{ min}^{-1}$). However, the photocatalytic performance remained is lower than that of WO₃ nanoparticles, in which photocatalytic performance results of WO₃ nanoparticles are shown as open reverse triangle markers ($k = 2.976 \cdot 10^{-3} \text{ min}^{-1}$). The presence of additional pores in the particle improved the photocatalytic performance (solid circle markers; $k = 6.14 \cdot 10^{-3} \text{ min}^{-1}$), whereby the k value of the macroporous particles is twice that of WO₃ nanoparticles reference.

The presence of Pt co-catalyst considerably improved the photodegradation rate. In the case of the aggregated particles with Pt co-catalyst, the photodegradation rate increases (solid square markers; $k = 13.52 \cdot 10^{-3} \text{ min}^{-1}$). Further, the value of k for aggregated particles is more than four times relative to the nanoparticles reference. The combination of the macroporous structure and added Pt in the WO₃-based catalyst resulted in optimum conditions, generating photocatalytic performance with $k = 17.18 \cdot 10^{-3} \text{ min}^{-1}$ (solid triangle markers). This result shows that the k value is more than five

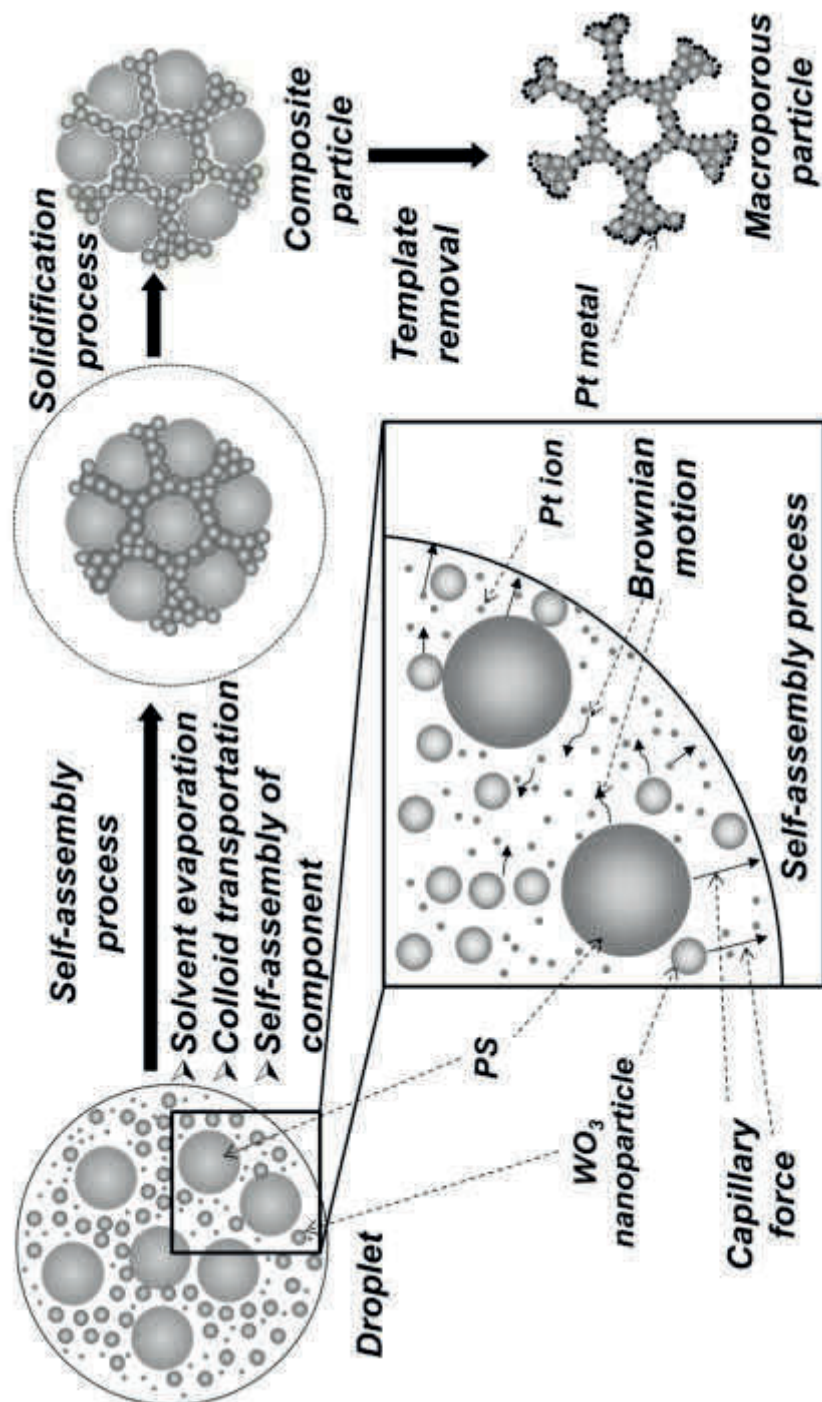


Figure 5.7. Proposed formation mechanism of the spherical macroporous Pt-modified WO_3 particles.

times higher than that of the nanoparticles reference. The k values obtained for the different WO_3 particles are shown in **Table 5.2**.

Figure 9 shows the recyclability of aggregated particles with macroporous and additional Pt as a co-catalyst for photodegradation of RhB. The inset SEM image shows both before and after three times cycling test, essentially maintain the same morphology. Process degradation of RhB was divided into two zones. First, the process was conducted in the dark condition. Second, the process was conducted under the visible light. In general, photocatalytic activity gradually decreased from 80 to 60%. The percentage of degradation RhB in the dark condition decreased from 20 to 6%. However, in the light condition, degradation of RhB was almost stable of around 60%. These prove that the changes of photocatalytic activity could be associated with the attachment of RhB on the particle surface, resulted in the decreases of absorption capability.

5. 3.4 Correlation between particle morphology, added Pt, and photocatalytic activity

Based on the photocatalytic results in **Figure 5.8**, different types of WO_3 catalysts produced different photodegradation behaviors of RhB. Considering that all particles featured the same crystal phase (based on XRD analysis in **Figure 5.5**), the different photocatalytic behaviors were attributed into two factors: the change in particle morphology and the presence of Pt co-catalyst.

Figure 5.10 shows the nitrogen adsorption analysis of the prepared particles. The result showed that the prepared particles based on WO_3 nanoparticles with and without additional PS exhibited a characteristic type-IV isotherm, indicated that the prepared particles contained mesoporous structures, while, dense particles exhibited characteristic type-II isotherm. Total surface area of aggregated particles was of $15\text{m}^2\text{g}^{-1}$, and aggregated particles with macroporous were $54\text{m}^2\text{g}^{-1}$, whereas total surface area of dense particles was of $2\text{m}^2\text{g}^{-1}$. This proves that aggregated particles have better photocatalytic performance than dense particles due to the existence of mesoporous structure which can increase the surface area.

Furthermore, in the present report, a geometrical analysis model was proposed to explain the correlation between particle morphology and surface area (**Figure 5.11**).

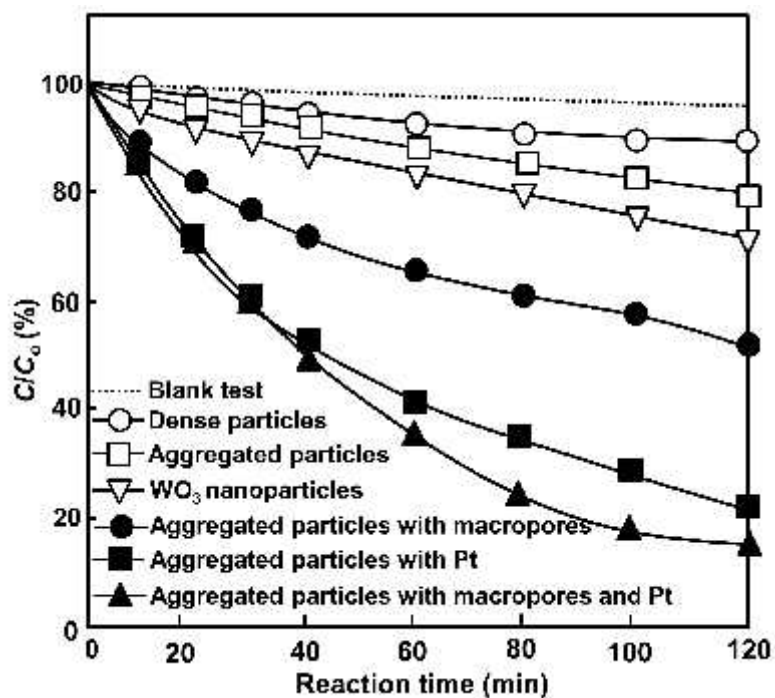


Fig. 5.8. Photodegradation profiles of RhB in the absence of catalyst (dotted line) and the presence of various WO₃-based catalysts.

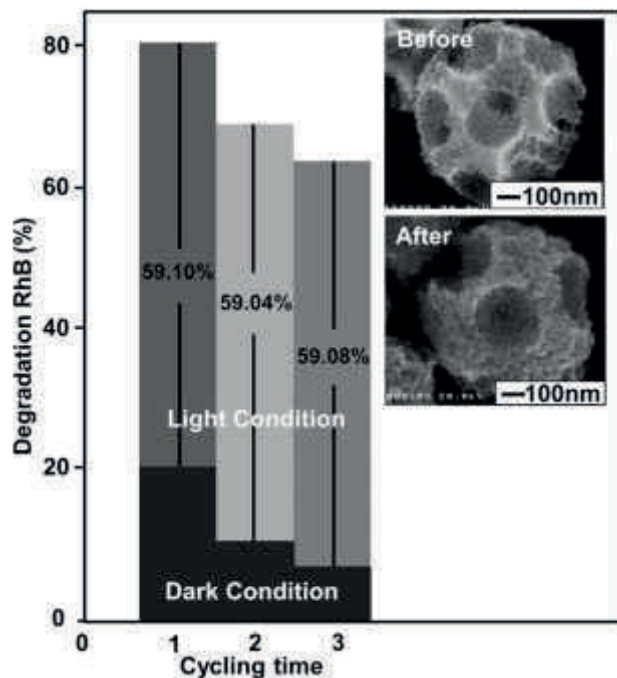


Fig. 5.9. Recyclability performance of aggregated particles with macroporous and Pt addition for photodegradation of RhB.

Table 5.2. Photodecomposition rate constants determined experimentally and surface area ratios calculated using a geometric model.

| Type | WO ₃ source | k (10^{-3} min^{-1}) | k/k_{ATP} | A/A_{ATP} | A/A_{ATP} <i>BET</i> |
|---|------------------------|------------------------------------|-------------|-------------|---------------------------|
| Dense particles | ATP | 0.97 | 1.00 | 1.00 | 1.00 |
| Aggregated particles | nanoparticle | 2.35 | 2.43 | 2.91 | 7.50 |
| Nanoparticle | nanoparticle | 2.98 | 3.08 | - | - |
| Aggregated particles with macropores | nanoparticle | 6.14 | 6.35 | 7.63 | 27 |
| Aggregated particles with Pt | nanoparticle | 13.99 | 13.99 | 2.91* | 7.5* |
| Aggregated particles with macropores and Pt | nanoparticle | 17.18 | 17.79 | 7.63* | 27* |

Note:

k = the photodecomposition rate;

A = the surface area of particles

*Effect of Pt amount is negligible for the calculating of surface area.

In this model, we focused only on the interaction between the water molecules and surface active catalyst. When the catalyst is dense with a smooth surface, interactions between the water molecules and surface active sites are limited (**Figure 5.11a**). Chemical interactions and light penetration occur only on the particle surface, while the catalytic components inside the catalyst remain inactive.

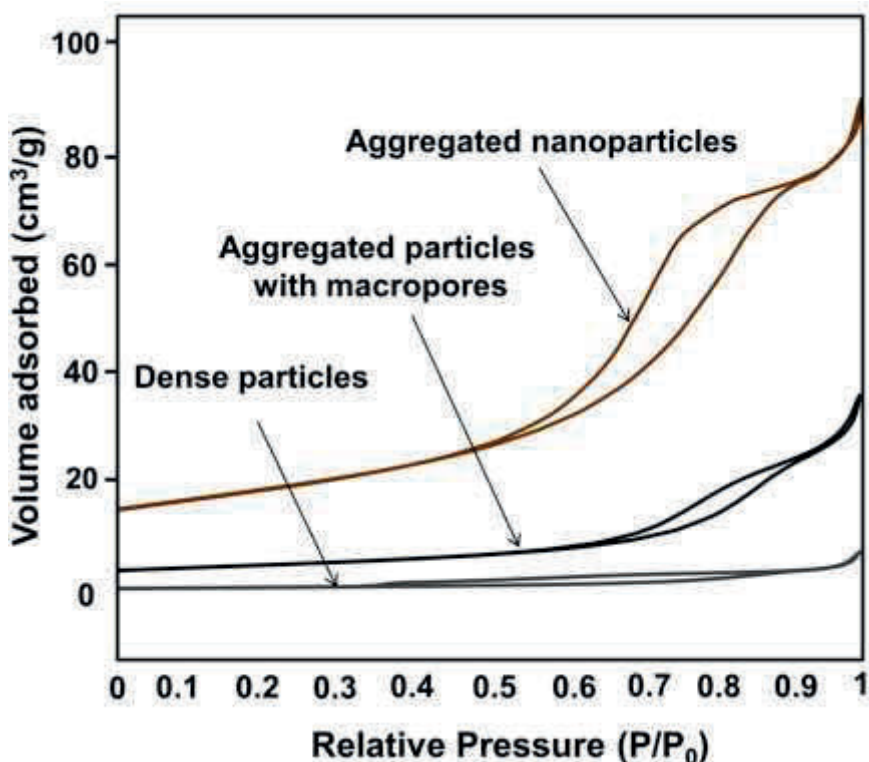


Fig. 5.10. Nitrogen adsorption of the prepared particles.

5.3.4.1 Effect of particle morphology

When the prepared particles are synthesized from WO₃ nanoparticles, the number of surface active sites increases (**Figure 5.11b**). The presence of cavities between aggregated nanoparticles promotes the penetration and diffusion of chemical species into the catalyst. Consequently, photocatalytic activity improves. However, owing to limitation of light penetration into the deepest regions of the catalyst, further catalytic process in the deepest region of catalyst cannot be done well. To improve further photocatalytic activity, additional presence of a macroporous structure in the

catalyst can be used (**Figure 5.11c**). The macropores enable the penetration of both light and chemical species into the deepest region of the catalyst.

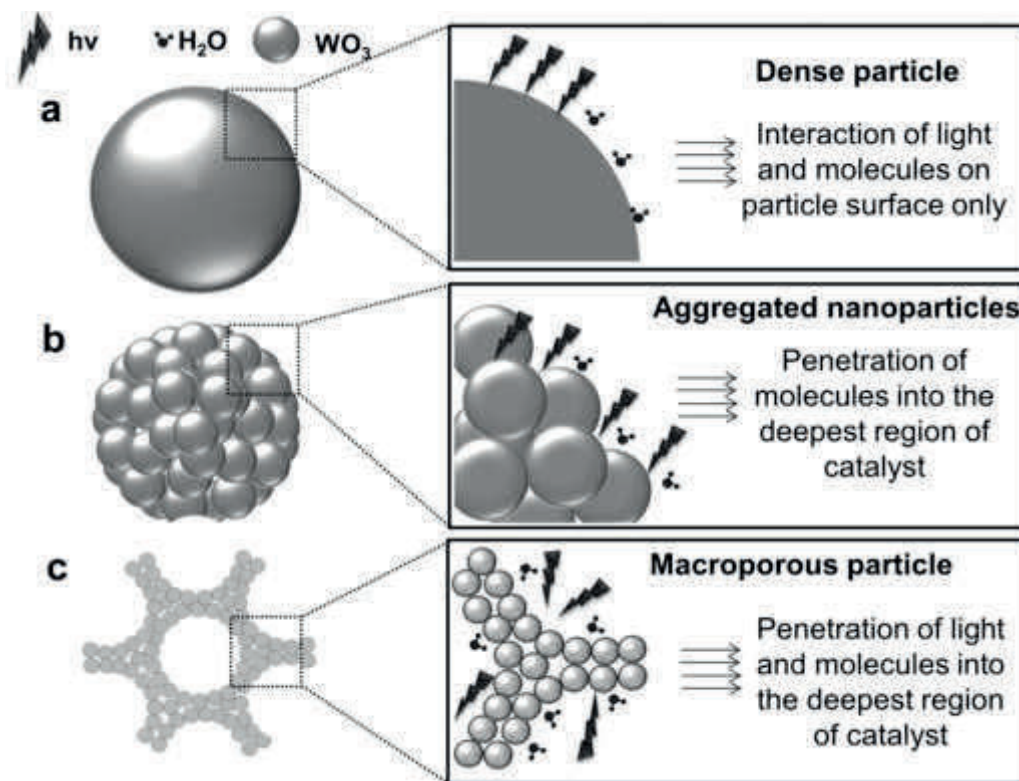
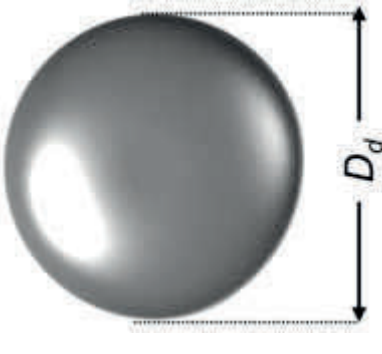
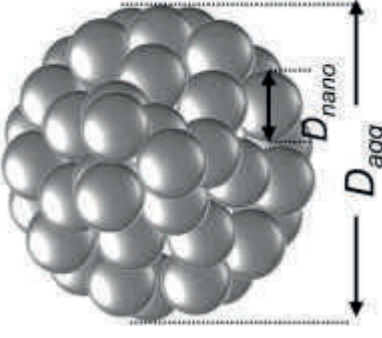
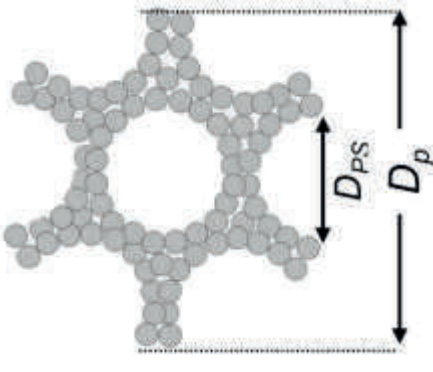


Figure 11. Proposed interaction mechanism between water molecules and surface active sites on WO_3 catalyst with different sizes and structures: (a) dense particles with a smooth surface; (b) aggregated particles (prepared from nanoparticles); and (c) aggregated particles with macropores.

A simple geometrical calculation for predicting the surface area as a function of particle morphology is shown in **Table 5.3**. We used three types of particle models: dense particles with a smooth surface ("dense particles" model), dense particles prepared from nanoparticles ("aggregated particles" model), and macroporous particles ("aggregated particles with macropores" model). The ratio of surface area between BET analysis results and geometrical calculation will be different. To estimate the surface area via a simple geometrical calculation, six assumptions are made: (1) All calculations are based on the same mass of WO_3 used for the photocatalytic process; (2) All particles

Table 5.3. Prediction of surface area based on geometrical model.

| Type | Dense Particles | Aggregated particles | Aggregated particles with macroporous |
|-----------------------------------|---|--|---|
| Model 3D |  |  |  |
| Surface area of a single particle | $A_d = \pi D_d^2$ | $A_{agg} = C_D \pi \frac{f}{D_{agg}} [D_{agg}^3 - (D_{agg} - 2D_{nano})^3]$ | $A'_{pore} = C_D n_{active} \pi D_{nano}^2 + \pi D_p^2 - \frac{n_{PS} \pi}{8} (D_{PS} + 2D_{nano})^2$ |

Note:

A_d = Surface area of a single spherical dense particle;

A_{agg} = Surface area of a single spherical particle prepared from aggregated nanoparticles;

A'_{pore} = Surface area of single porous structured particle

D_{PS} = the mean diameter of PS;

D_{nano} = the mean diameter of WO_3 nanoparticles;

f = the packing fraction;

C_D = the number of WO_3 nanoparticles that are active and interact with molecules and light directly;

n_{prot} = the number of protruded PS forming holes;

n_{active} = the number of active area and interacts with molecules and light

are homogenous in size and shape; (3) During the self-assembly process, all components completely fill the space with maximum arrangement; (4) Photon absorption occurs on the particle surface only (**Figure 5.12**); (5) No sintering phenomenon between the small aggregated nanoparticles exists; (6) For the "aggregated particles with macropores" model, all PS components are completely removed; thus, the generated pores are a replication of the PS components in terms of size and shape. Detailed derivations of the equations used in this model are explained. In this model, several assumptions are made:

- i) All calculations are based on the same mass of WO_3 used for the photocatalytic process
- ii) All particles are homogenous in size and shape; The mean outer diameter of all models are the same, based on particle size measurement by Ferret analysis of SEM images
- iii) During the self-assembly process, all components completely fill the space with maximum arrangement.
- iv) Photon absorption occurs on the particle surface only (see **Figure 5.12**)
- v) No "kissing effect" between the small aggregated nanoparticles exists
- vi) For the "porous" model, all PS components are completely removed; thus, the generated pores are a replication of the PS components in terms of size and shape.

Based on the above assumptions, the calculation of surface area in the catalyst can be described in the following.

5.3.4.1.1. Spherical dense particles

For a single particle with a mean diameter of D_d , the surface area of a single spherical dense particle (A_d) can be calculated using

$$A_d = fD_d^2 \quad (5.1)$$

The D_d is the mean outer diameter of dense particles.

5.3.4.1.2. Spherical particles prepared from aggregated nanoparticles

Surface area of a single aggregated particle

Using assumptions shown in **Figure 5.12b**, the surface area of a single spherical particle prepared from aggregated nanoparticles (A_{agg}) can be predicted by calculating number of nanoparticles arranging on the surface of particle ($n_{nano,surf}$).

$$A_{agg} = C_D n_{nano,surf} f D_{nano}^2 \quad (5.2)$$

where D_{nano} is the outer diameter of WO_3 nanoparticles measured from Ferret analysis of SEM images. C_D is the number of WO_3 nanoparticles that are active and interact with molecules and light directly. In the case of ideal condition, C_D can be approximated as 0.50.

To approximate the number of nanoparticles on the surface ($n_{nano,surf}$), the volume of arrangement nanoparticles on the first layer of the aggregated particle ($V_{nano,surf}$) compared with volume of a single WO_3 nanoparticle (V_{WO_3nano}) must be considered. The value of $V_{nano,surf}$ is

$$V_{nano,surf} = \frac{1}{6} f f \left[D_{agg}^3 - (D_{agg} - 2D_{nano})^3 \right] \quad (5.3)$$

where D_{agg} and f are the mean diameter of the aggregated particles and the packing fraction, respectively. Therefore, the value of n_{nano} is

$$n_{nano,surf} = \frac{V_{nano,surf}}{V_{WO_3nano}} \quad (5.4)$$

After simple conformation, we can get

$$n_{nano,surf} = \frac{f}{D_{nano}^3} \left[D_{agg}^3 - (D_{agg} - 2D_{nano})^3 \right] \quad (5.5)$$

Substituting this equation to equation (2), we can get

$$A_{agg} = C_D f \frac{f}{D_{nano}} \left[D_{agg}^3 - (D_{agg} - 2D_{nano})^3 \right] \quad (5.6)$$

Total surface area of aggregated particles compared with dense particles

To calculate the ratio of surface area between aggregated particles and dense particles (A_{agg} / A_d), the ratio density (ρ) should be added into the equation. Transforming ratio of A_{agg} / A_d , the equation can be written as

$$\frac{A_{agg}}{A_d} = f \left(\frac{D_{agg}^3 - (D_{agg} - 2D_{nano})^3}{D_d^2 \cdot D_{nano}} \right) \quad (5.7)$$

5.3.4.1.3. Porous-structured particles

Assuming that the PS are in a hexagonal packing arrangement and the WO₃ nanoparticles are filling in the space between the PS arrangement, the surface area of a single porous structured particle (A'_{pore}) can be described in the following:

$$A_{pore}^1 = A_{surface} + A_{pore} \quad (5.8)$$

where $A_{surface}$ and A_{pore} are the external surface area and the surface pores inside the particle.

Surface pore of a single porous particle

The surface pore (A_{pore}) is calculated by involving the number of WO₃ nanoparticles (n_{active}) on the holes. The A_{pore} defines

$$A_{pore} = C_D n_{active} f D_{nano}^2 \quad (5.9)$$

where C_D is the number of WO₃ nanoparticles that are active and interact with molecules and light directly. In the case of ideal condition, C_D can be approximated as 0.50. In addition, since the number of n_{active} relates to the mean diameter of PS (D_{PS}) and the mean outer diameter of porous particle (D_P), n_{active} is approximated by

$$n_{active} = \frac{3}{4} n_{PS} \left(\frac{(2D_{nano} + D_{PS})^3 - D_{PS}^3}{D_{nano}^3} \right) f \quad (5.10)$$

where n_{PS} is the number of PS consisted in the final particle. When PS and WO₃ nanoparticles self-assemble in the maximum arrangement, the value of n_{PS} can be estimated by

$$n_{PS} = 0.23 \left(1 + \frac{D_P}{D_{PS} + 2D_{nano}} \right)^{3.58} \quad (5.11)$$

External surface area of a single porous particle

The $A_{surface}$ is approximated by calculating the number of WO_3 on the surface of the particle. However, since there are surface pores formed by the protruded out PS on the particle, the calculation of surface pores must be accounted. Thus, the $A_{surface}$ is

$$A_{surface} = A_P - \frac{n_{prot}f}{4}(D_{PS} + 2D_{nano})^2 \quad (5.12)$$

where A_P is surface area of a single particle ($A_P = fD_P^2$). n_{prot} is the number of protruded PS forming holes. To simplify the calculation of n_{prot} , we assumed that the

$n_{prot} = \frac{1}{2}n_{PS}$. Therefore, $A_{surface}$ is

$$A_{surface} = fD_P^2 - \frac{n_{PS}f}{8}(D_{PS} + 2D_{nano})^2 \quad (5.13)$$

Total surface area of porous particles compared with dense particles

To calculate the ratio of surface area between porous particles ($A_{totpore}$) and dense particles (A_d), the density of porous particle (ρ) should be added. The density is equal to the optimum fraction of WO_3 nanoparticles used in the precursor for preparing porous particles (we used $\rho = 0.75$). The ratio $A_{totpore}/A_d$ is

$$\frac{A_{totpore}}{A_d} = \frac{1}{\rho} \left(\frac{A_{pore}^1}{fD_d^2} \right) \quad (5.14)$$

Taking into account the outer diameter of the WO_3 particles of $0.7 \mu m$ (based on Ferret analysis of SEM images of the prepared particles), the surface area of "aggregated particles" model is about three times as high as that of "dense particles" model. Furthermore, the surface area of the "aggregated particles with macropores" model markedly improved by up to eight times. Based on these results, we can conclude that the change in the morphology directly correlates to the improved photocatalytic performance, in which this was confirmed by the photocatalytic results in **Table 5.2**. Although the trend for the improvement of catalytic activity is proportional to the change of surface area, some errors are found. The experimental results are lower than the calculation of surface area. The dissimilar k value and surface area ratios are because some of catalytic parts do not interact well with both light and chemical species.

5.3.4.2 Effect of added Pt

Based on the surface area model in **Figure 5.11**, the calculated surface areas of particles in the presence and absence of Pt were similar (**Table 5.2**). However, the photocatalytic results in **Figure 5.8** showed that the added Pt effectively improved the photocatalytic performance. The k value of the dense particles containing Pt was more than five times higher than that without Pt. A higher k value was also observed in the case of aggregated particles with macropores; more specifically, the k value of the aggregated particles with macropores and Pt was almost three times as high as that without Pt. These results strongly suggested that loading Pt as a co-catalyst greatly enhanced the photocatalytic performance.

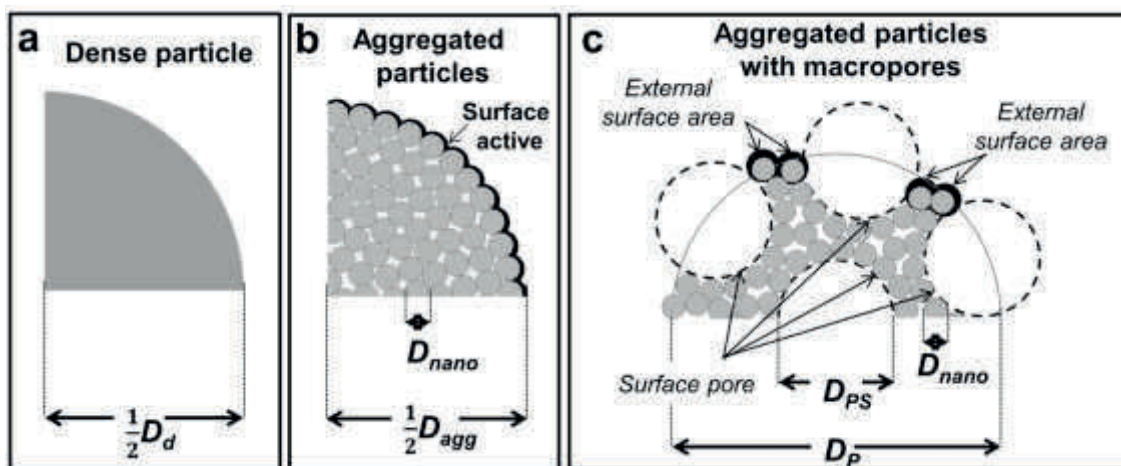


Fig. 5.12. Illustration of the effect particle morphology on the surface area.

To discuss the effect of Pt co-catalyst on the photocatalytic reaction, a mechanism of the photocatalytic process operating in the presence of the Pt-modified WO_3 system is shown in **Figure 5.13**. In this model, catalyst activation is possible only upon light irradiation with an appropriate amount of energy. Considering a WO_3 catalyst system, light irradiation ($h\nu$) on the catalyst results in the production of electrons (e^-) in the conduction band (CB) and holes (h^+) in the valence band (VB). These e^- and h^+ are then used for converting oxygen (O_2) and water molecules (H_2O), respectively. However, because WO_3 has a low CB, electron–hole recombination

processes occur, consequently leading to reduce production of hydroxyl radicals required for degrading the target organic compound [29].

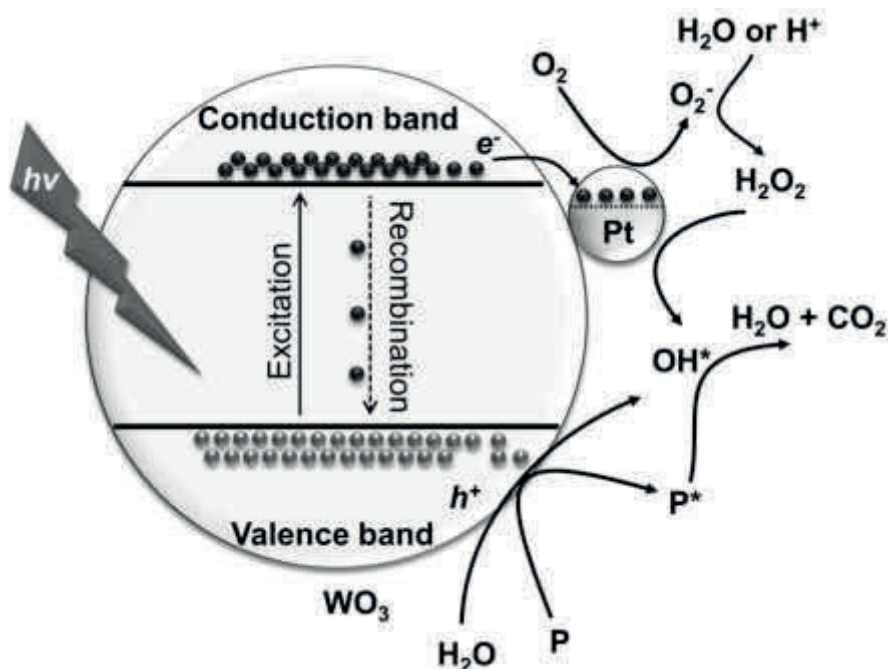


Figure 13. Proposed photocatalysis mechanism operating in the presence of a Pt-modified WO_3 particle system.

In a system containing WO_3 and Pt, an additional reaction mechanism occurs. The work function of WO_3 (5.7 eV) is larger than that of Pt (5.1 eV). When the Pt contacts WO_3 , the e^- will migrate from Pt to CB of WO_3 to achieve Fermi level equilibration. Consequently, Pt exhibits an excess positive charge, while WO_3 accumulates excess e^- . Under visible light illumination, Pt acts as an electron pool for trapping the produced e^- as the effect of deflexed energy band. These trapped to facilitate the multi e^- are then used for further reduction of oxygen molecules which has more positive potential for $2e^-$ and $4e^-$ than the $1e^-$ reduction. This leads to increase generation of H_2O_2 are then for further production hydroxyl radicals (OH^*) [9,16,30], as following Eqs.:





Therefore, the small amount of Pt to modified WO₃ catalysts displayed higher photocatalytic performance than bare WO₃, as confirmed in **Figure 5.8**

5.4 Conclusions

We successfully synthesized spherical macroporous Pt-modified WO₃ particles using a spray-drying method. The particles were prepared from a precursor containing WO₃ nanoparticles, Pt solution, and PS spheres (as a sacrificial colloidal template). The size and shape of the pores were consistent with that of initial PS template, suggesting that the pore size of the final product can be regulated accordingly. The numbers of pores are also controllable by altering the amount of PS added to the precursor. Photocatalytic analysis showed that the changes in particle morphology (from dense with a smooth surface, dense with a rough surface, to porous structure) and presence of Pt as a co-catalyst effectively improved the photocatalytic activity of WO₃. WO₃ particles prepared at a PS/WO₃ mass ratio of 0.32 and Pt co-catalyst achieved the best photocatalytic results, whereby the photocatalytic rate was more than five times higher than that achieved over pure WO₃ nanoparticles. The relationships between the change in particle morphology, added Pt as co-catalyst, and photocatalytic performance were investigated in detail and corresponding photocatalytic reaction mechanisms were proposed. The current strategy is a gateway towards designing materials with excellent performance but using relatively low amounts of raw materials.

Nomenclature

| | | |
|---------------|---|--|
| A_d | = | Surface area of a single spherical dense particle , μm^2 |
| A_{agg} | = | Surface area of a single spherical particle prepared from aggregated nanoparticles, μm^2 |
| A_P | = | Surface particle, μm^2 |
| A_{pore}^I | = | Surface area of single porous structured particle, μm^2 |
| $A_{surface}$ | = | External surface area, μm^2 |
| A_{pore} | = | Surface pores inside the particle, μm^2 |
| $A_{totpore}$ | = | Surface porous particle, μm^2 |
| C_D | = | Number of WO_3 nanoparticles that are active and interact with molecules and light directly, 0.50 |
| D_d | = | Mean outer diameter of dense particle, μm^2 |
| D_{nano} | = | Mean outer diameter of WO_3 nanoparticles, μm^2 |
| D_{PS} | = | Mean diameter of PS, μm |
| D_{agg} | = | Mean diameter of the aggregated particles, μm |
| D_P | = | Mean outer diameter of porous particle, μm |
| f | = | Packing factor, 0.74 |
| n_{nano} | = | Number of nanoparticles arranging on the surface of particle |
| n_{PS} | = | Number of PS consisted in the final particle |
| n_{prot} | = | Number of protruded PS forming holes |
| n_{active} | = | Number of WO_3 nanoparticle on the holes |
| $\{$ | = | Density of aggregated particles, 0.74 |
| $'$ | = | Density of porous particle, 0.75 |

5.5 References

- [1] De Respinis, M.; De Temmerman, G.; Tanyeli, I.; van de Sanden, M. C.; Doerner, R. P.; Baldwin, M. J.; van de Krol, R., Efficient plasma route to nanostructure materials: case study on the use of m- WO_3 for solar water splitting, ACS Applied Materials and Interfaces, 5 (2013) 7621-7625.

- [2] Deepa, M.; Srivastava, A.; Agnihotry, S., Influence of Annealing on Electrochromic performance of template assisted, electrochemically grown, nanostructured assembly of tungsten oxide, *Acta Materialia*, 54 (2006) 4583-4595.
- [3] Deepa, M.; Srivastava, A.; Lauterbach, S.; Shivaprasad, S.; Sood, K., electro-optical response of tungsten oxide thin film nanostructures processed by a template-assisted electrodeposition route, *Acta materialia*, 55 (2007) 6095-6107.
- [4] Guo, Y.; Quan, X.; Lu, N.; Zhao, H.; Chen, S., High photocatalytic capability of self-assembled nanoporous WO₃ with preferential orientation of (002) planes, *Environmental Science Technology*, 41 (2007) 4422-4427.
- [5] Morales, W.; Cason, M.; Aina, O.; de Tacconi, N. R.; Rajeshwar, K., Combustion synthesis and characterization of nanocrystalline WO₃, *Journal of American Chemical Society*, 130 (2008) 6318-6319.
- [6] Jiao, Z.; Wang, J.; Ke, L.; Sun, X. W.; Demir, H. V., Morphology-tailored synthesis of tungsten trioxide (hydrate) thin films and their photocatalytic properties, *ACS Applied Materials and interfaces Interfaces*, 3 (2011) 229-236.
- [7] Zoontjes, M. G.; Huijben, M.; Baltrusaitis, J.; van der Wiel, W. G.; Mul, G., Selective hydrothermal method to create patterned and photoelectrochemically effective Pt/WO₃ interfaces, *ACS Appl. Mater. Interfaces* 5 (2013) 13050-13054.
- [8] Ng, C.; Ng, Y. H.; Iwase, A.; Amal, R., Influence of annealing temperature of wo₃ in photoelectrochemical conversion and energy storage for water splitting, *ACS Applied Materials and Interfaces*, 5 (2013) 5269-5275.
- [9] Kim, J.; Lee, C. W.; Choi, W., Platinized WO₃ as an environmental photocatalyst that generates OH radicals under visible light, *Environmental Science and Technology*, 44 (2010) 6849-6854.
- [10] Huang, H.; Yue, Z.; Song, Y.; Du, Y.; Yang, P., Mesoporous tungsten oxides as photocatalysts for O₂ evolution under irradiation of visible light. *Materials Letter* , 88 (2012) 57-60.
- [11] Ashkarran, A.; Ahadian, M.; Ardakani, S. M., Synthesis and photocatalytic activity of wo₃ nanoparticles prepared by the arc discharge method in deionized water, *Nanotechnology*, 19 (2008) 195709.

- [12] Martínez-de la Cruz, A.; Martínez, D. S.; Cuéllar, E. L., Synthesis and characterization of WO₃ nanoparticles prepared by the precipitation method: evaluation of photocatalytic activity under vis-irradiation, *Solid State Science*, 12 (2010) 88-94.
- [13] Xu, Z.; Tabata, I.; Hirogaki, K.; Hisada, K.; Wang, T.; Wang, S.; Hori, T., Preparation of platinum-loaded cubic tungsten oxide: a highly efficient visible light-driven photocatalyst, *Materials Letter*, 65 (2011) 1252-1256.
- [14] Elezovic, N.; Babic, B.; Ercius, P.; Radmilovic, V.; Vracar, L. M.; Krstajic, N., Synthesis and characterization pt nanocatalysts on tungsten based supports for oxygen reduction reaction, *Applied Catalysis B*, 125 (2012) 390-397.
- [15] Luo, J. Y.; Gong, L.; Tan, H. D.; Deng, S. Z.; Xu, N. S.; Zeng, Q. G.; Wang, Y., Study of the catalyst poisoning and reactivation of pt nanoparticles on the surface of WO₃ nanowire in gasochromic coloration, *Sensors and Actuator B*, 171 (2012) 1117-1124.
- [16] Miyauchi, M., Photocatalysis and photoinduced hydrophilicity of WO₃ thin films with underlying Pt nanoparticles, *Physical Chemistry Chemical Physics*, 10 (2008) 6258-6265.
- [17] Shiraishi, Y.; Sugano, Y.; Ichikawa, S.; Hirai, T., Visible light-induced partial oxidation of cyclohexane on WO₃ loaded with Pt nanoparticles, *Catalyst Science and Technology*, 2 (2012) 400-405.
- [18] Cui, X.; Shi, J.; Chen, H.; Zhang, L.; Guo, L.; Gao, J.; Li, J., Platinum/mesoporous WO₃ as a carbon-free electrocatalyst with enhanced electrochemical activity for methanol oxidation, *Journal of Physical Chemistry B*, 112 (2008) 12024-12031.
- [19] Yan, Z.; Wei, W.; Xie, J.; Meng, S.; Lü, X.; Zhu, J., An ion exchange route to produce WO₃ nanobars as Pt electrocatalyst promoter for oxygen reduction reaction, *Journal of Power Sources*, 222 (2012) 218-224.
- [20] Nandiyanto, A. B. D.; Arutanti, O.; Ogi, T.; Iskandar, F.; Kim, T. O.; Okuyama, K., Synthesis of spherical macroporous WO₃ particles and their high photocatalytic performance. *Chemical Engineering Science*, 101 (2013) 523-532.

- [21] Arutanti, O.; Ogi, T.; Nandiyanto, A. B. D.; Iskandar, F.; Okuyama, K., Controllable crystallite and particle sizes of WO₃ particles prepared by a spray-pyrolysis method and their photocatalytic activity, *AIChE Journal*, 60 (2014) 41-49.
- [22] Arutanti, O.; Nandiyanto, A. B. D.; Ogi, T.; Iskandar, F.; Kim, T. O.; Okuyama, K., Synthesis of composite WO₃/TiO₂ nanoparticles by flame-assisted spray pyrolysis and their photocatalytic activity, *Journal of Alloys Compounds*, 591 (2014) 121-126.
- [23] Purwanto, A.; Widiyandari, H.; Ogi, T.; Okuyama, K., Role of particle size for platinum-loaded tungsten oxide nanoparticles during dye photodegradation under solar-simulated irradiation, *Catalysis Communications*, 12 (2011) 525-529.
- [24] Ogi, T.; Nandiyanto, A. B. D.; Okuyama, K., Nanostructuring strategies in functional fine-particle synthesis towards resource and energy saving applications, *Advanced Powder Technology*, 25 (2014) 3-17.
- [25] Nandiyanto, A. B. D.; Suhendi, A.; Ogi, T.; Iwaki, T.; Okuyama, K., Synthesis of additive-free cationic polystyrene particles with controllable size for hollow template applications, *Colloids Surfaces A*, 396 (2012) 96-105.
- [26] Nandiyanto, A. B. D.; Okuyama, K., Progress in developing spray-drying methods for the production of controlled morphology particles: from the nanometer to submicrometer size ranges, *Advanced Powder Technology*, 22 (2011) 1-19.
- [27] Li, N.; Hu, Z.; Zheng, M.; Lu, H.; Zhao, B.; Zhang, S.; Zheng, J.; Ji, G.; Cao, J., Formation of Pt nanoparticles in mesoporous silica channels via direct low-temperature decomposition of H₂PtCl₆·6H₂O, *Materials Letter*, 106 (2013) 193-196.
- [28] Hernandez, J. O.; Choren, E. A., Thermal stability of some platinum complexes, *Thermochimica Acta*, 71 (1983), 265-272.
- [29] Wen, Z.; Wu, W.; Liu, Z.; Zhang, H.; Li, J.; Chen, J., Ultrahigh-efficiency photocatalysts based on mesoporous Pt–WO₃ nanohybrids, *Physical Chemistry Chemical Physics*, 15 (2013) 6773-6778.
- [30] Yang, F.; Takahashi, Y.; Sakai, N.; Tatsuma, T., Photocatalytic remote oxidation induced by visible light, *Journal of Physical Chemistry C*, 115 (2011) 18270-18274.

Chapter 6

Summary

6.1 Conclusions

The synthesis of nanostructured WO_3 particles using aerosol method (i.e. spray-pyrolysis and flame-assisted spray-pyrolysis) for photocatalytic application was systematically described in this dissertation. For the conclusions of the dissertation, the major results are summaries as follows:

1. The synthesis of WO_3 particles with controllable crystallite and particle sizes using a spray-pyrolysis method, and their photocatalytic performance was systematically investigated. The particle morphology and crystallite size were controlled by changing precursor concentration and synthesis temperature. The as-prepared particles had a mean diameter from 58 to 677 nm depends on the synthesis temperature. From XRD pattern obtained, it was found that crystallite size increased by changing synthesis temperature from 120 to 1000°C, and decreased when the synthesis temperature of above 1000°C. The result showed that photocatalytic performance can be optimized by changing both crystallite and particle size. WO_3 particles with a mean diameter of 105 nm and crystallite size of 25 nm had the highest photocatalytic performance.
2. Composite WO_3/TiO_2 nanoparticles were successfully prepared by a flame-assisted spray-pyrolysis method. The as-prepared particles had different characteristics (i.e. morphology, crystallinity, light absorbance, and photocatalytic activity) by various amounts of WO_3 and TiO_2 . When the AMT amount was less than 25 wt%, photocatalytic performance drastically increased. The result showed that the increases in photocatalytic performance were significantly influenced by the change of band gap energy, while the surface area slightly increased. It can be concluded that beside the presence of band gap, the surface area also plays an important role.
3. The present study demonstrated an effective method to synthesis nanostructured macroporous WO_3 using spray-drying method. Ammonium tungstate pentahydrate (ATP) and Polystyrene (PS) with a size of 230 nm was used as a WO_3 source and

polymer template, respectively. Porous structure and particle morphology were controlled by changing PS/ATP mass ratio and precursor concentration, respectively. WO_3 particles with macroporous structure have a higher photocatalytic performance than that of WO_3 non-porous particles, confirming the effectiveness of porous structure on the enhancement of photocatalytic performance. It was found that the as-prepared particles with a PS/ATP mass ratio of 0.60 showed the highest photocatalytic performance 2.5 times than that of dense particles.

4. Macroporous WO_3 particles with Pt nanoparticles (NPs) deposition have been successfully prepared by spray-drying method. Mass ratio of PS/ WO_3 NPs was varied from 0.00 to 0.40 to produce particles with highly ordered-porous structure. Morphology analysis results showed that Pt NPs with a mean diameter around 2 nm were distributed on the particle surface. The changes in particle morphology and the presence of Pt NPs as co-catalyst effectively improved photocatalytic performance of WO_3 . Compare with WO_3 dense particles from ATP, aggregated WO_3 particles have a higher photocatalytic performance. It was found that the presence of Pt NPs was significantly enhanced the photocatalytic performance of WO_3 . The highest photocatalytic performance of WO_3 was prepared from the precursor with a PS/ WO_3 mass ratio of 0.32 and Pt concentration of 0.23 wt%.

From the conclusions stated above, it is can be highlight that morphology, crystallinity, band gap energy, and the presence of co-catalyst material are the main factors to improve photocatalytic performance of WO_3 semiconductor. Where, the intrinsic properties of material are important to control electron-hole recombination during photocatalytic process.

Acknowledgment

I would like to thank ALLAH S.W.T MIGHTY because without Allah`s will this dissertation would not have been possible at all.

First of all, I would like to express my deepest gratitude to my supervisor, Professor Kikuo Okuyama for providing very helpful advice, guidance, continuing encouragement not only research but also daily life.

I also would like to thank Professor Tsuneji Sano, Professor Kunihiro Fukui, and Professor Akihiro Yabuki for their patience, wisdom and support as referee members. And special thanks to Associate professor Dr. Takashi Ogi and Assistant Professor Dr. Ratna Balgis for their great advices and supports during my research.

I am grateful to Dr. Asep Bayu Dani Nandiyanto, Mr. Shinpei Kaneda, and Dr, Asep Suhendi for willingness supports my research during their stay in Hiroshima University. I also want to thank for the past and present friends in Okuyama laboratory for their kind helps and assistances during my research.

I thank funding from Kumahira, Momiji bank, and Ministry of Education, Culture, Sports, Science and Technology for providing scholarship of my PhD course and Hosokawa Micron Powder Foundation for financial support of my research.

Last but not least, I would like to thank my parents Dr. Wowo S. Kuswana and Mrs. Hasnah, my sister Henny Septiani, and my brother Ojan Prabowo for their prayers, support, and motivation. It is beyond words. Without these, I might not be able to achieve anything.

OSIARUTANTI

Higashi Hiroshima, September 2015